THE EFFECT OF AVERAGE GRAIN SIZE ON THE WORK FUNCTION OF POLYCRYSTALLINE DIAMOND FILMS

Patrick Roland Abbott, B.S., M.S.

Dissertation Prepared for the Degree of

DOCTOR OF PHILOSOPHY

UNIVERSITY OF NORTH TEXAS

May 2002

APPROVED:

David E. Golden, Major Professor
Bruce Gnade, Committee Member
Jeffry Kelber, Committee Member
Zhibing Hu, Committee Member
Samuel E. Matteson, Chair of the Department of Physics
C. Neal Tate, Dean of the Robert B. Toulouse School of Graduate Studies

Abbott, Patrick Roland, The Effect of Average Grain Size on Polycrystalline Diamond Films. Doctor of Philosophy (Physics), May 2002, 123 pp., 5 tables, 90 illustrations, references, 84 titles.

The work function of hydrogen-terminated, polycrystalline diamond was studied using ultraviolet photoelectron spectroscopy. Polycrystalline diamond films were deposited onto molybdenum substrates by electrophoresis for grain sizes ranging from 0.3 to 108 microns. The work function and electron affinity were measured using 21.2 eV photons from a helium plasma source. The films were characterized by x-ray photoelectron spectroscopy to determine elemental composition and the sp^2/sp^3 carbon fraction. The percentage of (111) diamond was determined by x-ray diffraction, and scanning electron microscopy was performed to determine average grain size.

The measured work function has a maximum of 5.1 eV at 0.3 microns, and decreases to 3.2 eV at approximately 4 microns. Then the work function increases with increasing grain size to 4.0 eV at 15 microns and then asymptotically approaches the 4.8 eV work function of single crystal diamond at 108 microns. These results are consistent with a 3-component model in which the work function is controlled by single-crystal (111) diamond at larger grain sizes, graphitic carbon at smaller grain sizes, and by the electron affinity for the intervening grain sizes.

ACKNOWLEDGEMENTS

I would like to thank Dr. David Golden for his direction and encouragement, Edward Sosa for the many informative discussions, and especially my family for their patience and support throughout the years.

TABLE OF CONTENTS

Page

LIST OF TABLES

LIST OF ILLUSTRATIONS

CHAPTER 1 – INTRODUCTION

1.1 PROPERTIES OF DIAMOND

Diamond is formed when carbon atoms are arranged in the hybridized sp^3 tetrahedral structure under high temperature and pressure conditions either naturally or synthetically via chemical vapor deposition (CVD) and other processes. The lattice structure of diamond is a face-centered cubic (fcc) structure with two atoms per unit cell [1]. Figure 1.1 shows the crystal structure with its tetrahedral bond arrangement.

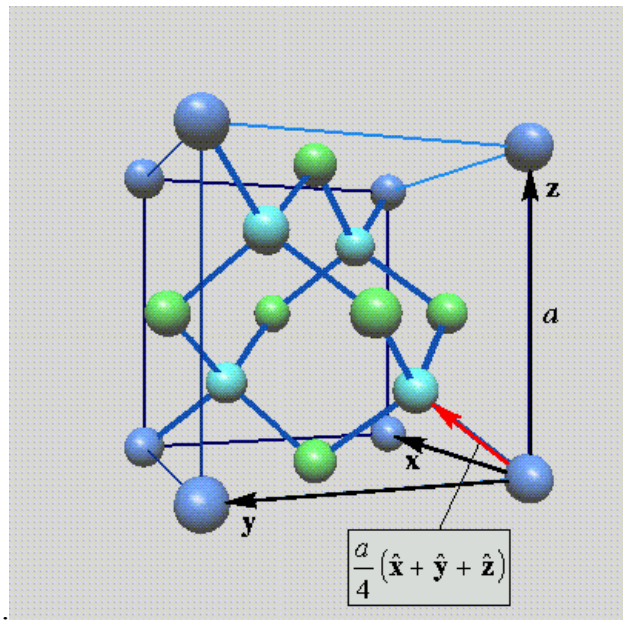

Figure 1.1 Diamond Lattice Structure

The fact that diamond is composed of these interlocking tetrahedral bonds gives its very high bonding strength. The other Group IV elements (silicon, germanium, and tin) also

form this directional covalent bonding. Diamond is similar to other Group IV elements in that they have the electronic configuration ns^2p^2 (where n ranges from 2 to 5).

Diamond has many extreme properties. It is the hardest known material, it is the best thermal conductor, and has a very low thermal expansion coefficient. Shown in Table 1.1 is a list of electrical, optical and structural properties [2].

Property	Value
Band Gap	5.47 eV
Resistivity	$10^{13} – 10^{16}$ Ω·cm
Electron Mobility	2,200 $cm^2/V·s$
Hole Mobility	1,600 $cm^2/V·s$
Dielectric Constant	5.7
Dielectric Strength	10^6 V/cm
Optical Index of Refraction	2.41
Optical Transmissivity	225
Thermal Expansion Coefficient	1.1×10^{-6} K^{-1}
Thermal Conductivity	20.0 W/cm·K
Mass Density	3.516 g/cm3
Atomic Density	17.6×10^{22} cm^{-3}
Nearest Neighbor Distance	1.54 Å

Table 1.1 Diamond Properties

1.2 DIAMOND AS A FIELD EMITTER

The advent of the field emission display (FED) has introduced a need for a chemically inert, low-work function material for use as a field emitter. Diamond films may provide an attractive choice for such a material because of their negative electron affinity (NEA) that may result in a lower work function lower than materials currently being used. In addition, diamond is known to be unreactive with oxygen below 1000°C [3]. Displays currently used suffer rapid degradation because a sufficiently low vacuum environment can not be maintained. The material of choice for field emission displays is molybdenum. However molybdenum is susceptible to oxidation and out-gassing from various internal components compromising their emission properties by forming insulating oxides. In an oxidizing environment, diamond emitters have been shown operate well when conventional emitters fail [4, 5]. It has been shown [6, 7] that Mo tips may be coated with a diamond film that significantly enhances the emission properties. Studies on diamond-coated silicon emitters [8, 9] also have shown improved emission by a factor of two over uncoated emitters. The NEA property lowers the field emission threshold, which translates into a lower turn on voltage for the device.

Diamond films used in previous studies all contained a large mixture of grain sizes. Some authors have suggested the work function of diamond exhibits a dependence on the grain size [10-12], however to date no quantitative studies have been performed. In the present study, the work function and electron affinity of diamond films were measured as a function of grain size. By using commercially prepared micronized diamond powders, it

was possible to study a range of grain sizes from 0.3-108 microns within a few percent of accuracy.

A relationship between crystallite size and work function could have applications in field emission, but also in heterojunctions conductors in microelectronic gate structures. It is believed that what we learn from diamond's properties will be applicable to other wide band gap semiconductors [13].

1.3 NEGATIVE ELECTRON AFFINITY

Figure 1.2 shows the energy band diagram of a typical semiconductor. The work function Φ is defined as the difference in potential energy between the vacuum level E_{vac} and the Fermi level E_f [14].

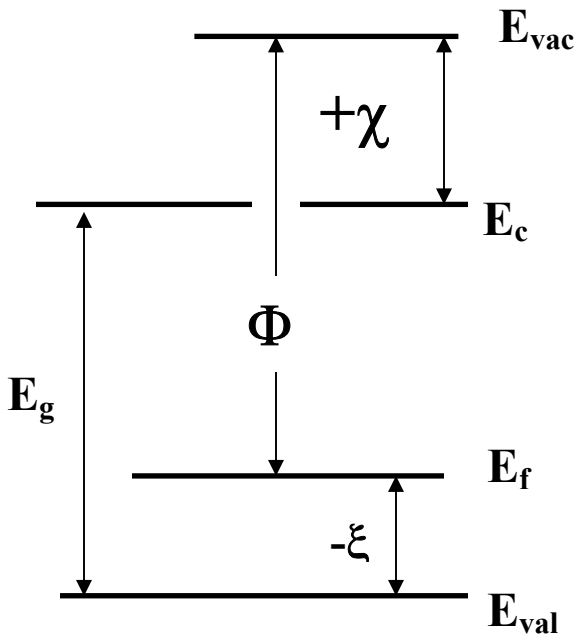

Figure 1.2 Semiconductor Band Diagram

The Fermi level offset ξ is the difference between the VBM and the Fermi level, where natural diamond's Fermi level has been measured as 0.2-0.4 eV below the VBM [15]. The band gap E_g is the energy difference between the valence band maximum and the conduction band minimum.

$$E_G = E_C - E_{val} \tag{1.2}$$

The electron affinity of a semiconductor is defined as the difference between the vacuum level and the conduction band minimum (CBM) given by

$$\chi = E_{vac} - E_C \tag{1.1}$$

Figure 1.2 shows a p-type semiconductor where the Fermi level is closer to the valence band maximum (VBM) than the conduction band minimum (CBM). Diamond is an indirect band gap material and E_g has a temperature dependence [16] of

$$E_G = 5.4925 + \frac{1.979 \times 10^{-4} T^2}{T - 1437} eV \tag{1.3}$$

In this work only room temperature diamond with $E_g = 5.47 \pm 0.005$ eV was studied.

Although conventional semiconductors have a positive electron affinity (PEA), through heavy p-type doping and cesium coating [17], a NEA can be produced. This is achieved by band bending at the surface. In particular, the hydrogen-terminated (111) surface of diamond has NEA [18], and the hydrogen-terminated (100) surface has NEA [19]. In the case of diamond, the vacuum level of the surface lies below the CBM with no special preparation other than naturally occurring hydrogen attachment at defects and grain boundaries.

The band diagram of diamond is shown in Figure 1.3 with NEA.

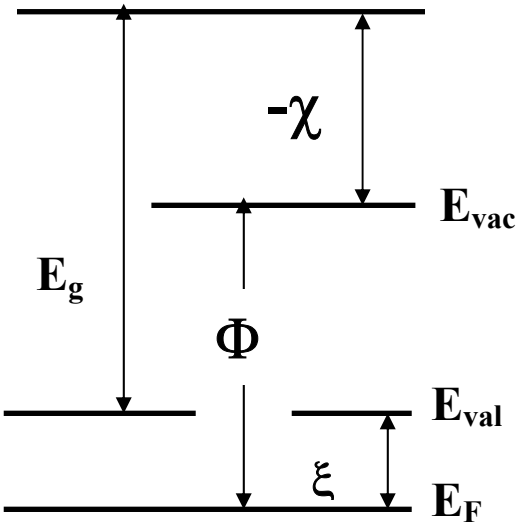

Fig. 1.3 Band Diagram of Diamond

The measurement of a NEA is possible by exciting valence band electrons to the conduction band by UPS. If photoemission occurs with sufficient energy to traverse the band gap, the electron affinity is said to be negative. The electron affinity (when positive) acts as an energy barrier to reach the vacuum level after exciting electrons to the conduction band. The *electron affinity* is defined as the width of the conduction band [20], or the energy to remove an electron from the CBM to the vacuum. It can be interpreted as an atom or molecule's inability to bind an additional electron therefore it is not stable as a negative ion. For example, the rare gases are known to have NEA. For the case of rare gases, the large binding energy splitting between shells pushes the lowest lying empty levels above the vacuum level.

Diamond has the highest thermal conductivity of any solid at room temperature. When considering device applications, this would be useful in high-frequency, high-power devices. Diamond's high breakdown voltage results in a high cutoff frequency and

much higher operational voltage than GaAs or Si [21], and in the case of thin films can act as a direct band gap material [22].

1.4 PREVIOUS STUDIES ON DIAMOND

The first measurement of diamond's NEA was by Himpsel et al. [18], who observed the UPS spectra of the (111) surface. By using photon energies $13 \leq h\nu \leq 35$ eV from synchrotron radiation, the vacuum level was found to lie in the fundamental optical gap below the CBM. This surface was shown by LEED measurements to be the unreconstructed 1×1 surface. This unreconstructed surface was later shown to be hydrogen terminated using photon stimulated ion desorption (PSID) [23]. The LEED pattern was observed for the 1×1 as-polished unreconstructed surface. After annealing at 950 °C for several minutes to desorb the hydrogen, the surface exhibited a 2×2/2×1 reconstruction. Furthermore, exposure to atomic hydrogen replenished the hydrogen on the surface returning the surface to a 1×1 construction.

Subsequent studies also showed that the C(111) surface was hydrogen terminated in a mono-hydride and tri-hydride form. High resolution electron energy loss spectroscopy (HREELS) [24, 25] has shown hydrocarbon species on the surface. This may imply that a tri-hydride (CH_3) is also present in addition to its mono-hydride. However, studies using electron stimulated desorption ion angular distributions (ESDIAD) [26], and He scattering [27] have shown the C(111) 1×1 surface to be predominantly monohydride.

There is a surface reconstruction upon removal of the chemisorbed hydrogen [24]. A 1×1 H-terminated surface reconstructs to a 2×2/2×1 construction after annealing in UHV.

Temperature programmed desorption (TPD) studies have reported hydrogen desorption for temperatures of 825°C [28], 900°C [29], 1000°C [30], and 1300°C [31]. Another study observed a change in the Auger (AES) spectra after an annealing at 950°C [32].

Although a NEA is a measurable quantity, the processes that give rise to this phenomenon are still in question. One model for our NEA surface is that electrons thermalize to the CBM and are able to photo-emit because they interact with holes to form surface dipoles (Mott-Wannier excitons) [33]. These electron-hole pairs originate in the bulk of the crystal and transport to the surface during photo-excitation. Another model attributes the NEA to a surface dipole layer produced by a charge transfer between the H ad-atoms and the topmost carbon atoms [34]. This would explain the absence of the NEA upon removal of the hydrogen. Natural diamond [35] and CVD diamond [26] have both been shown to go from a NEA H-terminated surface to a PEA for the clean (111) surface. As we shall see, there was no occurrence of (100) in this study. All of the films studied contained predominantly (111) diamond.

Most of the studies have been on natural single crystal diamond rather than a diamond film, and there has been little work measuring the work function of diamond. While the work function of graphite is reported to be 5.0 eV [36], the work function of CVD diamond has been shown as low as 3.4 eV [8]. Another study [37] measured the (111) H-terminated surface, and the work function increased with annealing temperature from 3.4 eV to 4.8 eV as the hydrogen was desorbed. Prior to annealing, the field emission characteristics were studied using Fowler-Nordheim distributions. In order to achieve a current density of 1 mA/cm^2, a field of only

E = 2-5 V/μm was necessary. (This compared to 2000 V/μm for a metal with a work function of about 4 eV). It was stated that graphitic carbon between the diamond crystallites (which is highly conductive) assists in supplying electrons for emission. In addition, it was noted in this study that hydrogenation only occurs in the diamond and not the graphite.

In light of these results, the focus of this study was to observe the dependence of the work function of diamond films on grain size.

REFERENCES

[1] I. Watanabe, T. Yamashita, and M. Sugimoto, Jpn. J. Appl. Phys. **31**, 1187 (1992)
[2] W.B. Choi, R. Schlesser, *et.al*., J. Vac. Sci. Technol. B **16**, 716 (1998)
[3] M.T. McClure, R. Schlesser, B.L. McCarson, and Z. Sitar, J. Vac. Sci. Technol. B **15**, 2067 (1997)
[4] W.B. Choi, *et. al.*, Appl. Phys. Lett. **68**, 720 (1996)
[5] S. Albin, W. Fu, A. Varghese, and A.C. Lavarias, J. Vac. Sci. Technol. A, 17, 2104 (1999)
[6] W. Zhu, G.P. Kochanski, S Jin, and L. Seibles, J. Appl. Phys. **78**, 2707 (1995)
[7] J.B. Cui, J. Ristein, and L. Ley, Phys. Rev. B, **60**, 16 135 (1999)
[8] A.A. Rouse, J.B. Bernhard, E.D. Sosa, and D.E. Golden, Appl. Phys. Lett. **75**, 3417 (1999)
[9] M. C. Benjamin, C. Wang, R. F. Davis, and R. J. Nemanich, Appl. Phys. Lett. **64**, 3288 (1994)
[10] Ralph W. G. Wyckoff, *Crystal Structures*, 2nd ed., Interscience Publisher, New York, 26 (1963)
[11] Spear and Dismukes, *Synthetic Diamond - Emerging CVD Science and Technology,* Wiley, NY, 1994
[12] M.W. Geis and M.A. Tamer, *Encyclopedia of Applied Physics*, VCH, Weinheim, 1993, Vol. 5, P. 2.
[13] W. L. Hsu, et al., Appl. Phys. Lett. **55**, 2739 (1989)
[14] C. Kittel, *Introduction to Solid State Physics*, Wiley & Sons Inc., Brisbane, 1996
[15] J.B. Cui, J. Ristein, and L.Ley, Phys. Rev. B **59**, 5847 (1999)
[16] V.G. Varshini, Physica **34**, 149 (1967)
[17] R.L. Bell, *Negative Electron Affinity Devices*, Clarendon, Oxford, 1973
[18] F.J. Himpsel, et al., Phys. Rev. B **20**, 624 (1979)
[19] J. Van der Weide and R.J. Nemanich, Phys. Rev. B **49**, 13629 (1994)
[20] S.O. Kasap, *Principles of Electrical Engineering Materials and Devices*, McGraw-Hill, 1996
[21] M.W. Geis, *et. al*., J.Vac. Sci. Technol. A **6**, 1953 (1988)
[22] A.J. Read, *et al*., Phys. Rev. Lett. **69**, 1232 (1992)
[23] B.B. Pate, et. al., J. Vac. Sci. Technol. **21**, 364 (1982)
[24] B.J. Waclawski, *et. al*., J. Vac. Sci. Technol. **21**, 368 (1982)
[25] S.T. Lee and G. Apai, Phys. Rev. B **48**, 2684 (1993-II)
[26] A.V. Hamza, G.D. Kubiak, and R.H. Stulen, Surface Sci. Lett. **206**, L833 (1988)
[27] G. Vidali *et. al.,* Phys. Rev. Lett. **51**, 118 (1983)
[28] D.D. Koleske *et. al*., J. Chem. Phys. **102** (2), 992 (1995)
[29] R.E. Thomas, R.A. Rudder, and R.J. Markunas, J. Vac. Technol. A, **10**, 2451 (1992)
[30] B.B. Pate *et. al*., J. Vac. Technol., **19** (3), 349 (1981)
[31] M.T. Schulberg, *et. al*., J. Appl. Phys., **77**, 3484 (1995)
[32] I.L. Krainsky and V.M. Asnin, Phys. Rev. B **56**, 13529 (1997)
[33] C. Bandis and B.B. Pate, Phys. Rev. B **52**, 12056 (1995)
[34] J.B. Cui, J. Ristein, and L. Ley, Phys. Rev. Lett. **81**, 429 (1998)

[35] B.B. Pate, et. al., J. Vac. Sci. Technol. A **2**, 957 (1984)
[36] David R. Lide ed., *CRC Handbook of Chemistry and Physics, 73rd ed*., CRC Press Inc., Boca Raton, 1992, p.12-108
[37] J.B. Cui et al., J. Appl. Phys. **88**, 3667 (2000)

CHAPTER 2 - TECHNIQUES AND INSTRUMENTATION

2.1 PHOTOELECTRON SPECTROSCOPY

2.1.1 Photoemission Theory

Ultraviolet photoelectron spectroscopy (UPS), x-ray photoelectron spectroscopy (XPS), x-ray diffraction (XRD) and scanning electron microscopy (SEM) were used in this study. In the case of UPS or XPS, the sample is irradiated with photons that have sufficient energy to liberate electrons from the surface via the photoelectric effect [1]. The electrons ejected from the surface have a kinetic energy **E** given by

$$E = h\nu - BE \tag{2.1}$$

where **hν** is the photon energy and **BE** is the electron's binding energy. It is the electric field component of the electromagnetic radiation that imparts energy on the electron enabling it to escape from the surface. The radiation may be treated as a plane polarized wave with an electric field component of the form [2]

$$\mathbf{E}(\mathbf{r},t) = E_0 e^{i(\mathbf{k}\bullet\mathbf{r}-\omega t)} \tag{2.2}$$

with the electric field related to the vector potential by

$$\mathbf{E}(\omega) = \frac{i\omega}{c}\mathbf{A}(\omega) \tag{2.3}$$

For a system of electrons in a solid, the Hamiltonian can be expressed as [3]

$$H = \frac{1}{2m}\sum_i \left(p_i + \frac{e}{c}\mathbf{A}(\mathbf{r}_i, t) \right)^2 + \frac{1}{2}\sum\nolimits'_{i,j} \frac{e^2}{\mathbf{r}_i - \mathbf{r}_j} + \frac{1}{2M}\sum_l P_l^2 + \frac{1}{2}\sum\nolimits'_{l,l'} W(\mathbf{R}_l - \mathbf{R}_{l'}) + \sum_{i,l} U(\mathbf{r}_i, \mathbf{R}_l) \quad (2.4)$$

where W is an unscreened potential between the ion cores of the solid. The quantity U is the interaction between electrons and ions (unscreened), M is the mass of the ions located at $\mathbf{R}_i$, with momenta $\mathbf{P}_l$. The electrons of mass *m* are located at coordinates $\mathbf{r}_i$ with momenta $\mathbf{p}_i$. This Hamiltonian may be expanded by Hartree-Fock calculations as $H=H_0+H_1+H_2$, where the unperturbed Hamiltonian (no radiation) is given by

$$H_0 = \frac{1}{2m}\sum_i \mathbf{p}_i^2 + \frac{1}{2}\sum\nolimits'_{i,j} \frac{e^2}{\mathbf{r}_i - \mathbf{r}_j} + \sum_l \frac{\mathbf{P}_l^2}{2M} + \frac{1}{2}\sum_{l.l'} W(\mathbf{R}_l, \mathbf{R}_{l'}) + \sum_{i,l} U(\mathbf{r}_i, \mathbf{R}_l) \quad (2.5)$$

and the first-order perturbation is given by

$$H_1 = \sum_i \left(\frac{e}{2mc}[\mathbf{p}_i \bullet \mathbf{A}(\mathbf{r}_i, t) + \mathbf{A}(\mathbf{r}_i, t) \bullet \mathbf{p}_i \right) \quad (2.6)$$

Since H_2 is second-order in **A** it becomes negligible for photoemission. If a photocurrent is to be calculated, the current density must be considered, such that the total current density operator can be expressed as

$$\mathbf{J}(\mathbf{r}) = \sum_i \mathbf{j}_i(\mathbf{r}) = \sum_i -\frac{e}{2m}\left(\mathbf{p}_i \delta(\mathbf{r} - \mathbf{r}_i) + \delta(\mathbf{r} - \mathbf{r}_i)\mathbf{p}_i\right) \quad (2.7)$$

where **J** is the sum of the single-particle current densities **j**, in which case the perturbation can be written as

$$H_1 = -\frac{1}{c}\int_\Omega d\mathbf{r}\mathbf{J}(\mathbf{r}) \bullet \mathbf{A}(\mathbf{r}, t) \quad (2.8)$$

with the integration over the volume Ω of the sample. If this first-order perturbation is applied to a single-particle approximation of eigenvalues ε_n corresponding to eigenfunctions |n⟩, then for a single-particle density matrix ρ_0, the eigenstates satisfy

$$\rho_0 \left| n \right\rangle = f_0(n) \left| n \right\rangle \tag{2.9}$$

where f_0 is a distribution function (the Fermi-Dirac distribution e.g.). If ρ_0 is the equilibrium density matrix, let ρ be the density matrix for a single particle in a radiation field which has the following equation of motion:

$$i\hbar \frac{\partial \rho}{\partial t} = [H_0 + H_1(t)\rho] \tag{2.10}$$

If ρ is expanded as series then the linear (ρ_1) and quadratic (ρ_2) terms satisfy the following equations

$$i\hbar = \frac{\partial \rho_1}{\partial t} = \left[H_0, \rho_1\right] + \left[H_1(t), \rho_0\right] \tag{2.11}$$

$$i\hbar = \frac{\partial \rho_2}{\partial t} = \left[H_0, \rho_2\right] + \left[H_1(t), \rho_1\right] \tag{2.12}$$

However the linear term contributes only to internal currents and not to photoemission; therefore the photocurrent density goes to zero for the linear term. The averaged photocurrent density may then be expressed as

$$J(\omega) = -\frac{e}{S}\frac{2\pi}{\hbar} \sum_{n.n'} f_n \left| \left\langle n \left| H_1 \right| n' \right\rangle \right|^2 \delta(\varepsilon_n + \hbar\omega - \varepsilon_{n'}) \tag{2.13}$$

This is known as the "Golden Rule" of photo emission [4] since it is expressed as a transition rate similar to Fermi's Golden Rule of time-dependent perturbation theory. Here, current density is a function of photon frequency ω incident on an area *S*. However, if this is expressed as a transition rate in terms of the electron wave vector **k**, then the Golden Rule for a one-electron rate of photon absorption becomes [5]

$$w_{n,n'} = \frac{2\pi}{\hbar}\frac{e^2}{m^2c^2}\frac{2V}{(2\pi)^3}\int\left|\mathbf{A}\bullet\mathbf{p}_{n,n'}(\mathbf{k})\right|^2\delta\left(\varepsilon_n(\mathbf{k})-\varepsilon_{n'}(\mathbf{k})-\hbar\omega\right)d\mathbf{k} \qquad (2.14)$$

where the integration is over one Brillouin Zone. There are several assumptions made in this model. Zero energy is taken to be the vacuum, and transitions are from the valence band *n'* to the conduction band *n*. A filled valence band and empty conduction band are assumed at T=0°K with no band bending at the surface. The quantum yield (in terms of electrons per photon) can then be expressed as the following ratio:

$$Y = \frac{\int'\sum_{n,n'}\left|\mathbf{A}\bullet\mathbf{p}_{n,n'}(\mathbf{k})\right|^2\delta\left(\varepsilon_n(\mathbf{k})-\varepsilon_{n'}(\mathbf{k})-\hbar\omega\right)d\mathbf{k}}{\int\sum_{n,n'}\left|A\bullet\mathbf{p}_{n,n'}(\mathbf{k})\right|^2\delta\left(\varepsilon_n(\mathbf{k})-\varepsilon_{n'}(\mathbf{k})-\hbar\omega\right)d\mathbf{k}} \qquad (2.15)$$

As is Eq. 2.13, the denominator is integrated over one Brillouin zone and the numerator is over all values of **k** which satisfy

$$\frac{\partial\varepsilon_n}{\partial k_x} > 0 \qquad (2.16)$$

This is the condition for escape from the surface where

$$\varepsilon_n(k) = \hbar^2\frac{(k_t^2+k_y^2)}{2m} \qquad (2.17)$$

with k_x is the wave vector in the solid, k_y the wave vector in the vacuum, and k_t is the wave vector tangential to the surface. This also assumes a direct transitions and no scattering of the electron current. Assuming a direct transition assumes that a hole exists at exactly the valence band maximum. Since this is generally not the case, transitions usually occur from a lower state in the valence band [6]. Because diamond is an indirect band gap material, these will be the dominant processes in this photoemission study. Indirect excitations are described by the "second-order" Golden Rule:

$$w_{n,n'} = \frac{2\pi}{\hbar}\sum_{n''}\left|\sum_{n'}\frac{\varepsilon_{n,n'}\varepsilon_{n',n''}}{E_n - E_{n'}}\right|^2 \delta\left(E_n - E_{n''}\right) \tag{2.18}$$

Here, the indices represent the unexcited crystal (*n*); an excitation by a photon produces a virtual electron-hole pair (*n'*), then a phonon or imperfection scatters the electron to the final state (*n''*). From this, the quantum yield can be calculated as in Eq. 2.14 for direct transitions. The yield is the ratio of $w_{n,n''}$ to $w_{n,n'}$ in Eq. 2.13. And similarly for the escape conditions, the momentum tangential (k_t) and normal ($k_{n'}$,$k_{n''}$) components satisfy

$$\varepsilon_n(k) = \left(\frac{\hbar^2(k_t^2 + k_y^2)}{2m}\right) \pm \hbar\omega \tag{2.19}$$

which is in the same form as Eq. 2.16 with the added constraint that $\pm\hbar\omega$ is positive for phonon emission and negative for phonon absorption. A direct consequence of this is the measurement of surface states in Sec. 3.6.

The depth to which photoelectron measurements can be made is a function of the electron's mean free path. As electrons are ejected from the sample's topmost atomic layers, they encounter collisions with atoms in the solid. For example, the mean free path

for carbon has been measured to be 9-10 Å [7]. While the accepted analysis depth for a surface technique such as XPS is typically on the order of 100 Å, due to the nature of its lattice structure, this value is less for diamond. Because diamond is a wide band gap semiconductor, photoemission takes place according to a three step process known as the Spicer model [8]. First, bulk electrons are photo-excited by the incident photon energy. Second, the electrons transport to the surface, and third, are ejected into the vacuum as "photoelectrons". For reference, the *vacuum level* for an electron is defined as the energy at rest at a point sufficiently outside the surface so that the electrostatic image force on the electron may be neglected – more than 100 Å [9]. This is simply when the electron has been freed from the surface and no longer experiences the periodic potential of the solid.

2.1.2 Hemispherical Energy Analyzer

The electron spectroscopy methods used in this study utilize a hemispherical energy analyzer for the collection of photoelectrons. The excited photoelectrons are focused by electrostatic lenses into an electrostatic (hemispherical) energy analyzer. The electrostatic analyzer consists of two concentric spheres of radii R_1 and R_2. The outer sphere is at a potential $-V_2$ while the inner sphere is at $+V_1$. The center line of the trajectory shown in Fig. 2.1with $R_0 = (R_1+R_2)/2$, is at a potential V. The potential along the path R_0 is known as the *pass energy E* of the analyzer.

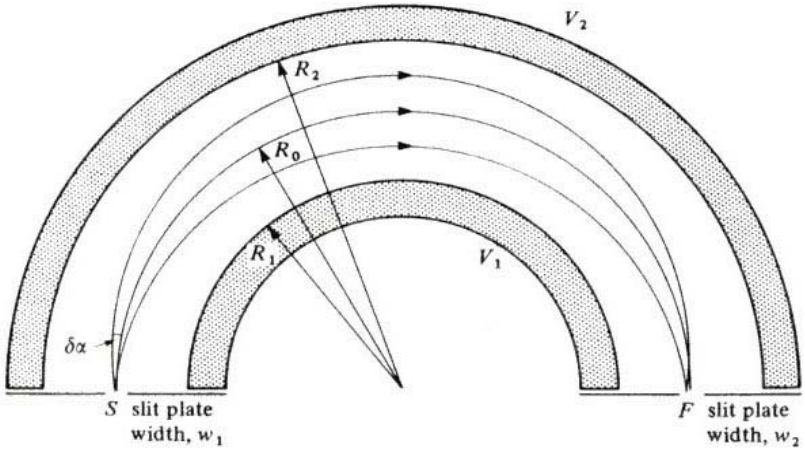

Fig. 2.1 Hemispherical Energy Analyzer

When photoelectrons enter the entrance slit *F* they are guided along trajectory R0 to the exit slit *S*. The electric field between the hemispheres is non linear (i.e. field lines are more dense near the inner hemisphere). In Fig. 2.2 the ESCA surface science system used in this study is shown.

Fig. 2.2 VG ESCA Lab Surface Science System

The hemispherical energy analyzer is pictured in the upper left. To calculate the resolution of the analyzer, take ΔE to be the FWHM of a distribution of a monochromatic beam. Then the resolution of the analyzer is $\Delta E/E$ given by [10]

$$\frac{\Delta E}{E} = \frac{\Delta r}{r} + \alpha^2 = \frac{w_1 + w_2}{r} + \alpha^2 \qquad (2.20)$$

Where r is the mean radius of the hemispheres, Δr is the shift along r, w_1 and w_2 are the slit widths, and α is the half angle of electrons entering the analyzer. Analyzers are typically designed such that $w_1 = w_2$ [11]. For the VG ESCALab II used in this study, the mean radius of the hemispheres is r = 150 mm. A 6mm slit width was used in all of the XPS and UPS data. The resolution was then controlled by the pass energy E. Before electrons enter the hemispheres, they pass through a lens system which acts to focus and magnify the image, and also to retard their kinetic energy to the pass energy. If the voltage on the hemispherical sections are held constant, the pass energy is constant and this is known as the constant analyzer energy (CAE) mode. This mode is commonly used for XPS and UPS, and has gives a fixed resolution for all energies. In the constant retard ratio (CRR) mode, the ratio of kinetic energy to pass energy is held constant, and this is usually used for Auger spectroscopy.

In this work, the inner and outer spheres are kept at a fixed voltage (CAE mode). In Fig. 2.3 the electrostatic focusing lenses, hemispherical analyzer and channeltron detectors are shown.

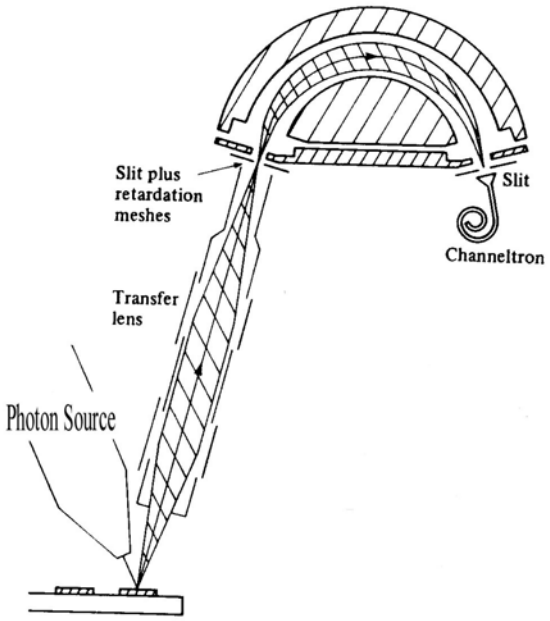

Figure 2.3 Energy Analyzer and Lens Elements

The channeltron detector in the VG surface science system includes three electron multipliers. Each multiplier contains a highly resistive coating inside of a glass tube to produce a secondary electrons cascade. The potential on the front end of the channeltron is the pass energy, and the exit voltage is adjustable up to 4 kV. This allows a gain of $10^4 – 10^6$ electrons from the input signal.

The measurements in such a system are usually performed under ultra-high vacuum (UHV) conditions. These low pressures are necessary for a number of reasons. The first is that the mean free path of the electrons traveling from the sample to the spectrometer must be greater than the dimensions of the analysis chamber in order to avoid interactions with background gases.

The mean free path is given by

$$\lambda = \frac{k_B T}{1.414 P \sigma} \tag{2.21}$$

where λ is the mean free path of the particle, k_B is Boltzmann's constant, T is the temperature, P is the pressure, and σ the collision cross section. Another reason for ultra–high vacuum (UHV) is the need to maintain a clean surface during analysis. It is often necessary to achieve an atomically clean surface to analyze, and the surface properties should not change over the course of the analysis. When a surface requires cleaning by ion sputtering, the surface may become oxidized by oxygen in the analysis chamber. The rate of adsorption is typically one monolayer per second at a pressure of 10^{-6} Torr. However in the 10^{-9} Torr range, the amount of time for a monolayer to adsorb on the sample surface is 1000 seconds. This pressure is sufficiently low to ensure the surface may be examined via XPS, UPS, etc. without significant interactions taking place between residual gas molecules and the sample surface. In addition, the instruments (channeltron detectors, ion pressure gauges, etc.) operate best under UHV conditions.

2.2 ULTRAVIOLET PHOTOELECTRON SPECTROSCOPY

2.2.1 UPS Theory

Ultraviolet photoelectron spectroscopy (UPS) provides a technique for measuring valence band electrons which are ejected via the photoelectric effect. This technique is more sensitive to the valence band because ultraviolet photons have a larger photoionization cross section than x-rays. The surface to be analyzed is irradiated with

photons of energy **hν** and electrons are ejected with kinetic energy **E.** This process allows the work function **Φ** to be measured by the relation

$$\Phi = h\nu - E \tag{2.22}$$

The photoelectrons are analyzed to measure their kinetic energy and thus the work function can be calculated. Equation 2.22 applies only if the process being studied is a one-step process (direct transition). If a two-step process (indirect transition) is studied, several different photon energies must be used. UPS typically utilizes a gas resonance or plasma lamp with a spot size of the order of 0.3-0.5 cm in diameter. Therefore, the information obtained is an average over that dimension. Therefore very small structures usually cannot be analyzed via UPS and it is often very helpful to have knowledge of the surface constituents beforehand. The photoemission distribution for UPS is a function of the angle of the incident radiation. For an electron with a total ionization cross section $\sigma_T(\varepsilon)$, the photoelectron intensity will be given by [12]

$$\frac{d\sigma(\varepsilon)}{d\Omega} = \frac{\sigma_T(\varepsilon)}{4\pi}\left[1 - \frac{\beta P_2(\cos\theta)}{2}\right] \tag{2.23}$$

where θ is the angle between the incident photon beam and the direction of the ejected photoelectron. The parameter β depends on the given orbital. For a spherically symmetric charge distribution, which is the case for the s-orbital, β=2.

In order to traverse a wide band gap, high-energy UPS is used, where photon energies may be as high as 40.8 eV (HeII line). In UPS only electrons in the valence orbitals are ejected. Prior to UPS analysis some knowledge of the sample is helpful in order to

identify the energies and ordering of occupied orbitals. With the presence of oxides and contaminants there are a variety of possible valances for a given surface which change its chemical environment significantly. While UPS may provide information about the band structure of the surface, it cannot identify the elemental composition. In this study, the surface constituents are well known and confirmed by XPS and XRD measurements.

2.2.2 UPS Instrumentation

The high-energy UPS instrument used in this study was a gas discharge plasma source where radiation was produced by a direct current discharge in a rare gas within a capillary of about 2 mm to obtain 21.2 eV photons. Other sources such as microwave lamps or synchrotron radiation may also be used. However, few laboratories have access to a synchrotron source which also requires the use of a monochromater due to the line width of the radiation. This is the reason the principal resonance lines of rare gases are desirable. While a number of gases can be used to create the plasma (H, Ar, O, N, Xe, and Kr e.g.), helium was used in this study. The HeI line at 584.3340 Å has an energy of 21.2175 eV [13]. The helium plasma discharge produces an intense beam of ~10^{12} photons/cm^2·sec and has a higher spectral purity than other gases. Fig. 2.4 shows a schematic diagram of the UV source used in this study.

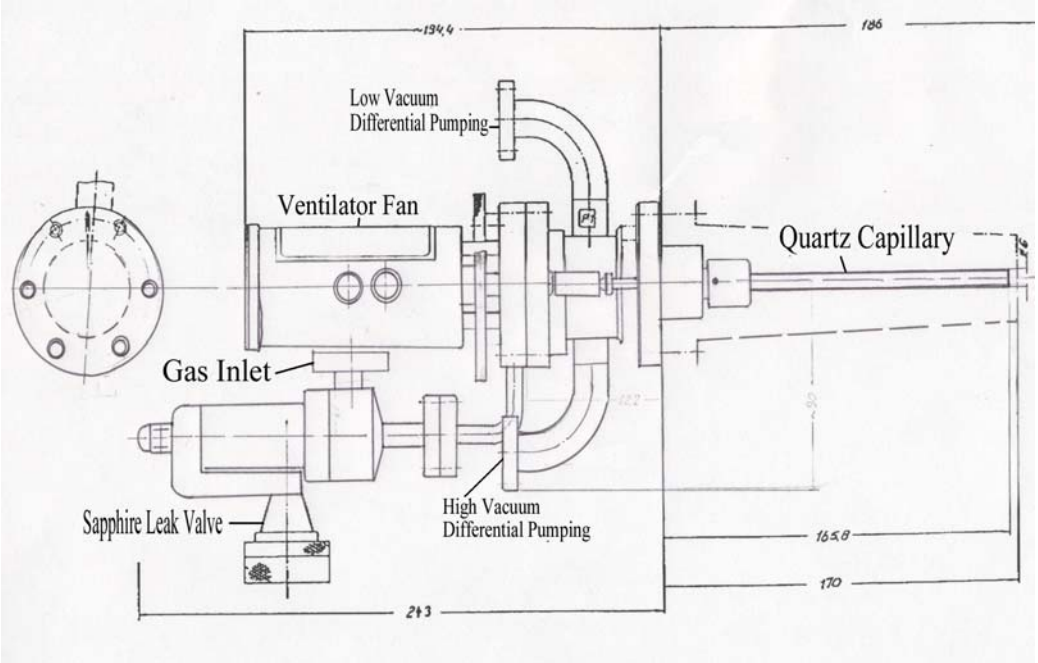

Fig. 2.4 Ultraviolet Radiation Source

Helium is introduced into the source through the gas inlet by a sapphire leak valve and enters the discharge chamber where a DC current of 1-5 kV creates a helium plasma. This produces photons from the first excited state that relax back to the ground state. Although currents of up to 150 mA can be obtained, we operated at 1-1.5 kV with a current of 80-90 mA. Differential pumping keeps the gas from absorbing the radiation and raising the pressure in the analysis chamber. There are two different pumping ports shown in Fig. 2.4 that have the low vacuum side at $\approx 10^{-4}$ Torr and the high vacuum side at 10^{-9} Torr. The radiation is directed by the capillary (about 2 mm in diameter and 10 cm in length). Although there is leakage into the chamber, the inlet pressure can be gradually reduced after the plasma has been achieved. For this reason pressures in the analysis chamber during UPS are typically an order of magnitude higher than base pressures.

The HeI line is produced via the 2p→1s transition that occurs 98% of the time. Under the proper conditions, the HeII line will be produced. To achieve HeII radiation, considerably higher discharge voltages are necessary (4-10 kV) with lower helium pressures.

Although the HeI line at 584.3340 Å is relatively monochromatic, there are factors which affect the line width of the radiation [14]. The following are a list of phenomena that contribute to the width of the energy distribution for a resonance line:

-*Pressure (Resonance) Broadening* - Line broadening can occur due to collisions between excited and non-excited atoms. This is a function of the pressure in the discharge capillary given by

$$\delta\lambda_T = \frac{3}{2\pi^2}\sqrt{\frac{g_1}{g_2}}\left[\frac{e^2 f}{8mc^2\varepsilon_0}\right]\lambda^3 N \tag{2.24}$$

where g_1, g_2 are statistical weights of the upper and lower states, f is the oscillator strength, ε_0 is the dielectric constant of free space, e is the electron charge, m the electron mass, and N is the particle density. In order to reduce this effect, the source should be operated at the lowest possible gas pressure that will maintain a plasma discharge. Pressure broadening is the most pronounced of the factors that affect the line width. This effect can be substantial in a resonance lamp operating at several atmospheres. However the plasma source used in this study is equipped with differential pumping that continually pumps helium from the discharge chamber. Under these conditions, pressure broadening is typically 10-15 meV.

-*Natural Linewidth* – This is a function of the lifetime of the excited state. It is given by

$$\delta\lambda_n = \frac{\lambda^2}{2\pi c\tau} \tag{2.25}$$

where τ is the mean lifetime of the state, $c = 3\times10^8$ m/s, and λ is the wavelength of radiation. For HeI emission this corresponds to $\delta\lambda_n \cong 3.0\times10^{-5}$ Å (10μeV).

-*Self Absorption* – This occurs when there are ground state helium atoms within the capillary that are excited by the resonant radiation from the discharge. The results is an increased full width half maximum (FWHM) of the line. Depending on the length of the capillary and the pressure in the discharge chamber, this value is typically less than 0.5 meV (half-width)/cm (capillary length) [15].

-*Doppler Effect* – The helium atoms (in the plasma) are of sufficient energy to cause a shift in the energy of radiation. The frequency shift is given by

$$\Delta\nu = \sqrt{\frac{2\ln(2)\nu^2 k_B T}{Mc^2}} \tag{2.26}$$

where *M* is the atomic (or molecular) mass. This effect is quite small under normal conditions ($\Delta\nu$ 3.6×10^{-3} Å).

-*Stark Effect* –Stark broadening may occur due to the weak electric field set up by the motion of electrons and ions in the plasma.

-*Self-Reversal* – This may result from temperature gradients in the plasma.

2.3 LOW-ENERGY ULTRAVIOLET PHOTOELECTRON SPECTROSCOPY

2.3.1 Surface State Theory

Surface states are electronic energy states that exist on the surface but not within the bulk of the solid. While their energies are not limited to the band gap, the states of interest in this study lie primarily in the band gap. Diamond has been shown to exhibit a number of surface states [16-19]. Measuring the states is not a function of photon energy (as in direct photoemission), the positions of the peaks remain constant for variable photon energies. The process is indirect and thus independent of the initial photon energy. Indirect transitions are assisted by phonons (lattice vibrations within the solid). Therefore a state that is at a discrete energy value below the conduction band is emitted by a phonon with the same energy regardless of how it gained the energy to reach the unfilled state in the band gap.

The density of states on the surface is different than for bulk electronic states because the bonding environment is different than in the bulk. The number of nearest-neighbor atoms, relaxation, reconstruction, and anisotropy of bonding can all give rise to new electronic states on the surface. To measure surface states, UPS may be performed at a grazing angle known as angle-resolved ultraviolet photoelectron spectroscopy (ARUPS), or a lower photon energy may be used. Both of these approaches provide for a technique that is more surface sensitive.

From a quantum mechanical standpoint, wave functions which describe electrons at the solid/vacuum interface allow for a more rigorous treatment of what constitutes a surface state. Assuming the solid has a periodic potential described by [20]

$$V(\mathbf{r}) = \begin{cases} \sum_n v(|\mathbf{r} - \mathbf{R}_n|) & \text{for z<0} \\ E_F + \Phi - \dfrac{e^2}{4(z + z_0)} & \text{for z>0} \end{cases} \tag{2.27}$$

which is for a semi-infinite crystal with z=0 the solid-vacuum interface. Here, E_F is the Fermi level, Φ is the work function, and z_0 is an adjustable parameter. The solution to the time-independent Schrödinger equation for the electron inside the solid is then

$$\Psi_B = \frac{1}{\sqrt{A}} \sum_{j=1}^{n} C_j \psi_j \tag{2.28}$$

where A is introduced as the surface area (L_2 for normalization), and ψj are the Bloch wave functions which decay exponentially into the solid, and C_j are constants to be calculated. On the vacuum side of the interface, the wavefunctions are given as

$$\Psi_V = \frac{1}{\sqrt{A}} \sum_g D_g \psi_{\mathbf{k}+\mathbf{g}}(\mathbf{r}) \tag{2.29}$$

where D_g are constants to be determined, **k** is the wave vector parallel to the plane, **g** is a generalized 2D wave vector, and $\psi_{k+g}(r)$ are defined as

$$\psi_{\mathbf{k}+\mathbf{g}}(\mathbf{r}) = e^{i(\mathbf{k}+\mathbf{g})\bullet\mathbf{r}} \phi_{\mathbf{k}+\mathbf{g}}(z) \tag{2.30}$$

The one-dimensional ϕ(z) must satisfy the 1D Schrödinger equation such that

$$\left(-\frac{\hbar^2}{2m} \frac{d^2}{dz^2} + V(z) \right) \phi_{\mathbf{k}+\mathbf{g}}(z) = \left(E - \frac{\hbar^2 (\mathbf{k}+\mathbf{g})^2}{2m} \right) \phi_{\mathbf{k}+\mathbf{g}}(z) \tag{2.31}$$

and $\phi(z)$ must also satisfy the boundary condition that $\phi(z)\rightarrow 0$ as $z\rightarrow\infty$. Once the wavefunctions for $z>0$ and $z<0$ have been established, continuity at the interface must also be satisfied. Setting the first derivatives of Ψ_B (bulk side) and Ψ_V (vacuum side) equal to zero and solving for the constants C_j and D_g, then they can be put into a matrix form such that

$$\Lambda(\mathbf{k};E)\mathbf{y} = \mathbf{0} \tag{2.32}$$

where $\mathbf{y}$ is a vector of 2n coefficients D_g and C_j, and $\mathbf{\Lambda}$ is a $(2n)\times(2n)$ matrix. A solution exists only if the determinant of $\mathbf{\Lambda}$ vanishes.

$$\det \mathbf{\Lambda}(E;\mathbf{k}) = \mathbf{0} \tag{2.33}$$

If this condition is satisfied for some value of E within the band gap for a given $\mathbf{k}$, then a surface state exists at this energy. This is often called a Shockley surface state because Shockley showed that the surface state is completely determined by the nature of the energy gap [21].

2.3.2 Low-Energy UPS Instrumentation

In this work an argon ion laser was used as the radiation source for low-energy UPS measurements. Through the use of a frequency-doubling crystal, a wavelength as low as 229 nm is obtained from the 458 nm fundamental line produced by the laser. This process known as second-harmonic generation (SHG) is achieved by a non-linear interaction. This process used a β-Barium Borate (BBO) crystal. As shown in the diagram of Fig. 2.5,

the temperature stabilized crystal must be kept dry at all times to avoid the absorption of water.

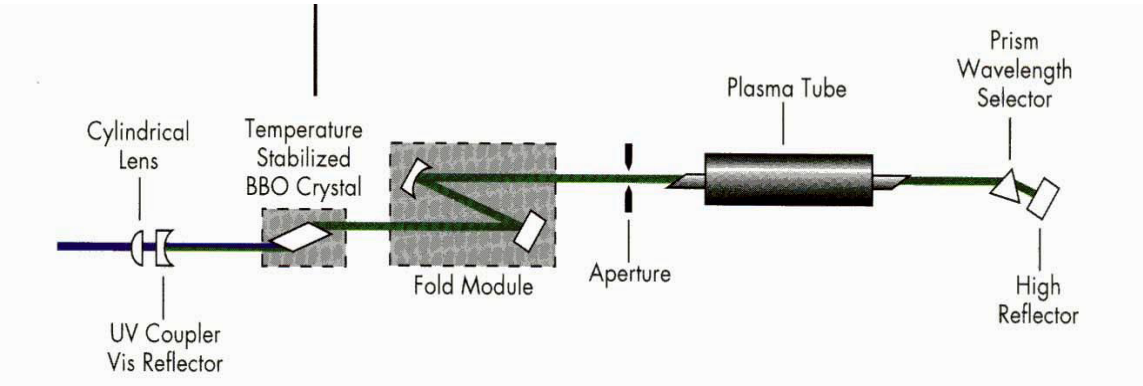

Fig. 2.5 Laser diagram

The laser system is equipped with an internal heater to prevent moisture forming on the crystal, and a constant nitrogen purge of Grade-5 (99.999% pure) N_2 is kept on the crystal at 0.5-1.0 SCFH (standard cubic foot hours).

Photon intensities from this source are on the order of 10^{17} photons/cm^2·sec. With such an intense beam, the high signal generated allows for very high electron energy resolution. And because the laser is steered into the analysis chamber with mirrors through a quartz window, the spectra may be taken at the base pressure of the chamber which is $\approx 8\times10^{-10}$ Torr. This is much lower than the 5×10^{-8} Torr pressure which is present during high-energy UPS analysis. As a result there is a much higher signal-to-noise ratio than with conventional UPS. This radiation source has a line width of the order of μeV that makes it possible to resolve very narrow structures.

The photon energy of the 229 nm line is 4.51eV. This line was used primarily, while the 351 nm line operating without a BBO crystal was also used in some low-energy UPS

measurements. The 351 nm line is achieved by operating in the high-tension single line UV mode. This is the lowest frequency attainable without the use of a frequency doubling crystal. While the photon energies of the laser fall below the 5.47 eV band gap of diamond, the purpose is to study surface states in the band gap of diamond. These can easily be verified by changing the photon energy and observing which peaks remain constant in their energy position. Such peaks are due to indirect transitions and are identified as surface states.

2.4 X-RAY PHOTOELECTRON SPECTROSCOPY

2.4.1 XPS Background

This is the most widely used of all surface characterization techniques. Also known as electron spectroscopy for chemical analysis (ESCA), x-ray photoelectron spectroscopy (XPS) provides qualitative and quantitative information about a surface. The presence of any element (except H and He) can be measured using XPS to about 0.1 atomic % [22].

When coupled with ion sputter etching, XPS is a valuable tool for depth profiling of thin films. An ion sputter gun creates a beam of ions (typically argon) and removes surface atoms by ion bombardment. The rate at which atoms are removed is a function of beam current, atomic mass of the surface atoms, and time of exposure to the beam.

By controlling these parameters, thins films can be removed from the surface, and XPS can be performed to characterize each subsequent layer. Because XPS does not penetrate deeply into the solid, it is very sensitive to the surface probing only a few

monolayers. Shown in Fig. 2.6 is a curve showing the electron's mean free path in a solid as a function of electron kinetic energy.

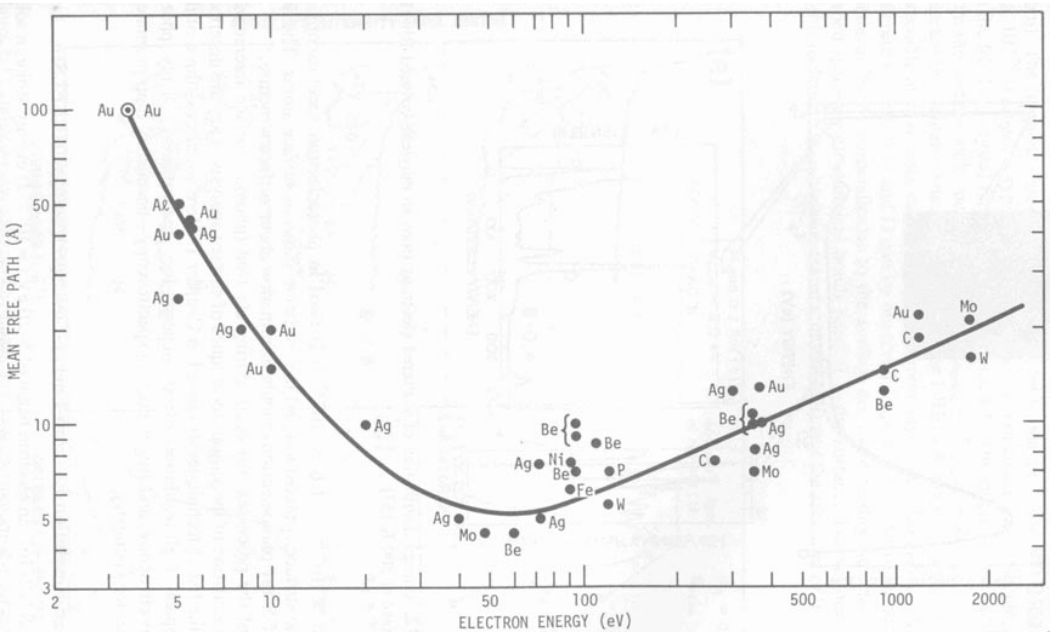

Fig. 2.6 Electron Mean Free Path vs. Kinetic Energy

Because x-rays bean ebergies for XPS are 1.2-1.6 keV, this translates into an escape depth of only 20-30 angstroms for most elements.

UPS (described earlier), is not used to obtain information about elemental composition because many valence shell orbitals have similar energies. Valence electrons are directly involved in bonding and very sensitive to their environment, but the core level electron energies measured by XPS are used to obtain atom's identity. Measuring core-level photoemission current gives the signature of that particular atom. These electrons undergo small changes because the valence shells participate in bonding. As the valence shells rearrange to accommodate for bonding, the entire orbital structure is afected. These changes are less than 5% for the binding energies of core level electrons whereas valence

shell energies may change as much as 20% during bonding [23]. This is why when a core level photoelectron is analyzed, it not only gives a signature of that particular atom but information about its chemical environment as well. In order to interpret the data, there are well known tables of standards used as reference for analyzing peaks [24]. Whether an energy shift is due to an oxygen bond, or another chemical species is well documented for many elements. In the case of oxidation (the most common chemical shift), this loss of negative charge (i.e. oxidation) is most often accompanied by a shift to higher binding energy.

2.4.2 XPS Instrumentation

The XPS source used in this study is a VG twin anode source as shown in Fig. 2.7

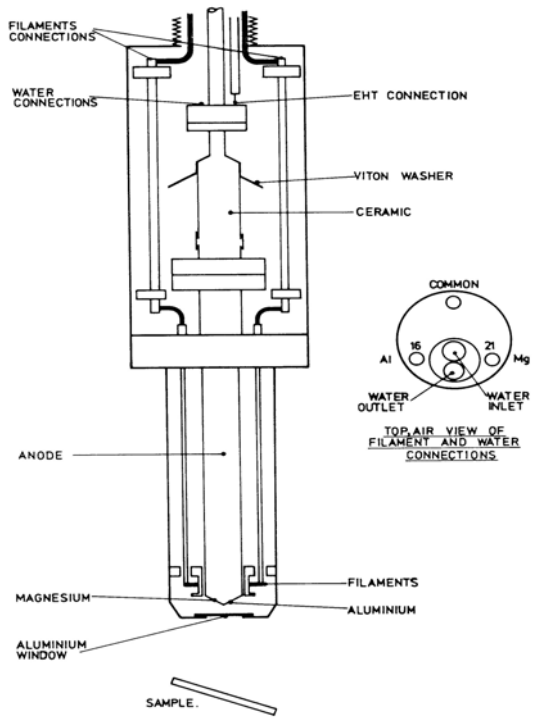

Fig 2.7 X-Ray Source

This source has the ability of utilizing either of two anodes to produce an x-ray beam of different energies. A filament produces electrons via thermionic emission that are accelerated to the anode target. The incident electron creates a vacancy in the anode material that gives rise to the emission of an x-ray. If the anode used is Magnesium, an average photon energy of 1253.6 eV is produced and if aluminum is used, the average x-ray energy is 1486.6 eV. Because an aluminum x-ray is higher energy than magnesium, it is widely used in order to observe higher binding energies and can thus be used to identify a wider range of elements. The aluminum $K_{\alpha 1}$ and $K_{\alpha 2}$ lines each have a width of 0.7 eV, giving a $K_{\alpha 1}$, $K_{\alpha 2}$ doublet of 1.0 eV at FWHM [25]. To reduce the source width some instruments employ the use monochromater.

When performing XPS, it is common to first run a "survey" scan over the entire range of the secondary electron energies. In the case of the Al source, energy steps of ½ eV up to 1486.6 eV would be used. This allows all possible binding energies within this range to be observed. The lower binding energy limit is usually 50-100 eV. This avoids the large amount of signal associated with unwanted low energy electrons. Once a survey scan has revealed the species present, a closer examination of particular peaks can be made. Resolving a single peak involves increasing the resolution (lower pass energy), using smaller step sizes, and performing numerous scans to improve the signal-to-noise ratio. Resolving a single peak (or two overlapping peaks) involves scanning a small window of energies that contain the structure of interest. There are a number of characteristics to be considered when interpreting the spectra. Photoelectrons are not the only signal that contributes to the energy distribution. There may be x-ray Auger lines,

satellites, ghost lines, and plasmon (energy loss lines). However these are also documented in reference manuals.

2.5 X-RAY DIFFRACTION

2.5.1 XRD Theory

This technique provides information for both crystalline and amorphous materials. In this study, the samples were polycrystalline diamond (sp^3 hybridized carbon). However, in the production of diamond films, it is also likely to produce diamond-like carbon as well as amorphous carbon (sp^2). This technique was employed in order to observe what forms of carbon were present. X-ray diffraction (XRD) is a process by which x-rays are scattered from a surface within a particular angular range then detected. The measurement involves detecting the relative intensity of the diffracted beam. Data is typically plotted as relative intensity vs. 2θ (in degrees). The radiation impinges on the target in small angular steps (often intervals of $2\theta = 0.05°$).

Although the x-ray source is identical in design to the sources described in the previous section on x-ray sources, the anode for XRD sources is typically copper. The Cu $K_{\alpha 1}$ line gives an energy of 8.04 keV ($\lambda = 1.54$nm) [26] that is considerably higher than the photons used in XPS ($\cong$1.5 keV). In a typical x-ray source, after the electrons collide with the anode target, only about 1% of the relaxations result in the emission of an x-ray. The majority of the radiation is non-radiative (electronic emission). Similar to the source used for XPS, the copper source also produces a doublet consisting of the $CuK_{\alpha 1}$ line

($2p_{3/2} \rightarrow 1s$) and the $CuK_{\alpha 2}$ line ($2p_{1/2} \rightarrow 1s$). The energy of the $K_{\alpha 1}$ is 8.045 keV while the energy of the $K_{\alpha 2}$ line is 8.025 keV [27]. However most instruments are equipped with a monochromater to allow only the $K_{\alpha 1}$ line as the radiation source. This may be accomplished by either filtering the radiation through a thin foil, or by diffracting the beam from a grating. For a copper anode, a thin nickel foil will block out the unwanted K_β radiation, and for a molybdenum anode, a zirconium foil is used.

A monochromatic beam may also be achieved by using a diffraction grating which operates on the same principle as the XRD technique. A single-crystal graphite diffraction grating can eliminate the K_β line by diffracting only the K_α radiation. The crystal is oriented in the apparatus such that only the desired wavelength is preserved.

At each interval, the diffracted beam may interfere constructively or destructively as given by Bragg's Law:

$$n\lambda = 2d\sin\theta \tag{2.34}$$

Here, λ is the wavelength of the incoming radiation, n is the order of the diffracted beam (typically n=1), d is the lattice spacing of the crystal, and θ angle of radiation with respect to the surface. Along most directions, there is no diffraction. This makes a distinction between diffraction and reflection. While reflection may occur at any angle, only radiation at certain angles with respect to the solid surface will result in the constructive interference which acts to diffract the beam. This technique is also quite surface-sensitive as each successive order of n represents diffraction from deeper atomic sites in the lattice. The strongest lines are the first order (n=1) as would be expected.

In a typical apparatus, the sample is rotated with respect to the x-ray source in small steps. At each step, the diffracted x-rays are then recorded. When these angles are recorded as peaks on a spectrum, they identify the crystalline structure of the surface. The positions of the peaks, the peak heights, and the width of the peaks all provide information about the crystalline structure of the sample. When the incident beam is compared to the diffracted beam there is a difference in the phase of the two waves. Upon being diffracted from the surface atoms and the first few atomic layers, there is a shift in the emerging radiation which is a function of the depth at which it is diffracted. The diffracted beam is shifted by integer multiples of $2dsin\theta$ as shown in Fig. 2.8.

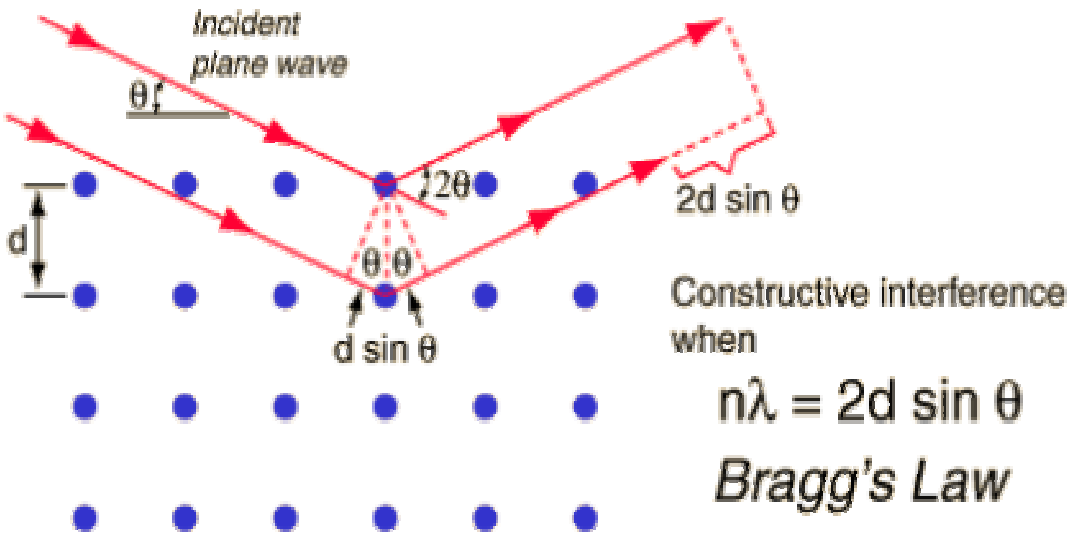

Fig. 2.8 Bragg's Law

Along specific crystal directions (crystal facings), constructive interference occurs. The signal is detected when incident x-rays produce an electron-hole pair generating a measurable pulse. This process may take place in a proportional, scintillation, or solid state detector [28]. To identify the surface structure, there are extensive data bases at our

disposal which identify the peak positions. Standard values are known for the peak positions of most crystalline surfaces and programs exist [29] for fitting data of unknown species.

The most important information provided by XRD to this study is the identification of the crystal planes present on the surface. Unless the crystal is specially prepared such that it is grown with a particular facing, there are typically a number of faces present, especially in polycrystalline powders such as used in this study.

The Miller index (hkl) of a plane can be obtained from the angular spectrum by

$$\sin^2\theta = \frac{\lambda^2}{4a^2}\left(h^2 + k^2 + l^2\right) \tag{2.35}$$

where the radiation wavelength λ and lattice spacing *a* are constant for any one sample. Once the lattice parameter is calculated from the peak positions, the pattern can be indexed for the (hkl) values. The Bravais lattice may be identified by using selection rules for cubic lattices. There is a pattern such that the sum $h^2+k^2+l^2$ follows the given sequences:

Primitive: 1, 2, 3, 4, 5, 6, 8, 9, 10, 11, 12, 13, 14, 16, …
Body-Centered: 2, 4, 6, 8, 10, 12, 14, 16, …
Face Centered: 3, 4, 8, 11, 12, 16, 19, 20, 24, 27, 32, …

For the face-centered cubic (fcc) structure, h,k, and l are unmixed (i.e. they make take on any of these values such that they are all even or all odd). As mentioned in Section 1.3, the (111) surface of diamond has been shown to exhibit a NEA. Therefore, it was essential to determine the amount of (111) diamond present on the surface as a ratio of

the total diamond surface. Having a prior knowledge of the sample material is advantageous because a search of the spectra data base will easily return the peak positions for various forms of diamond. Numerous XRD studies are available for both synthetic (chemical vapor deposition) and natural diamond samples. The diamond powders used in this study were processed using a high-temperature/high-pressure process (CVD).

2.5.2 X-Ray Diffractometer

The instrument used for all XRD measurements was a Seimens F-Series x-ray diffractometer as pictured in Fig. 2.9.

Fig. 2.9 X-Ray Diffractometer

The instrument uses a copper anode, and is equipped with a monochromator providing monochromatic radiation of the $K_{\alpha 1}$ line at 8.04 keV. Taking into consideration the position of diamond and other carbon peaks, the angular range for all measurements was from $2\theta = 20°$-$100°$. This range includes the predominant structures for any carbon species that may be present on the surface.

2.6 SCANNING ELECTRON MICROSCOPY

2.6.1 SEM Theory

The scanning electron microscope (SEM) allows an image to be viewed from 10 to 200,000 times magnification with as much as 5 nm resolution. In order to view a sample, it must be electrically conductive. However samples non-conductive may be coated with gold or carbon in a sputter coating machine. This provides a thin conductive layer which allows for the sample to have an electrical ground as well as scatter the incident electrons forming the image. This layer can be thin enough so that it does not affect the features of the sample surface.

In addition, because the SEM chamber is under vacuum (10^{-5} –10^{-7} Torr), the samples that may be subject to out-gassing cannot be used because it would compromise the vacuum conditions. An electron beam is focused by condensing lenses, while the objective lens focuses the beam onto the sample. Scanning coils direct the beam across the sample in a back and forth rastering motion over the area of interest. A schematic of the lens system is shown in Fig. 2.10.

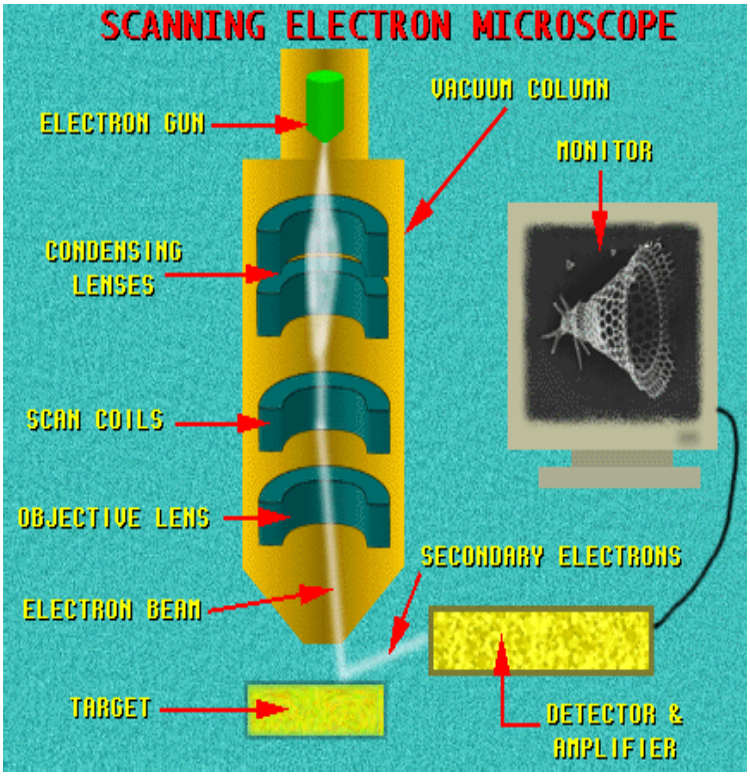

Fig. 2.10 Scanning Electron Microscope Diagram

The number of secondary electrons reaching the detector is a function of the deflection angle and determines the brightness at that location. This allows the topography of the surface to be observed.

2.6.2 Scanning Electron Microscope Instrumentation

The instrument used for all of the grain size measurements was a JEOL JMS-T300 Scanning Electron Microscope as pictured in Fig. 2.11.

Fig. 2.11 JOEL JMS-T300 Scanning Electron Microscope

An accelerating voltage of 20 kV was used on all samples with the vertical separation set for slightly higher resolution. For normal work, a setting of 15 is used (as measured by the micrometer on the manipulator) and the settings used were 12-14 in this study. Magnification varied with grain size, the larger sizes were easily imaged using 2000×, while the smallest grain sizes were imaged at 5000 and 7500 magnification.

2.7 ELECTROCHEMISTRY THEORY

In order to deposit the diamond films onto molybdenum substrates, an electrochemistry technique was employed. This method has been demonstrated to be

effective in coating molybdenum field emitters with colloidal diamond powder in a dielectric solution [30]. Electrophoresis is defined as the movement of charged particles suspended in a liquid under the influence of an applied electric field [31, 32]. A direct current (DC) electric field is applied within a liquid in which the particles are suspended. Once the DC field is applied, the particles establish a steady state in which they migrate at a constant velocity. Negative ions migrate toward the anode and positive ions are attracted to the cathode. This steady state condition is established when the electrical force acting on the particles is balanced by the frictional force of the solution given by the Stokes equation

$$f = 6\pi r v^2 \eta \tag{2.36}$$

where **r** is the radius of the particle, **v** is the velocity and **η** is the viscosity of the medium. There are a total of four forces acting on a particle which is in electrophoretic motion [33]. The first is the Coulombic force of the DC field on the charge **F** = q**E,** where q is the effective charge of the ion and **E** is the electric field. This is the only force which acts to migrate the particle to electrode of opposite polarity; the other three forces oppose this motion. The second is the Stokes friction force of Eq. 2.5. that depends on the viscosity of the medium. The third and fourth forces are due to the electrolyte ions in the solution. Near the colloid particle, the ions give the solution a net charge opposite that of the particle. This is known as the "ionic atmosphere". The 3rd force known as electrophoretic retardation, is a force acting on the colloidal particles due to the ions in the solution responding the electric field. The relaxation effect is the 4th force which is caused when the field is first applied and the particles in the solution move away from the center of the

ion atmosphere. Both of these last two forces can be described by the Debye-Huckel theory of the conductivity of strong electrolytes [34], and typically are negligible effects.

The electrophoretic mobility is given by

$$m = \frac{v}{E} \tag{2.37}$$

which is a function of the particle's velocity (**v)** under the applied field (**E)**. This velocity may also be expressed in terms of the current density (**J**) and conductivity (**σ**) of the medium, where

$$v = mE = \frac{mJ}{\sigma} \tag{2.38}$$

The pH of the environment can affect the net charge on a particle which in turn will influence its mobility. The mobility is inversely proportional to the square root of the ionic strength of the solution. The ionic strength affects the electrokinetic potential which reduces the net charge on the particles to their effective charge. Although a lower ionic strength will give a higher migration, this may cause unwanted changes in the temperature of the solution from joule heating. These temperature gradients can then cause changes in the conductivity and viscosity of the solution [35]. Electrophoresis is most commonly used for the separation of two species, which arises from the differences in mobilities given their differing charges. Rather than performing electrophoresis in a free solution, a stabilizer is introduced to avoid joule heating which also causes density gradients and convection flows [36]. Both of which are undesirable effects in this process because they can effect the behavior of the colloidal particles.

2.8 THERMAL DESORPTION

2.8.1 Adsorption Theory

The process that involves trapping of atoms (or molecules) incident on a surface is known as adsorption. The reference to "atoms" in this section will refer to atoms or molecules interchangeably. Adsorption may occur with gaseous or liquid phase atoms interacting with the solid surface, however the gas phase is typically the most commonly studied phenomenon in surface science as oxides etc. are investigated. When an atom interacts with a solid surface, it resides on the surface for a time τ given by [37]

$$\tau = \tau_0 \exp\left(\frac{\Delta H_{ads}}{RT}\right) \tag{2.39}$$

where ΔH_{ads} is the heat of adsorption. When an atom is adsorbed to a surface heat is given off. By thermodynamic convention, exothermic processes are usually designated by a negative sign. However in this work, it has been taken to be positive. When an atom initially contacts a surface, a significant amount of movement occurs along the surface before adsorption takes place (if adsorption takes place). Because the activation energy for surface diffusion is much lower than that for diffusion into the bulk or desorption, atoms may easily diffuse along the surface before bonding to a surface atom.

The coverage of a surface is a function of the flux of gas molecules F striking the surface as well as the resident time, where the surface coverage (molecules/cm^2) is given by

$$\sigma = \tau F = \frac{N_A P}{\sqrt{2\pi MRT}} \tau_0 \exp\left(\frac{\Delta H_{ads}}{RT}\right) \tag{2.40}$$

which shows the coverage proportional to pressure P and inversely proportional to the square root of molecular mass M. As adsorption occurs however, less sites are available for adsorption, or the adsorption of additional layers involves different activation energies. A simple model for adsorption of one monolayer could represent σ_0 as a completely covered surface. The available sites are then $\sigma_0 - \sigma$, where a fraction of the total flux $\frac{\sigma}{\sigma_0} F$ would be reflected from occupied sites. The fraction of the surface then left available for adsorption would be $\left(1 - \frac{\sigma}{\sigma_0}\right) F$. Modifying Eq. 2.40, yields

$$\sigma = \tau F = \left(1 - \frac{\sigma}{\sigma_0}\right) \frac{N_A P}{\sqrt{2\pi MRT}} \tau_0 \exp\left(\frac{\Delta H_{ads}}{RT}\right) \tag{2.41}$$

Making the substitution $\theta = \frac{\sigma}{\sigma_0}$ and $b = \frac{F\tau}{\sigma_0 P}$, the degree of coverage θ is given by [38]

$$\theta = \frac{bP}{1 + bP} \tag{2.42}$$

where the degree of coverage θ is for one monolayer.

2.8.2 Physisorption

When an atom adsorbs onto a surface, it may bond in one of two ways: physical adsorption (physisorption) or chemical adsorption (chemisorption). The former is the weakest for of adsorption and is not a true chemical bond to the surface. The adsorption

is due to the weak interaction known as a van der Waals attraction. In such a case, there is an attraction between the polarizable solid and the atomic charge distribution (dipole) of the atom. This is best modeled by considering the atom's image charge [39] in the solid as shown in Fig. 2.12.

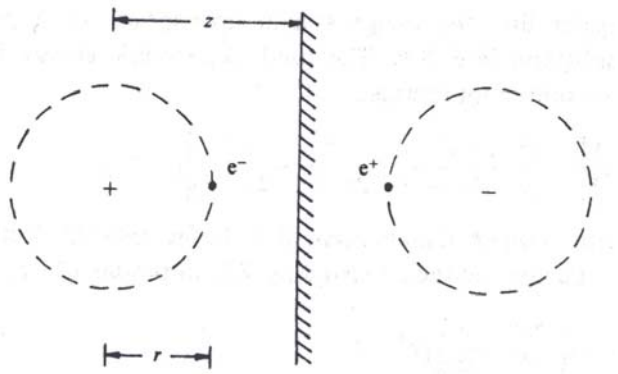

Fig. 2.12 Image Charge of Atom in Substrate

Considering a perfectly conducting substrate, the electrostatic energy of this configuration can be expanded in a series of r/z such that [40]

$$U = \frac{1}{2}\left[-\frac{e^2}{2z} - \frac{e^2}{2(z-r)} + \frac{e^2}{2z-r} + \frac{e^2}{2z-r}\right] = -\frac{1}{8}\frac{e^2 r^2}{z^3} - \frac{3}{16}\frac{e^2 r^3}{z^4} - \cdots \quad (2.43)$$

The van der Waals effect is dominated by the z^{-3} term in which the force can be expressed in terms of $V(z) = -\frac{C_V}{z^3}$. In order to calculate this constant of proportionality, it is necessary to include the ability of the substrate and the atom to polarize one another.

For a dielectric substrate, the polarization of the image can be written in terms of the atom's polarization such that

$$\mathbf{P}_{image}(\omega) = \frac{1-\varepsilon(\omega)}{1+\varepsilon(\omega)}\mathbf{P}_{atom}(\omega) \tag{2.44}$$

On a microscopic scale, the constant of proportionality can be evaluated as

$$C_V = \frac{\hbar}{4\pi}\int_0^\infty \alpha(\omega)\frac{\varepsilon(i\omega)-1}{\varepsilon(i\omega)+1}d\omega \tag{2.45}$$

which allows a general expression for the van der Waals interaction

$$V(z) = -\frac{1}{z^3}\frac{\hbar}{4\pi}\int_0^\infty \alpha(\omega)\frac{\varepsilon(i\omega)-1}{\varepsilon(i\omega)+1}d\omega \tag{2.46}$$

In physisorption, the adsorbate-adsorbate interactions dominate over the adsorbate-substrate interactions. As a result, the adsorbed layer may have an independent lattice structure from the substrate. A chemisorbed species can best be described by a potential energy diagram similar to the model used for binding energy of an electron in an atom. The potential minima are shallow in physisorption compared to those of true chemical bonds (such as chemisorption). Shown in Fig. 2.13 are physisorbed potential energy wells for He near the surfaces of Ag, Cu, and Au. [41]

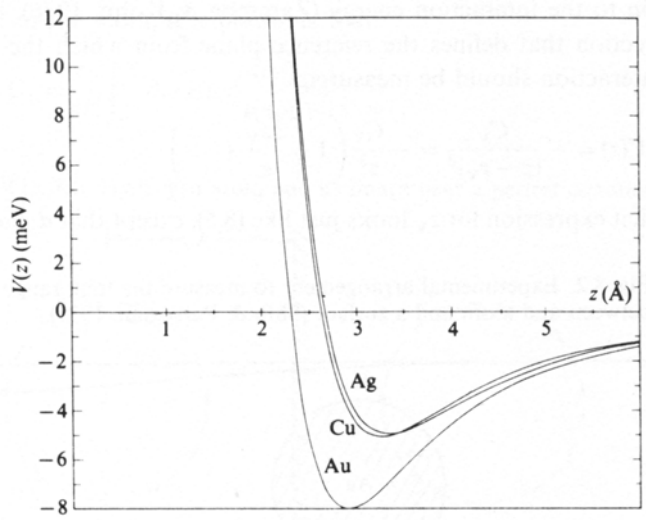

Fig. 2.13 Physisorption Potential Energy Diagram

The minimum may also be interpreted as the heat of physisorption (or heat of adsorption in general) for that particular species.

2.8.3 Chemisorption

In chemical adsorption (chemisorption) a true chemical bond is formed. Unlike physisorption, the interaction between the adsorbates and the substrate is dominant, and the adsorbed layer configures itself to the lattice structure of the substrate. However when an atom chemisorbs onto a surface, there is reconstruction of the substrate in the vicinity of the adsorbed atom. In the case of chemisorption on semiconductors, the adsorption sites occur at dangling bonds. Langmuir (1916) described the surface as a Chinese checkerboard which defines specific sites for potential adsorption. Atoms incident on the surface may either be reflected or bind to a site forming a chemical bond. The potential

energy diagram for chemisorption is shown in Fig. 2.14 where an additional barrier is present indicating the more tightly bound adsorbate.

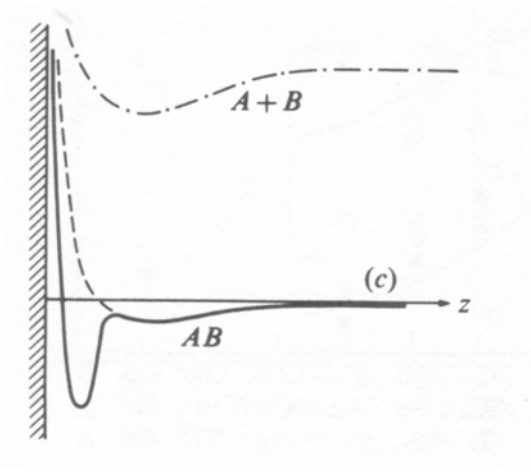

Fig. 2.14 Chemisorption Potential Energy Diagram

Shown here is the case where the adsorbate directly forms an immediate molecular bond. Dissociative chemisorption may also occur whereby an O_2 molecule e.g. dissociates at the surface allowing the individual oxygen atoms to bond at separate sites. Shown in Fig. 2.15 is the superposition of the physisorption and chemisorption potential energy curves.

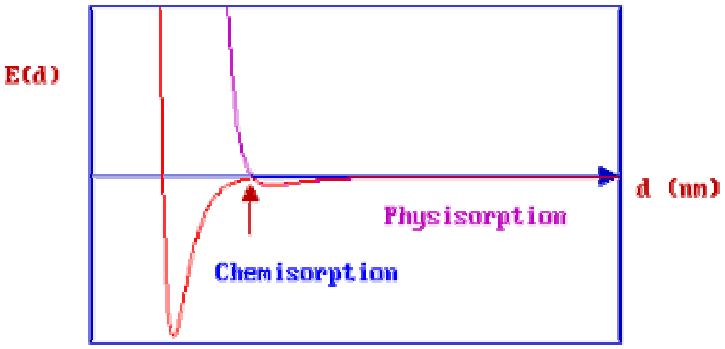

Fig. 2.15 Chemisorption and Physisorption Potential Energy Curves

Note the deeper potential well in the chemisorption curve indicating a much stronger bond than the shallow well from the van der Waals interactions of the physisorbed species. When dealing with semiconductors, the formalism of Section 8.1 requires some slight modification to account for dopants and space charge layers. For instance, in the case of having positive donor ions at the surface, they create an electric field within a depletion layer of thickness z_0. Within the space charge layer, Poisson's equation is

$$\frac{d^2V}{dz^2} = -\frac{4\pi e N_d}{\varepsilon} \tag{2.47}$$

where ε is the dielectric constant of the semiconductor, and N_d is the concentration of dopants. The potential then becomes

$$V(z) = V_{bulk} - \frac{2\pi e N_d}{\varepsilon}(z - z_0)^2 \tag{2.48}$$

This parabolic potential changes the energy levels at and around the surface. The response of crystal is band bending at the surface. Therefore, in addition to the work function Φ, the surface also has an electron affinity χ, and band bending V. Because the (111) diamond surface has shown to exhibit chemisorbed hydrogen, thermal desorption studies were performed and detailed in Section 3.5

REFERENCES

[1] A. Einstein, Annalen der Physik, **17**, 132-148 (1905)
[2] Mark A. Heald and Jerry B. Marion, *Classical Electromagnetic Radiation 3rd ed*., Saunders College Publishing, Fort Worth 1995
[3] B. Feuerbacher, B. Fitton, and R. F. Willis ed., *Photoemission and the Electronic Properties of Surfaces*, Wiley & Sons, Ltd., Chichester, 1978
[4] W.L. Schaich and N. W. Ashcroft, Phys. Rev. B **3**, 2452 1971
[5] Evan O. Kane, Phys. Rev. **127**, 131 (1962)
[6] C. N. Berglund and W. E. Spicer, Phys. Rev. **136**, A1030 (1964)
[7] H. Ibach, *Electron Spectroscopy for Surface Analysis*, Springer-Verlag: New York, 1977
[8] W.E. Spicer, Phys. Rev. **112**, 114 (1958)
[9] C. Kittel, *Introduction to Solid State Physics*, Wiley & Sons Inc., Brisbane, 1996 Wiley-Interscience, New York, 1977.
[10] C. E. Kuyatt and J. A. Simpson, Rev. Sci . Instr. **38**, 103 (1967)
[11] D. Briggs and M.P.Seah, *Practical Surface Analysis*, John Wiley & Sons Inc., Chichester, 1995
[12] Thomas A. Carlson*, Photoelectron and Auger Spectroscopy*, Plenum Press, New York, 1975, Chap. 3.
[13] J.W. Rabalais, *Principles of Ultraviolet Photoelectron Spectroscopy*, John Wiley & Sons, New York, 1977.
[14] H. R. Griem, *Plasma Spectroscopy*, McGraw-Hill, New York, 1964.
[15] J. A. R. Samson, Rev. Sci. Instr. **40**,1174 (1969)
[16] A. A. Rouse, J. B. Bernhard, E. D. Sosa, and D. E. Golden, Appl. Phys. Lett. **75**, 3417 (1999)
[17] N. M. Miskovsky, P. H. Cutler, and Z. H. Huang, J. Vac. Sci. Technol. B **14**, 2037 (1996)
[18] Glenn D. Kubiak and Kurt W. Kolanski, J. Vac. Sci. Technol. A **6**, 814 (1988)
[19] B. B. Pate, *et al*., J. Vac. Sci. Technol. **19**, 349 (1981)
[20] A. Modinos, Field*, Thermionic, and Secondary Electron Emission Spectroscopy*, Plenum Press, New York 1984
[21] Andrew Zangwill, *Physics at Surfaces*, Cambridge University Press, Cambridge 1988
[22] J.C. Vickerman *Surface Analysis – The Principal Techniques,*. John Wiley & Sons: Chichester, 1993, Chap.3
[23] A.D. Baker, *Photoelectron Spectrsocopy*, Pergamon Press, Oxford 1972 Chap. 5
[24] C.D.Wagner et al., *Handbook of X-ray Photoelectron Spectroscopy*, Perkin-Elmer Corporation, 1979.
[25] K. Siegban *et. al*., *ESCA – Atomic, Molecular and Solid State Structure Studied by Means of Electron Spectroscopy*, Uppsala 1967.
[26] C. Suryanarayana and M. Grant Norton, *X-Ray Diffraction – A Practical Approach,* Plenum Press New York, 1998.

[27] Ron Jenkins, *Introduction to X-ray Powder Diffractometry*,
John Wiley & Sons, New York, 1996.
[28] B.D. Cullity, *Elements of X-Ray Diffraction*, Addison-Wesley,
Reading, Massachusetts 1978.
[29] See for example JADE software, Materials Data Inc., 1224 Concannon Blvd., Livermore, California 94550
[30] W. B. Choi, *et al*., J. Vac. Sci. Technol. B, **16** (1998)
[31] Milan Bier, *Electrophoresis – Theory, Methods and Applications Vol. 1*, Academic Press Inc., New York, 1959
[32] Milan Bier, Electrophoresis – *Theory, Methods, and Applications Vol. 2*, Academic Press Inc, New York 1967
[33] P. Debye and E. Huckel, Ann. D. Physik. Z., **24**, 305 (1924)
[34] Anthony T. Andrews, *Electrophoresis – Theory, Techniques, and Biochemical and Clinical Applications*, Clarendon Press, Oxford 1986
[35] James W. Jorgenson ed. And Marshall Phillips ed., *New Directions in Electrophoretic Methods*, American Chemical Society, Washington D.C. 1987
[36] Z. Deyl ed., *Electrophoresis – A Survey of Techniques and Applications, Part A: Techniques*, Elsevier Scientific Publishing Co., Amsterdam, 1979
[37] Gabor. A. Somorjai, *Introduction to Surface Chemistry and Catalysis*, John Wiley & Sons, Inc., New York, 1994
[38] S. Roy Morrison, *The Chemical Physics of Surfaces 2nd ed*., Plenum Press, New York, 1990
[39] J. D. Jackson, *Classical Electrodynamics 3rd ed*., John Wiley & Sons, Inc., New York 1998
[40] E. Zaremba and W. Kohn, Phys. Rev. B **13**, 2270 (1976)
[41] E. Zaremba and W. Kohn, Phys. Rev. B **15**, 1769 (1977)

CHAPTER 3 - EXPERIMENTAL RESULTS

3.1 SAMPLE PREPARATION

3.1.1 Film Deposition

Polycrystalline diamond powders were obtained commercially in various grain sizes. The films were deposited onto a molybdenum substrate via electrophoresis. A grounded array of six molybdenum field emitters was used as the cathode for the electrophoresis. Field emission tips were used because the sharpness of the molybdenum tips enhances the electric field used for coating. The anode was a 1cm×1cm molybdenum foil 0.1mm thick of 99.95% purity. Prior to deposition, the foils were polished with 180 grit carbon paper to increase surface roughness. The foils were then rinsed in acetone and allowed to air dry.

Film deposition was performed in a 10% ethanol solution of 18MΩ·cm ultra-pure water, and approximately 6 grams of diamond powder per 200 ml of solution. The solution was found to be slightly acidic with a pH of 5.52 as measured by a Corning pH meter 320. Buffer solutions of pH 7 and pH 10 were used to calibrate the meter prior to measuring the electrolytic solution. The pH was measured before, during and after the deposition process, and remained constant throughout.

In order to expedite the coating process, the Mo foil anode was facing upward in the solution with the emitter array directly above at a separation of 3mm from the tips to the

foil. After mixing the solution using a stirbar, an even coating of the diamond powder was allowed to settle onto the foil at which point +600V was applied to the foil. The voltage used was higher than that used in the procedure for coating a field emission micro-tip. The larger potential difference was necessary in order to create the high fields needed to deposit the particles onto the flat substrate. The concentration of field lines is greater on the tip than the plane (substrate) therefore this was determined to be a sufficient voltage for deposition onto the molybdenum foils. In using this procedure, the concentration of diamond powder in the solution is not crucial provided there is sufficient coverage on the substrate for deposition. Shown in Figure 3.1 is the apparatus where colloidal diamond is beginning to settle in the solution with a layer on the substrate which is facing upward.

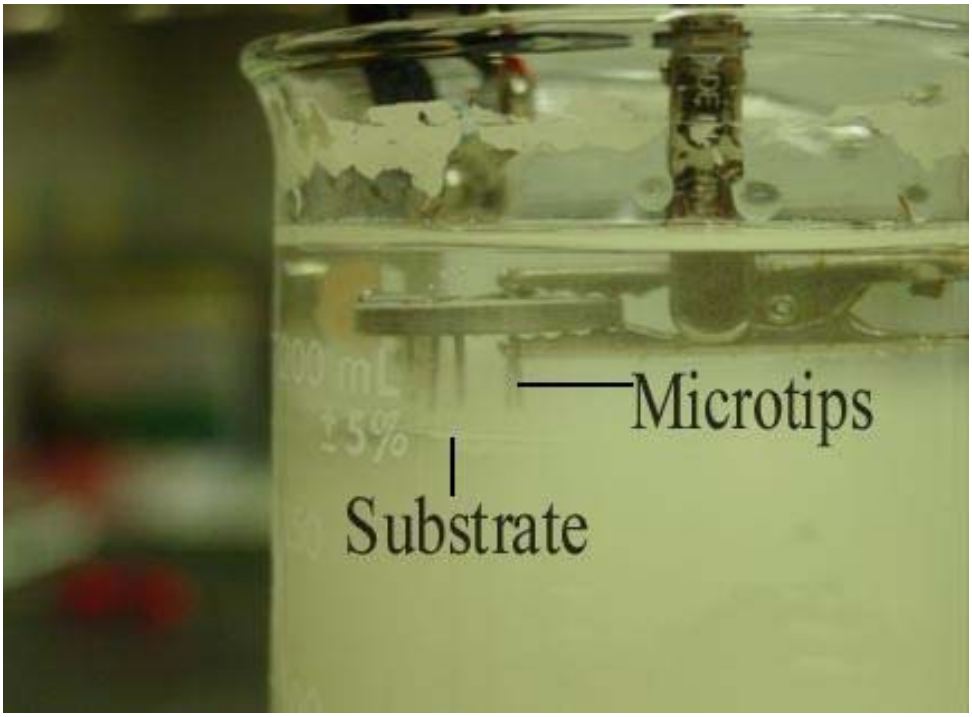

Fig. 3.1 Electrophoresis Apparatus

All of the coating times were for 1 hour. This was to insure that each molybdenum substrate would have a comparable oxide formation on the surface. Molybdenum readily forms two oxides: MoO_2 and MoO_3 . Molybdenum dioxide has a work function of 5.2 eV while molybdenum trioxide has a work function of 3.8 eV. Therefore, with pure molybdenum having a work function of 4.6 eV [1], it was necessary to insure a consistent Fermi level among the substrates. Because the foils are not pure molybdenum (they contain oxides and trace impurities), the Fermi level of the substrate may be offset from the valence band maximum. In addition, the samples were on molybdenum platform in contact with a nickel mounting peg in contact with the spectrometer. The contact of these dissimilar metals affects the Fermi level at the surface such that it is different from the level when it is isolated. Therefore calibration is needed to properly plot the photoelectron yield with respect to binding energy. In order to determine the Fermi level offset, bare molybdenum foils were subjected to the same electrolytic process as used for film deposition. The Mo substrates were biased at +600V with the anode array grounded for times of one hour in a 10% ethanol solution (the same conditions used in film deposition). By then measuring the UPS threshold of these bare molybdenum foils, the Fermi level offset was found to be 1.7 eV above the valence band maximum. All of the UPS data in this study reflects this compensation such that the Fermi level is shifted to zero binding energy.

3.1.2 Sample Mounting

After coating, the samples were allowed to air dry. The samples were then mounted onto a specially prepared Mo sample mount. Utilizing a conventional Ni / Fe sample peg used in the VG ESCAlab system, a molybdenum disk (99.95% pure) 1" in diameter and 0.060" in thickness was mounted on the peg. The disk has 8 drilled holes at different radii for securing various-sized samples using 0.25mm molybdenum wire (99.95% pure). The molybdenum foil was in intimate contact with the stage as well as the wire providing a conducting path ensures that the sample is properly grounded to the spectrometer.

In Figure 3.2 two sample mounts are shown with a diamond flat sample mounted on the stage via molybdenum wire.

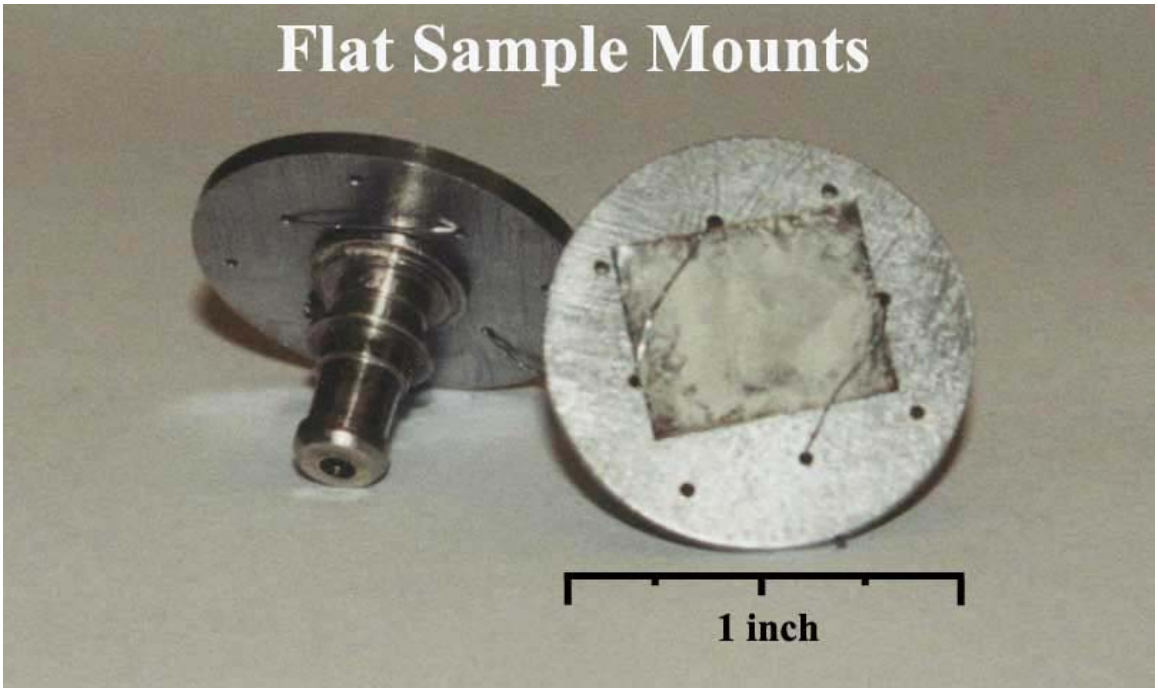

Figure 3.2 Sample Mounts for ESCA System

The conventional technique of mounting samples for use in the VG ESCA system has been to secure them directly to the peg using a silver-based paste that holds the sample in place while providing a conducting path for grounding the sample. However, this process would render the samples difficult to work with in further analysis when the sample was removed. Because the samples were annealed to above 800°C at times, silver paste became brittle and lost its adhesive properties. The silver paste being annealed was another consideration. Temperature programmed desorption involves monitoring the desorption using a residual gas analyzer. This would have further complicated the spectrum as species desorbed from the paste were monitored with those being desorbed from the diamond films. After UPS and XPS measurements were taken, the samples were then analyzed by taking SEM and XRD measurements. Afterward, samples were often reintroduced into the UHV chamber for additional UPS or XPS. The repeated analysis of each sample was greatly simplified by the ability to easily mount and remove them using the specialized holders.

3.1.3 Grain Size Measurement

The powders were "micronized" through a filtering process that selects only specific grain sizes within some limit. To verify the manufacturer's specifications, SEM micrographs were taken from 1500 to 5000 times magnification depending on the average grain size. For these measurements a JEOL JMS-T300 scanning electron microscope was used. The purpose of the SEM was not only to measure the crystallite size, but also to observe film coverage. In order to measure the average crystallite size,

SEM micrographs typically contained a collection of 30-60 crystallites in various regions of the film to observe the consistency in size.

In order to determine the average grain size for a given film, the individual crystallites of a region were estimated according to the SEM scale. The distributions of sizes were then averaged. All of the films were in good agreement with the manufacturer's specifications. Shown in Figures 3.3-3.9 are SEM micrographs for the 3-5, 4-6, 5-10, 15, 30, 45 and 98 micron grain sizes. In the SEM images, sizes referred to are manufacturer's specifications and Table 3.1 of actual measured sizes follows.

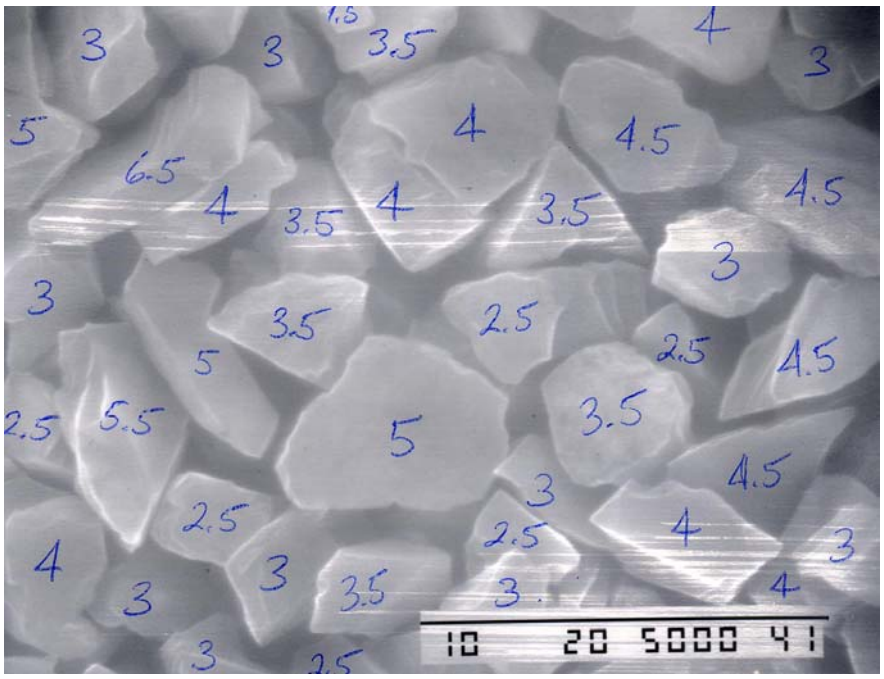

Fig 3.3 SEM of 3-5 micron Diamond

Fig. 3.4 SEM of 4-6 micron Diamond

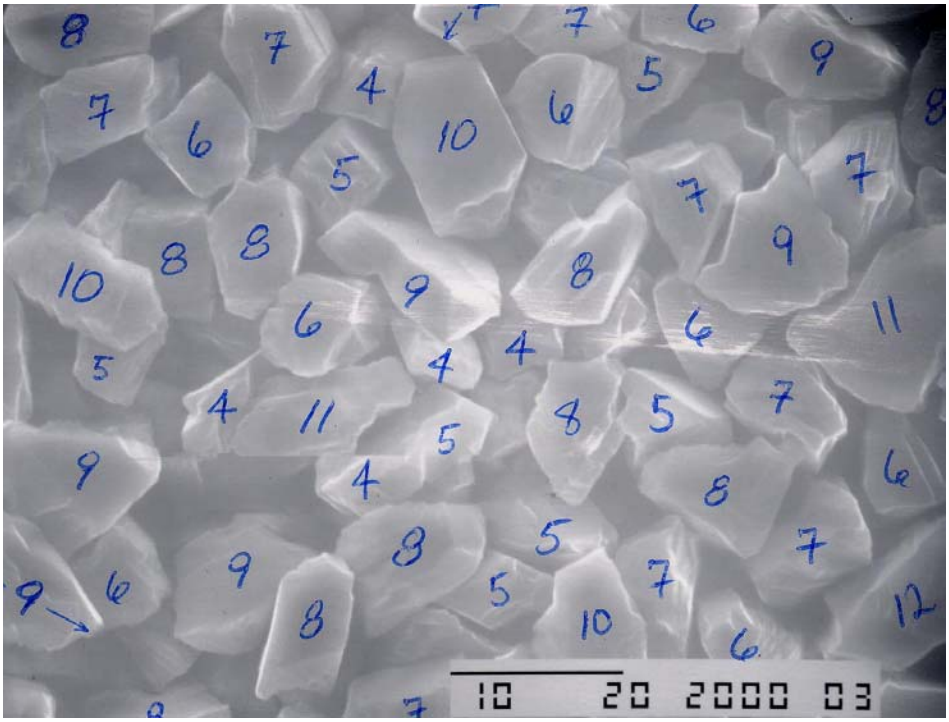

Fig. 3.5 SEM of 5-10 micron Diamond

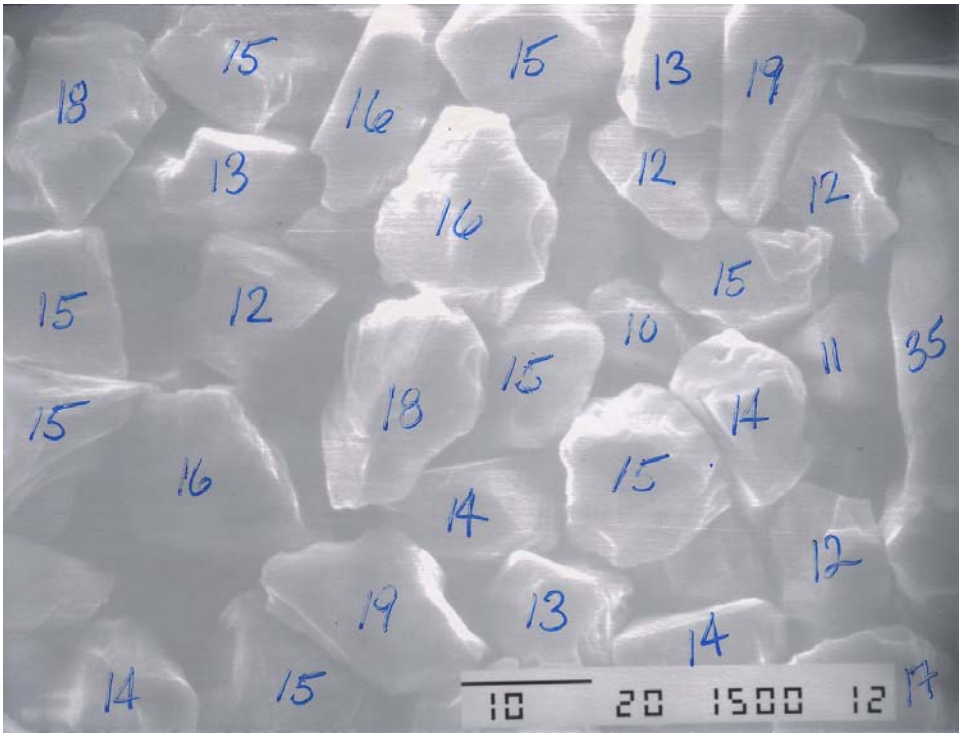

Fig. 3.6 SEM of 15 micron Diamond

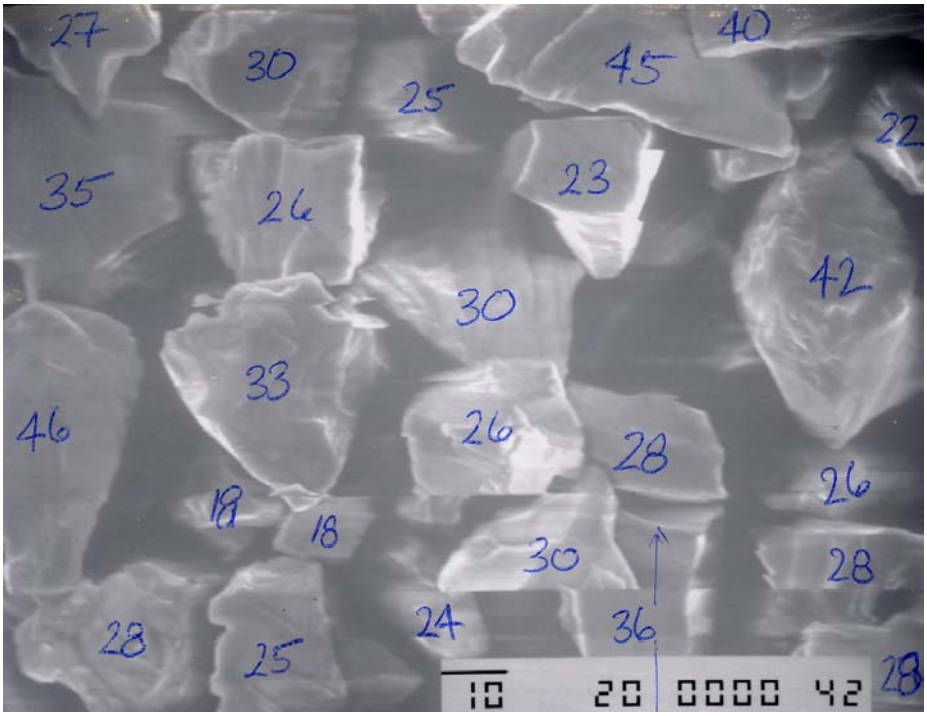

Fig. 3.7 SEM of 30 micron Diamond

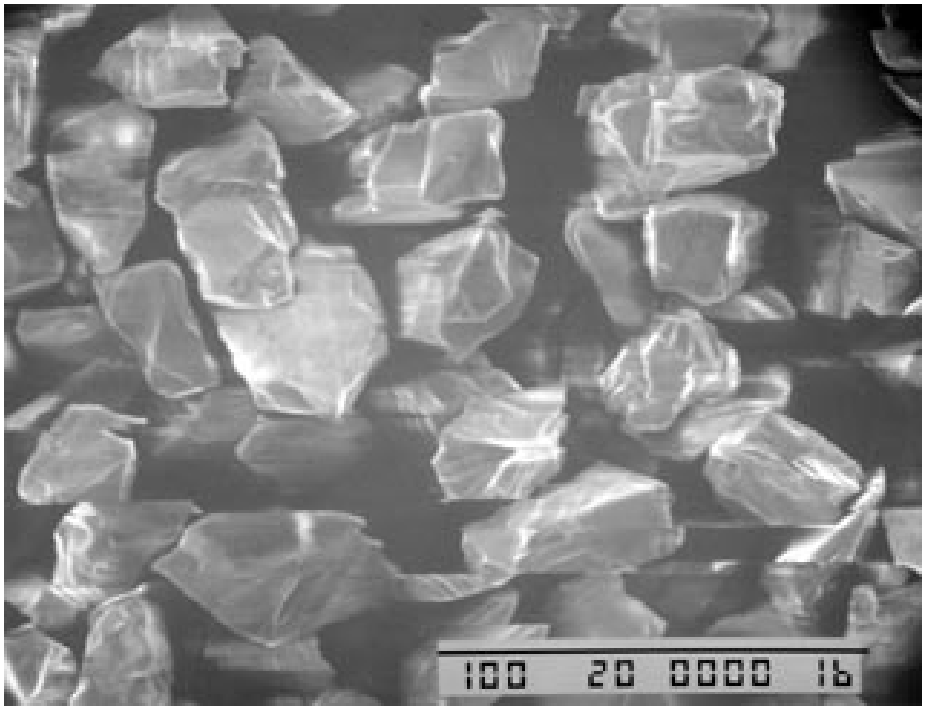

Fig. 3.8 SEM of 45 micron Diamond

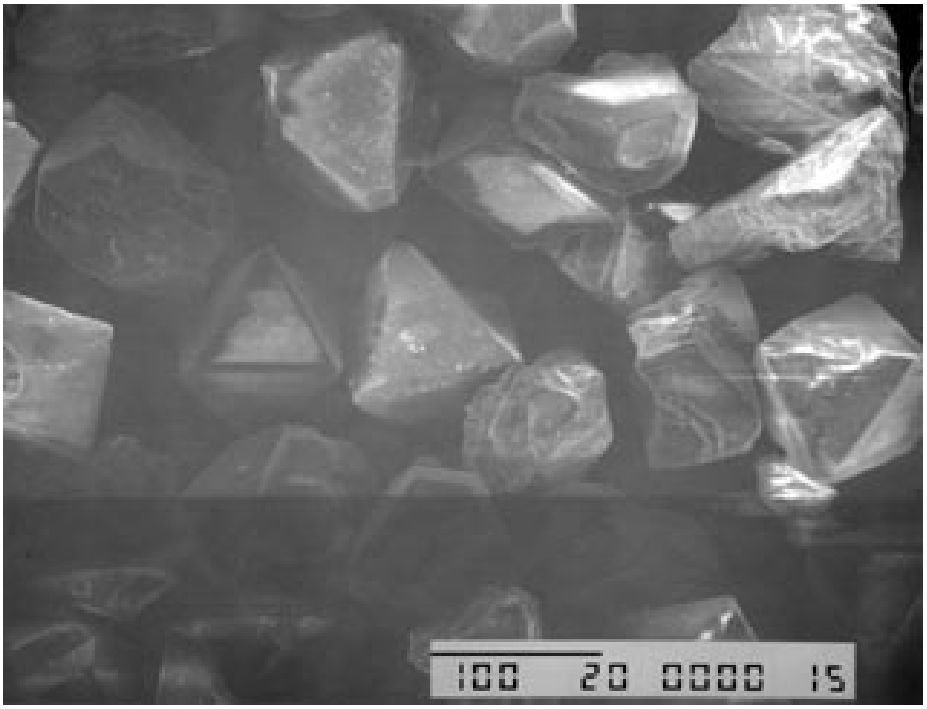

Fig. 3.9 SEM of 98 micron Diamond

Average Size (microns)	Labeled Size (microns)
0.32	¼
1.1	½
3.6	3-5
3.9	3-6
4.8	4-6
7.3	5-10
7.8	9
9.6	8-12
10.4	8-16
12.4	15
15.3	15
26.7	25
29.3	30
40.5	45
108	98

Table 3.1 Average Grain Sizes

In addition to averaging the grains, a distribution was calculated for each sample. This was to ensure there was not a large deviation from the mean for each particular size. The standard deviation was calculated for each grain size by

$$\sigma = \sqrt{\frac{\sum_n w_n (x_n - y)^2}{N}} \qquad \textbf{(3.1)}$$

where the sum is on n over all grain sizes with w_n the being the number of crystallites of a given size x_n, y is the mean, and N the total number of grains measured. For example, the distribution of grain sizes for the 0.3 micron film is shown in Fig. 3.10.

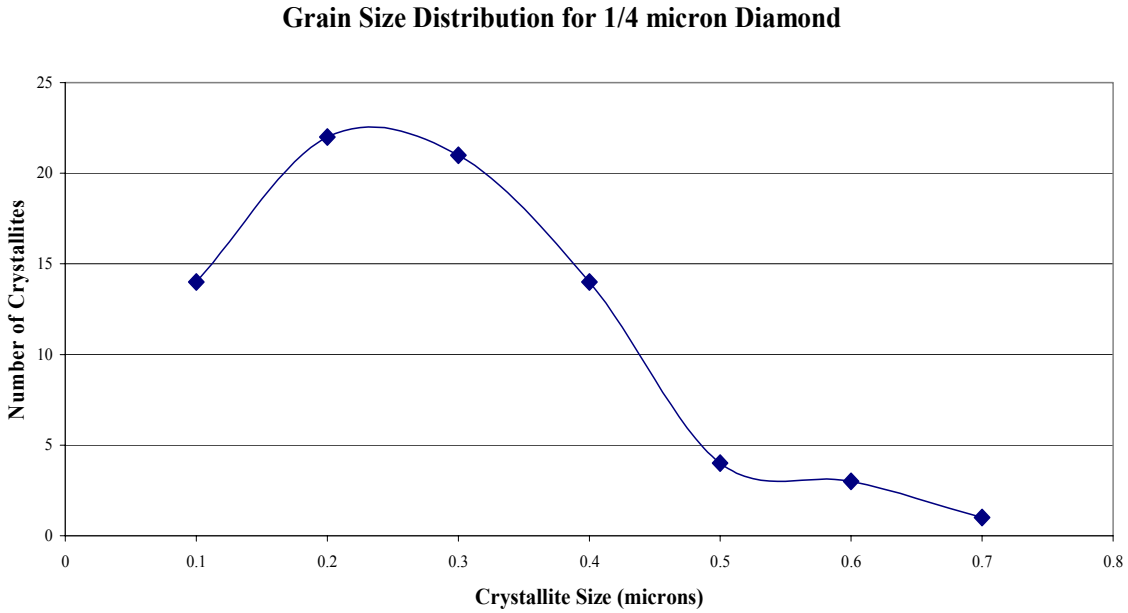

Fig. 3.10 Size Distribution for ¼ micron Diamond

The mean for this distribution is approximately 0.3 microns with a standard deviation of 0.13 microns. The standard deviation for the crystallite sizes was generally between 15 and 20 percent of the mean. Shown in Table 3.2 are the standard deviations calculated for each average grain size.

Average Grain Size (microns)	Standard Deviation (σ) (microns)
0.3	0.13
1.1	.34
3.6	0.88
3.9	0.99
4.8	0.86
7.8	1.96
9.6	1.84
10.4	1.61
12.4	2.02
15.3	1.86
26.7	2.99
29.6	5.02
40.5	5.74
108	8.41

Table 3.2 Standard Deviation of Grain Sizes

3.2 ULTRAVIOLET PHOTOELECTRON SPECTROSCOPY

3.2.1 Instrumentation and Experimental Procedure

The ultraviolet source used for the UPS measurements was a SPECS UVS 10/35 plasma discharge UV source using helium for the HeI line with an energy of 21.2 eV. This UV lamp is on a VG ESCA Lab II system and during UPS the pressure in the main chamber was 4×10^{-8} Torr. Radiation is emitted when the lamp strikes a plasma by a 1-1.5 kV DC discharge and operates at a current of 80-90 mA. Because an effective window material is not available for UV sources, there is some helium leakage into the main chamber despite the differential pumping. This explains the pressure of 4×10^{-8} Torr in a system which would otherwise have a base pressure of 8×10^{-10} Torr when the UV source is not in use.

The emission width of diamond has been measured to be from 19-24 eV [2-4], which makes the helium plasma resonance lamp an effective source for observing the full width of the valence band. The diamond spectra have a characteristic double-bump structure with a strong onset at ≈5.5 eV indicative of the band gap. In order to observe the NEA of the diamond films, it was necessary to bias the samples by –6V. This negative bias provides the additional energy needed to eject the low energy electrons from the conduction band into the vacuum. An unbiased sample shows only one predominant structure in the spectra. However a negative bias on the sample allows for the NEA peak (lower kinetic energy) to be observed in addition to the photoemission from the valence band.

The samples were irradiated with a beam spot size of approximately 5mm in diameter, and the UPS spectra were typically taken in step sizes of 0.05 eV for 3-6 scans. A spectrometer pass energy of 5 eV was used giving a resolution of 0.2 eV for all samples. The slit width of the spectrometer was 3mm with an acceptance angle of 6°at the aperture to the analyzer. Photoemission of the samples was comparable, however the NEA peak was more pronounced in thicker films. Although the peak intensities vary with film thickness, the positions of the peaks for a particular grain size remain constant for each.

3.2.2 UPS Results and Discussion

From the UPS spectra, it is possible to calculate parameters of interest, such as work function, NEA, and Fermi level of the diamond. The kinetic energy threshold measures the Fermi level offset of the diamond ξ above the valence band maximum ($\xi = E_F - VBM$). From this, the emission width W is measured from the NEA peak maximum to the kinetic energy onset. The emission width then allows the electron affinity χ to be calculated

$$\chi = h\nu - E_G - W \tag{3.2}$$

The work function Φ is then given by

$$\Phi = \chi + E_G + \xi \tag{3.3}$$

The NEA peak varies in height as a function of coverage. As film thickness increases, the NEA peak height increases, due to the fact that there is more diamond present to participate in photoemission. Because work function is calculated from the electron affinity

(Eq. 3.3), a more negative electron affinity will lower the work function. The Fermi level varies among the samples between 2.2 and 2.6 eV above the valence band maximum.

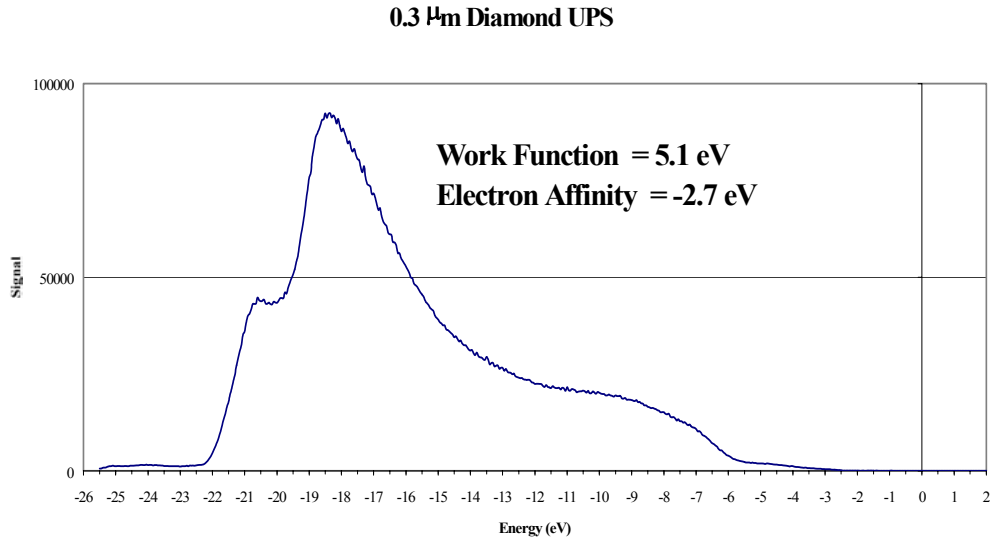

Figures 3.11 through 3.25 show the UPS spectra for increasing average grain sizes with work function and electron affinity.

Figure 3.11 UPS Spectrum of 0.3 micron Diamond

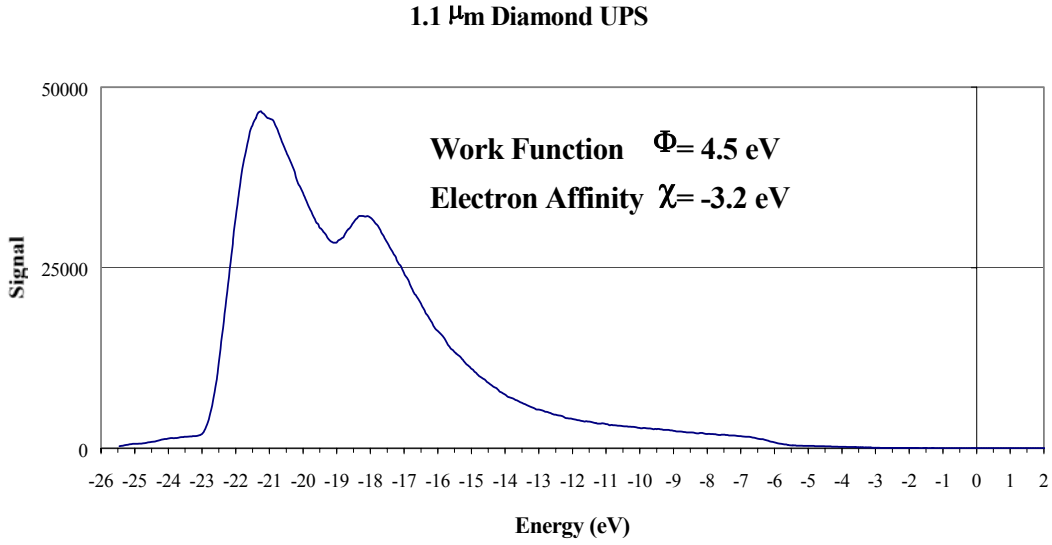

Figure 3.12 UPS Spectrum of 1.1 micron Diamond

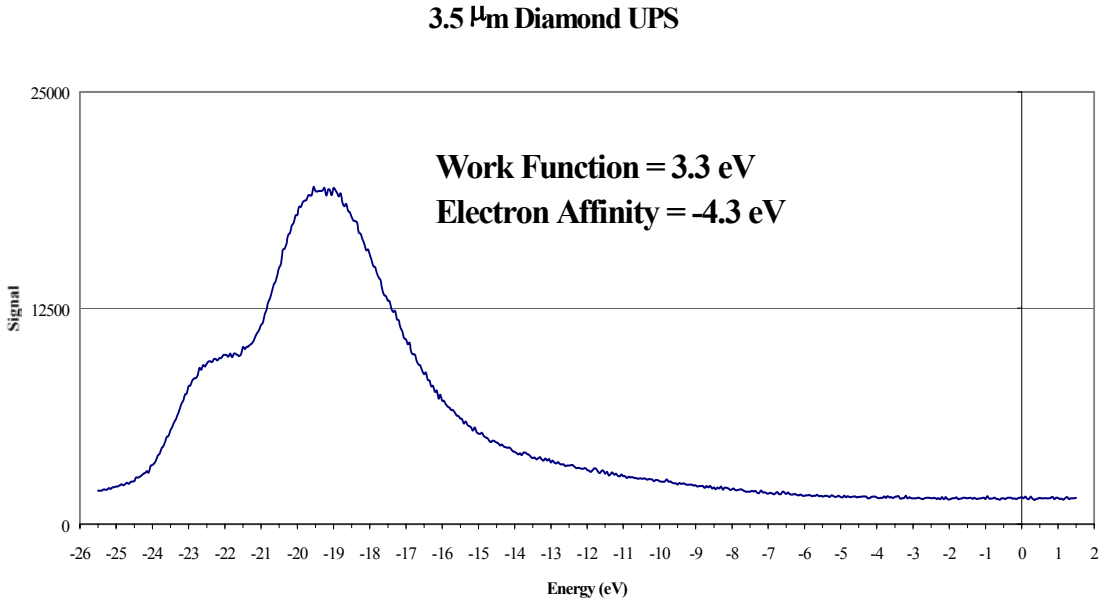

Fig. 3.13 UPS Spectrum of 3.5 micron Diamond

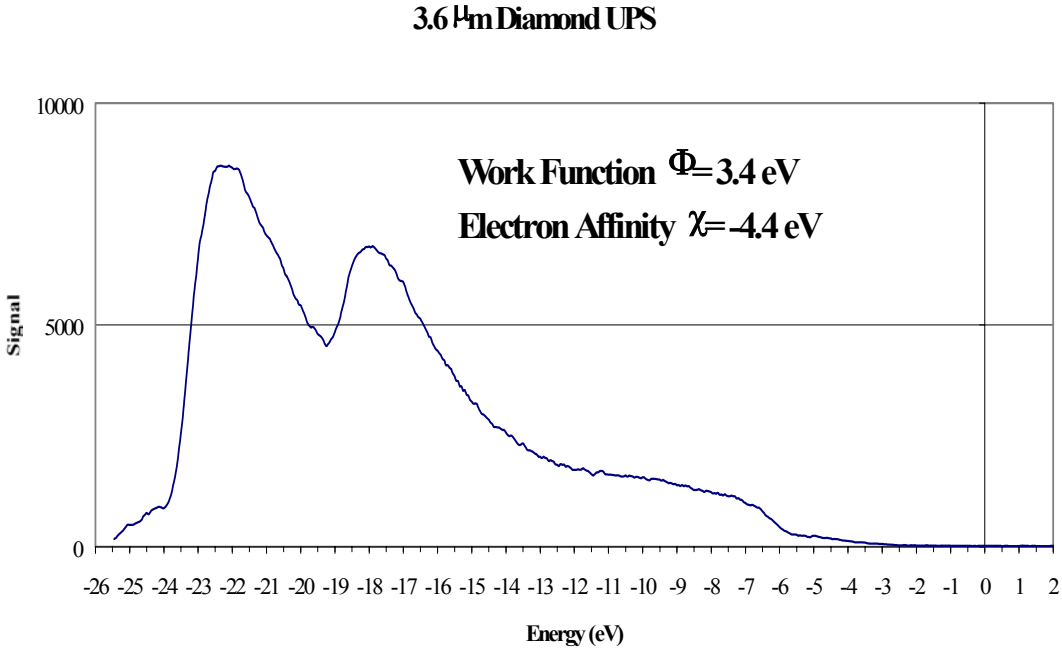

Fig. 3.14 UPS Spectrum of 3.6 micron Diamond

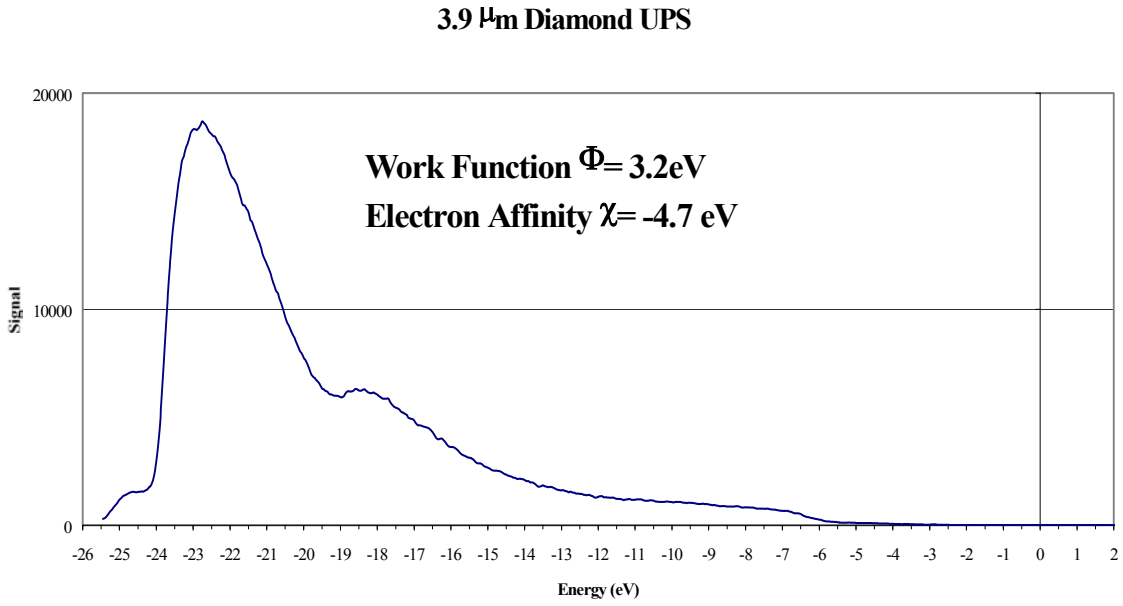

Fig. 3.15 UPS Spectrum of 3.9 micron Diamond

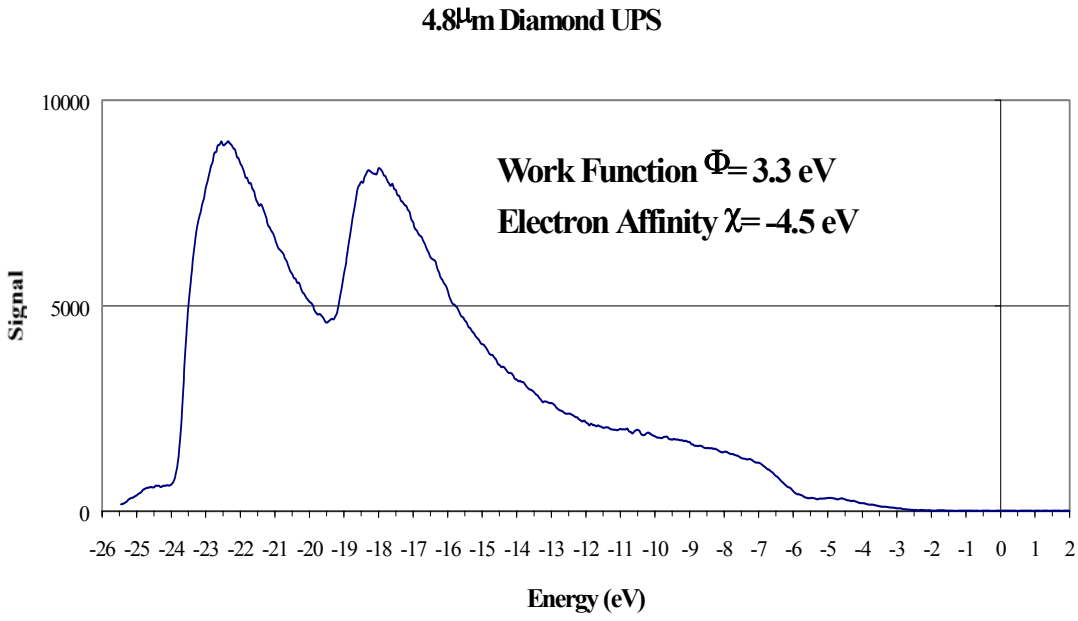

Fig. 3.16 UPS Spectrum of 4.8 micron Diamond

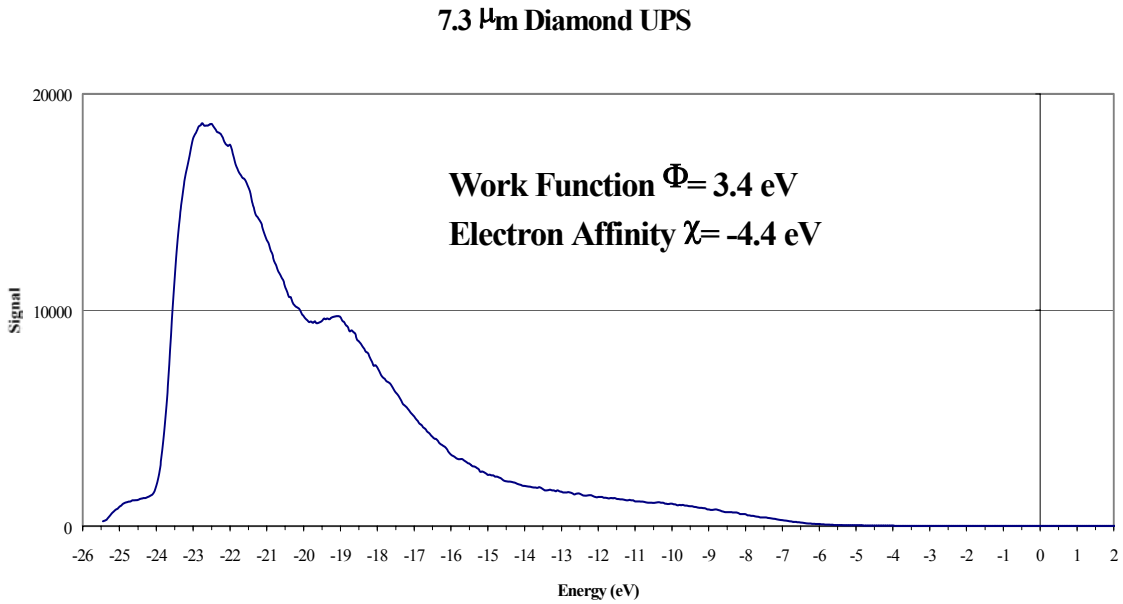

Fig. 3.17 UPS Spectrum of 7.3 micron Diamond

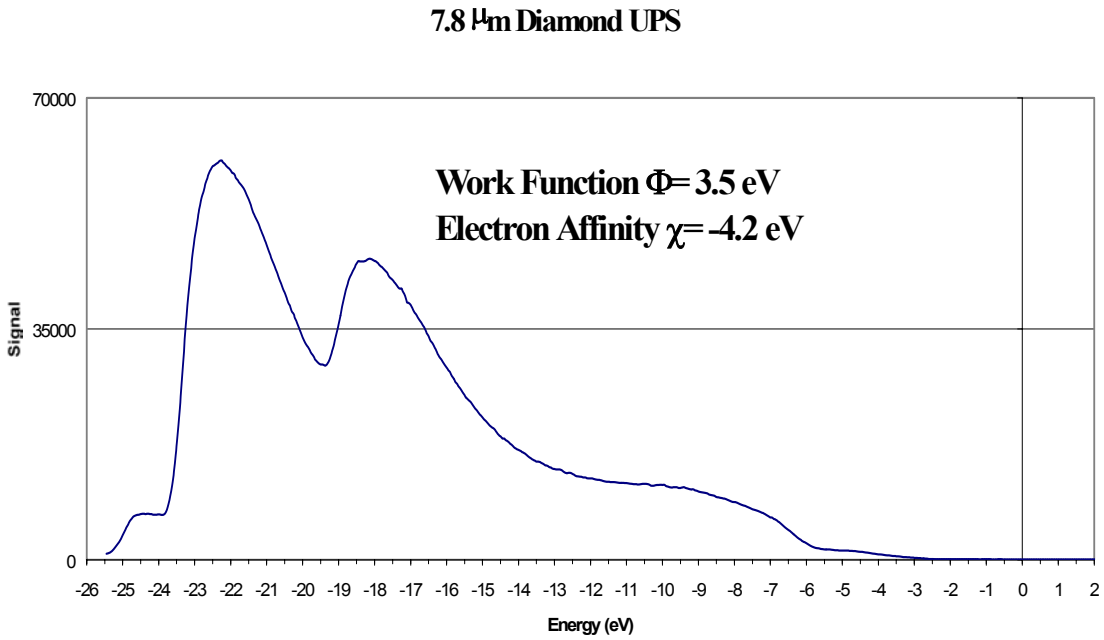

Fig 3.18 UPS Spectrum of 7.8 micron Diamond

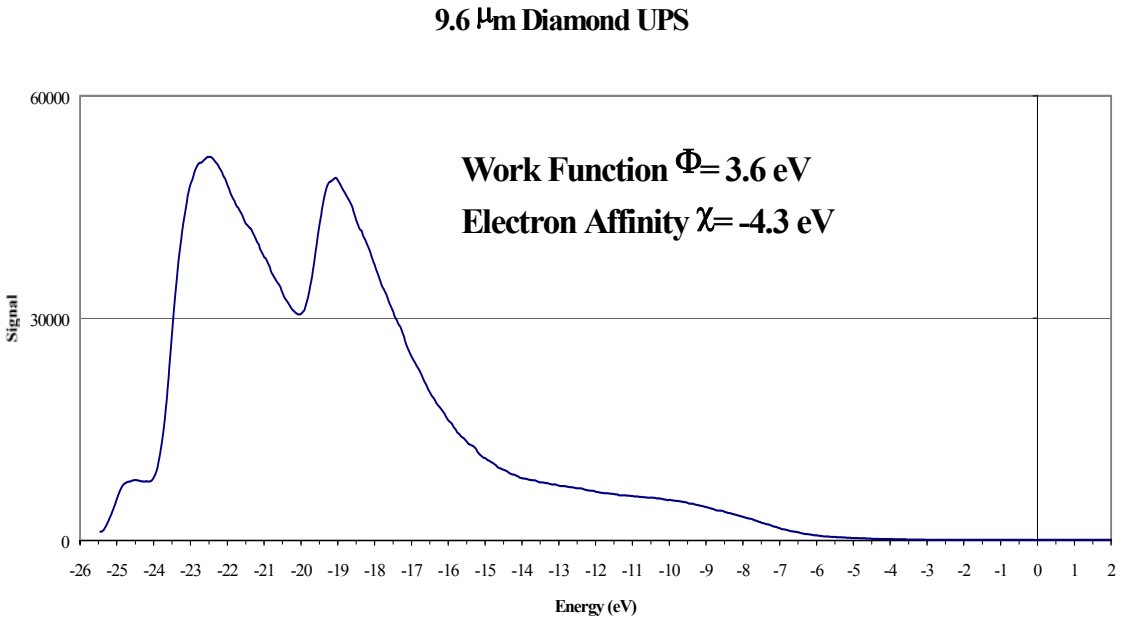

Fig. 3.19 UPS Spectrum of 9.6 micron Diamond

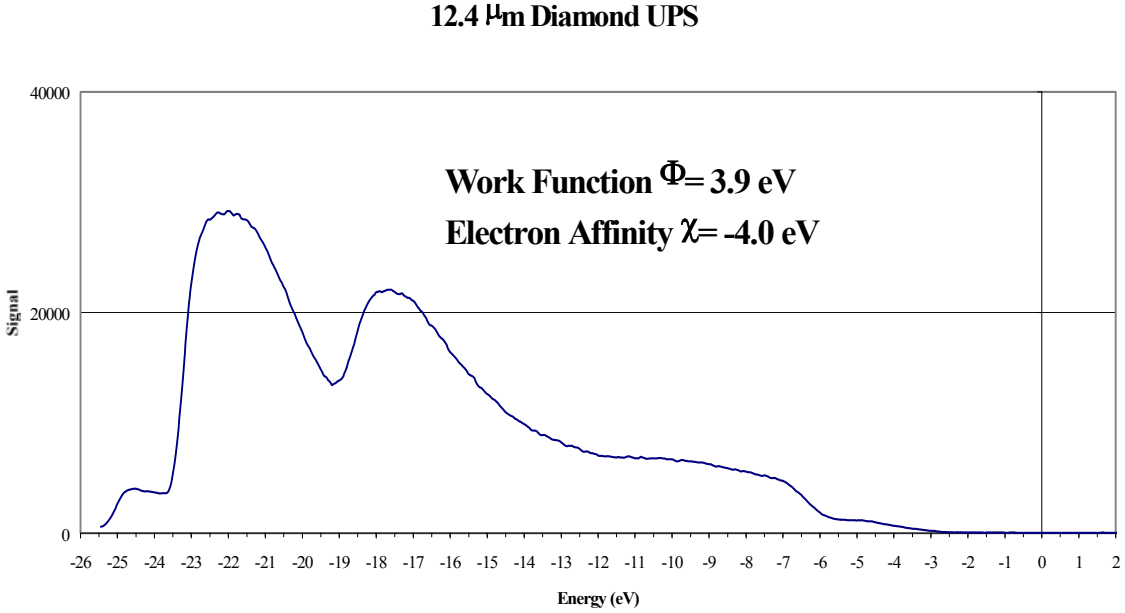

15.3 μm Diamond UPS

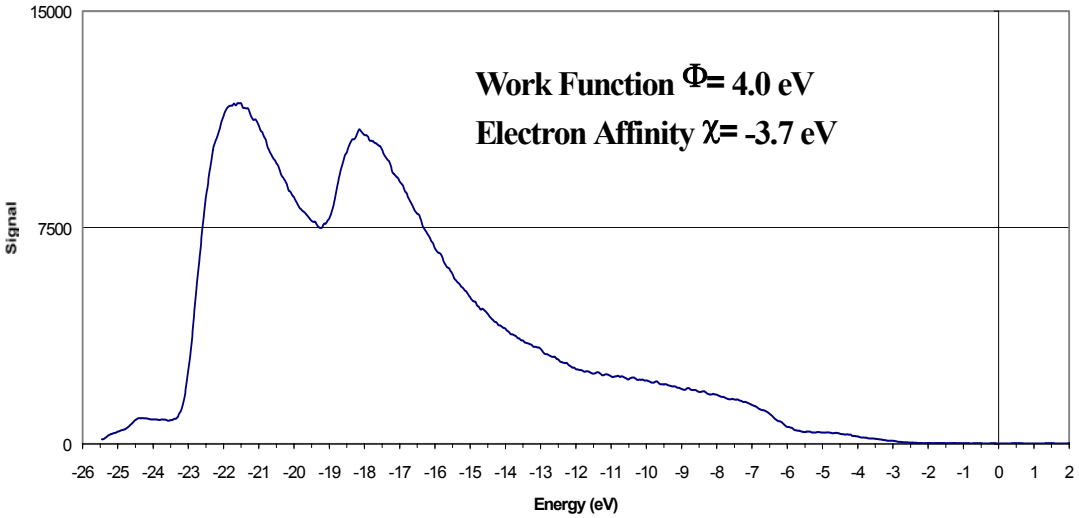

Fig 3.20 UPS Spectrum of 12.4 micron Diamond

Fig 3.21 UPS Spectrum of 15.3 micron Diamond

26.7 μm Diamond UPS

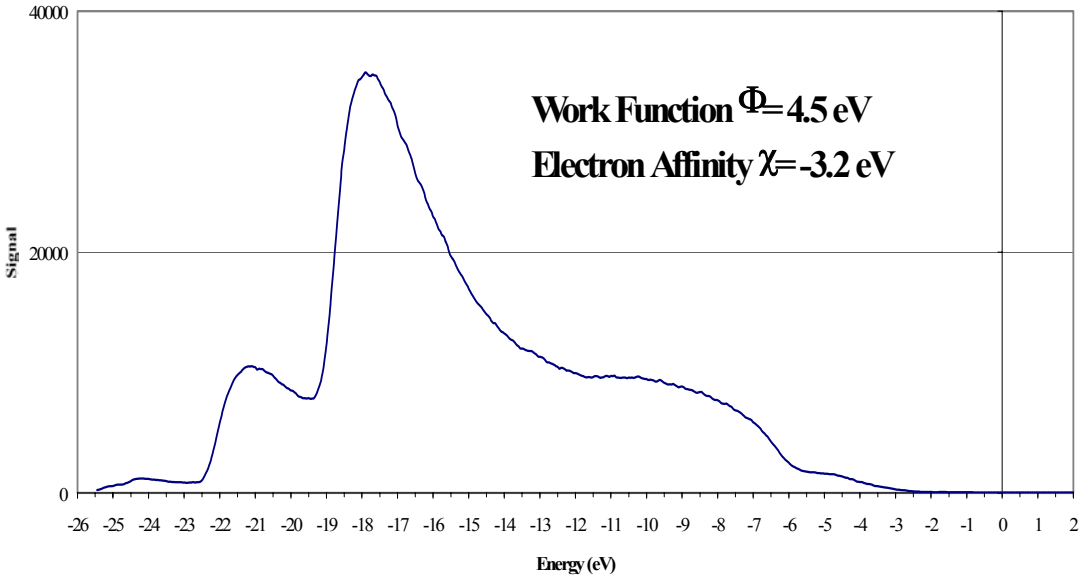

Fig. 3.22 UPS Spectrum of 26.7 micron Diamond

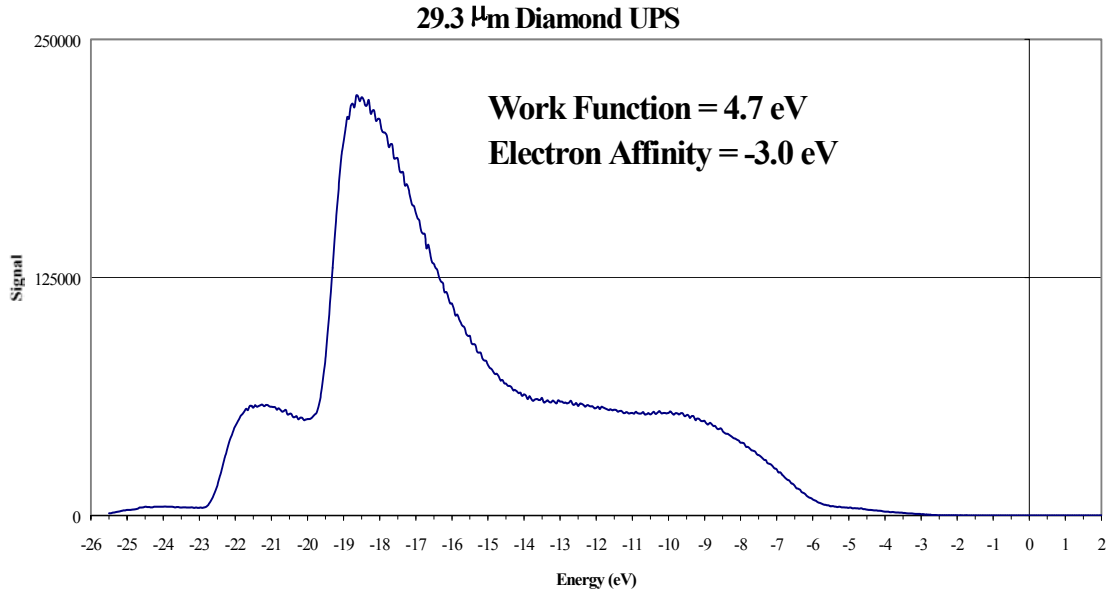

Fig 3.23 UPS Spectrum of 29.3 micron Diamond

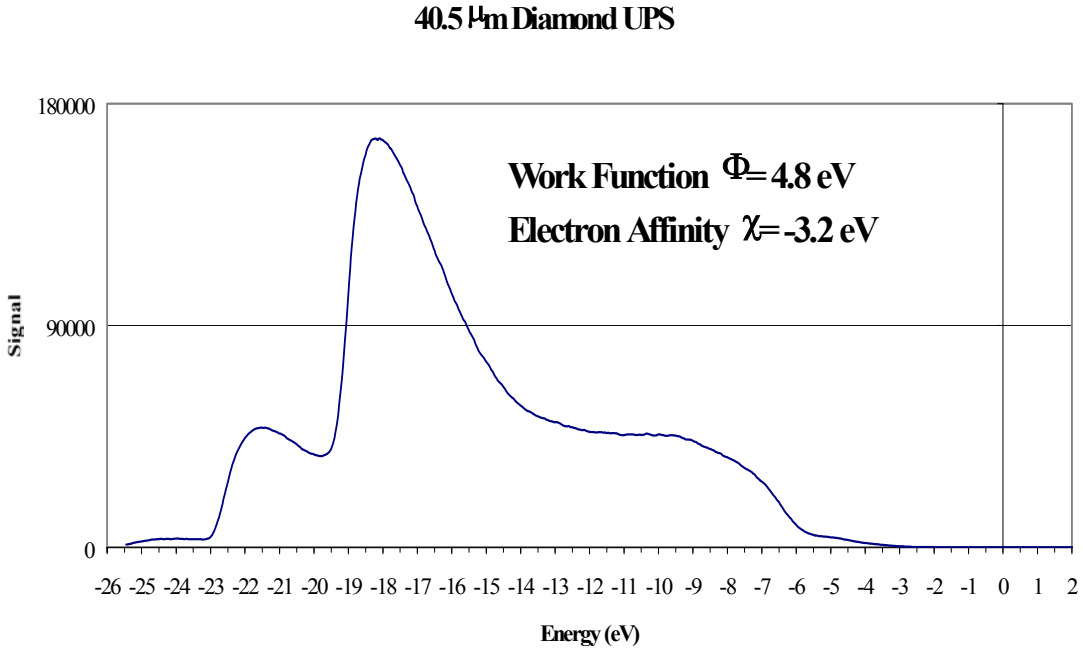

Fig 3.24 UPS Spectrum of 40.5 micron Diamond

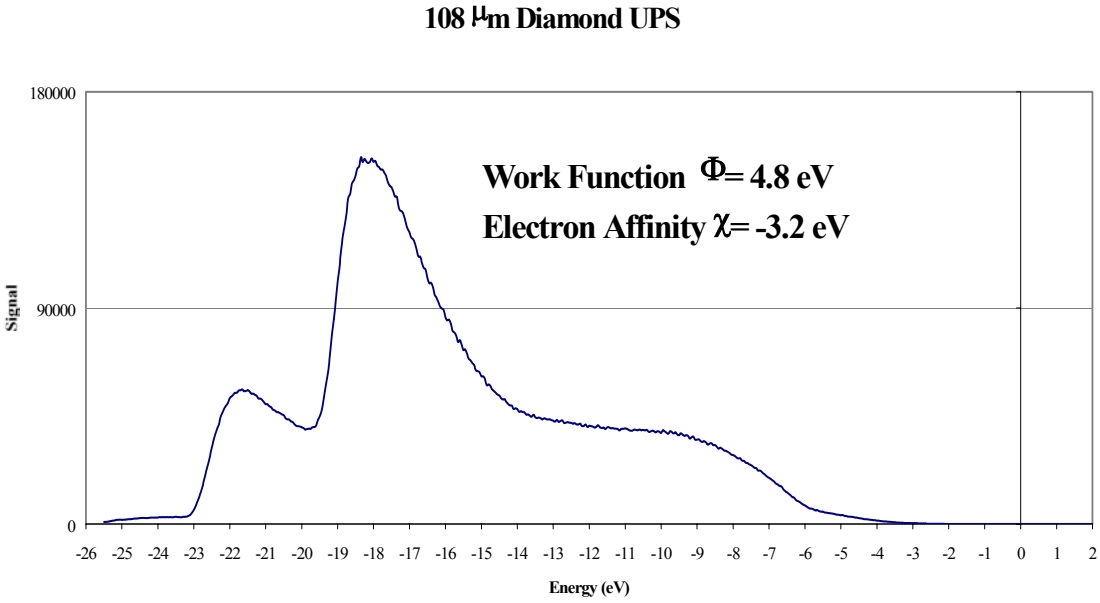

Fig 3.25 UPS Spectrum of 108 micron Diamond

All of the UPS spectra are plotted with respect to binding energy. The –6V bias and Fermi level of the molybdenum substrate are taken into account such that zero represents the Fermi level of the substrate. The kinetic energy onset allows the measurement of the diamond Fermi level offset ξ while a strong onset at 5.5 eV is indicative of the band gap. The NEA peak varies according to the film coverage such that thicker films yield a larger peak. This increase in signal is attributed to the presence of more diamond contributing to photoemission. Because film coverage is inversely proportional to average grain size, the NEA peak has a general decrease in signal as grain size increases.

The molybdenum substrates are highly susceptible to oxidation which forms an insulating barrier, and all of the Fermi level offsets were below the valence band

maximum due to this oxidation layer. The UPS parameters for all grain sizes measured are given in Table 3.3.

Grain Size (microns)	Work Function Φ (eV)	Electron Affinity χ (eV)	Fermi Offset ξ (eV)	Emission Width W (eV)
0.3	5.2	-2.7	2.4	18.4
1.1	4.5	-3.2	2.2	18.9
3.6	3.4	-4.4	2.3	20.1
3.9	3.2	-4.7	2.4	20.4
4.8	3.3	-4.5	2.3	20.2
7.3	3.4	-4.4	2.3	20.1
7.8	3.5	-4.2	2.2	19.9
9.6	3.6	-4.3	2.4	20.0
10.4	3.8	-4.3	2.6	20.0
12.4	3.9	-4.0	2.4	19.7
15.3	4.0	-3.7	2.2	19.4
26.7	4.5	-3.2	2.2	18.9
29.3	4.7	-3.0	2.2	18.7
40.5	4.8	-3.2	2.5	18.9
108	4.8	-3.2	2.5	18.9

Table 3.3 Diamond UPS Parameters

The smallest average grain size shows a work function near that of graphitic carbon [1] while a minimum work function of 3.2 eV is measured for the 3.9 micron average grain size. As the average crystallite size increases, the work function approaches that of natural single-crystal diamond at 4.8 eV [5]. There are two factors that affect the work function of these films: the varying emission width and the Fermi level offset below the valence band maximum. While the Fermi level offset is a function of the properties the diamond-molybdenum bond and oxides on the Mo surface, the emission width is a direct consequence of the valence band properties. Because the electron affinity is calculated from the emission width (Eq. 3.2) and from this the work function (Eq. 3.3), the electron affinity governs the work function of the diamond. A more negative electron affinity gives a lower work function. Shown in Fig. 3.26 is a plot of how the electron affinity varies as a function of average grain size.

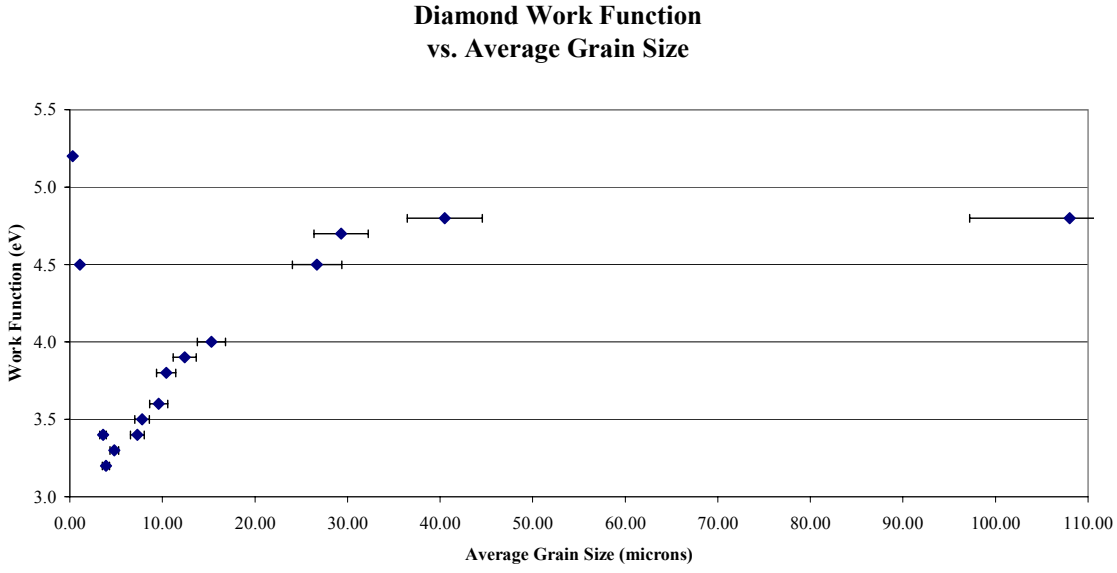

Fig. 3.26 Electron Affinity vs. Average Grain Size

From Table 3.1 it can be seen that as the electron affinity becomes more negative, the work function decreases, with the lowest electron affinity of -4.7 eV corresponding to the lowest work function of 3.2 eV for the 3.9 micron grain size. Other work has also shown large negative values (-4.20 eV) for the NEA [6]. In contrast, at the smallest average grain size of 0.3 μm, the smallest electron affinity of -2.7 eV corresponds to the highest work function measured of 5.2 eV.

Shown in Figure 3.27 is a plot of work function with respect to average grain size.

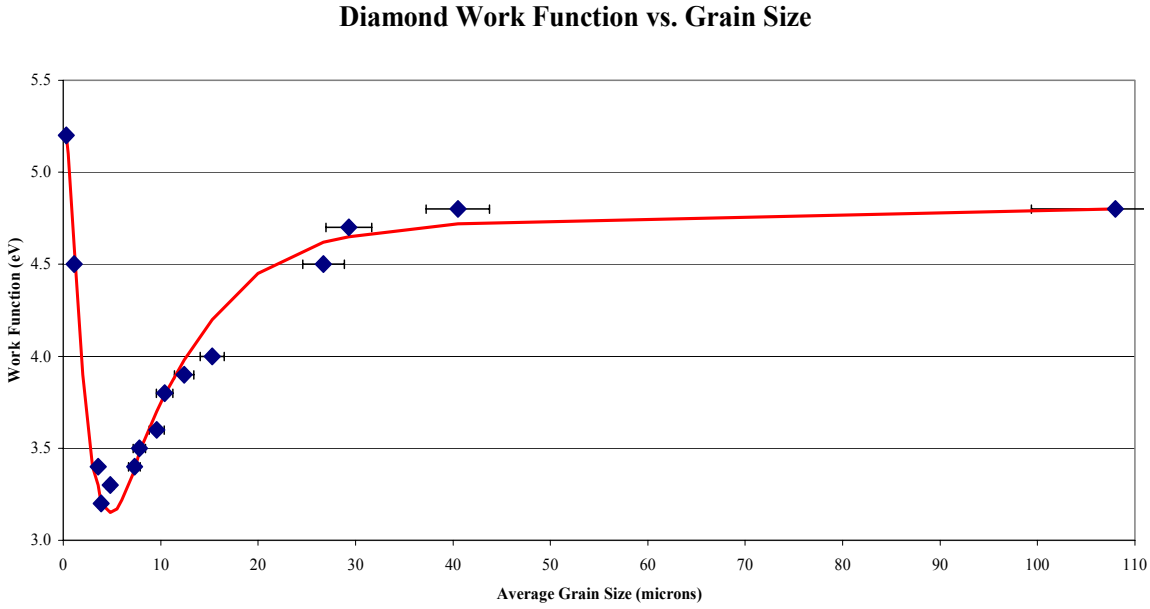

Figure 3.27 Work Function vs. Average Grain Size

Figures 3.26 and 3.27 show the same basic structure as the negative electron affinity controls the work function of the diamond surface. The Fermi offset varies slightly among the samples, depending upon interactions with the substrate and does not follow a general trend as does the electron affinity. The electron affinity which is a direct

consequence of the valence band emission width can be attributed to properties of the diamond crystallites as average grain size varies.

3.2.3 Effects of Annealing on Band Structure

In addition to finding a correlation between work function and average grain size, samples were annealed to observe changes in the electronic band structure. It has been reported that removal of chemisorbed hydrogen on the (111) diamond surface raises the work function by decreasing the electron affinity [7-11]. Thermal desorption spectra may be found in Sec 3.4 detailing the annealing procedures monitoring desorbed species.

The average grain size giving the lowest work function was 3.9 micron with $\Phi = 3.2$ eV. After annealing, the electron affinity changed from -4.7 eV to -3.3 eV. The UPS spectra before and after heating are shown in Fig. 3.28.

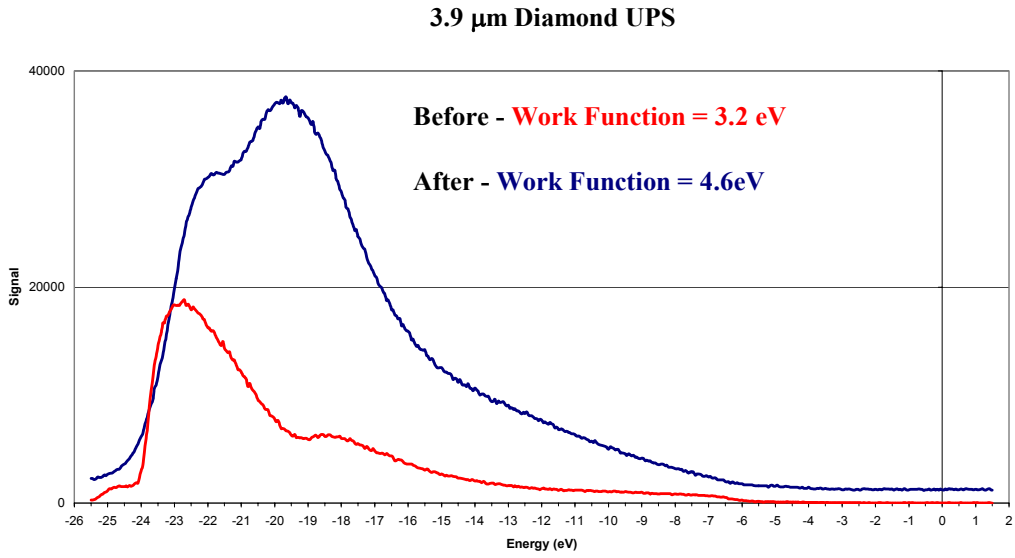

Fig. 3.28 UPS Spectra of 3.9 micron Annealed Diamond

The curve in blue shows the photoemission signal after heating. The NEA peak reduces in size as well as shifting by 1.4 eV. The Fermi level offset ξ remained constant before and after annealing.

The next larger grain size to be annealed was the 3.9 micron diamond which was also in the region of lowest work function at Φ = 3.4 eV. The UPS data for the sample before and after heating is shown in Fig. 3.29.

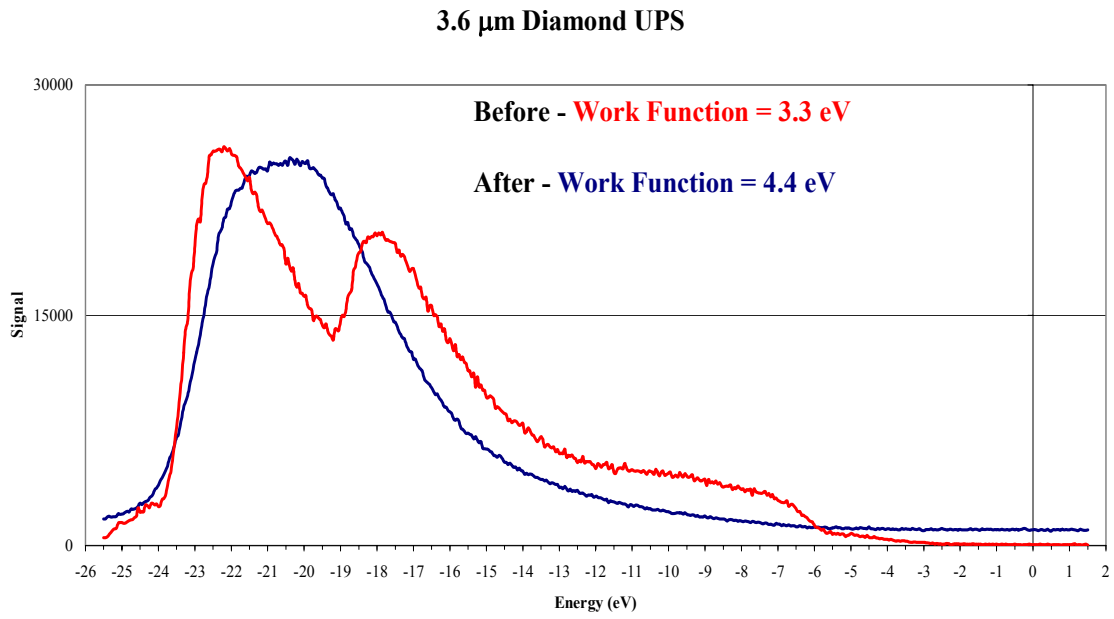

Fig. 3.29 UPS of 3.6 micron Annealed Diamond

Here, the NEA peak is shifted to lower binding energy (i.e. reducing the emission width and thus raising the work function). The change in emission width is due only to the NEA peak shifting, as opposed to the Fermi level shifting. The electron affinity before heating was -4.4 eV and changed to 3.3 eV after heating. This resulted in a work function that increased from 3.4 eV to 4.4 eV upon removal of the surface hydrogen.

The 4.8 micron average grain size had a surface work function of 3.3 eV prior to annealing which put it near the two previous grain sizes annealed. These three grain sizes (3.6, 3.9, and 4.8 microns) in the region of lowest work function were selected in order to observe the most dramatic changes in work function. Shown in Fig. 3.30 are the UPS spectra for the 4.8 micron sample prior to and after annealing.

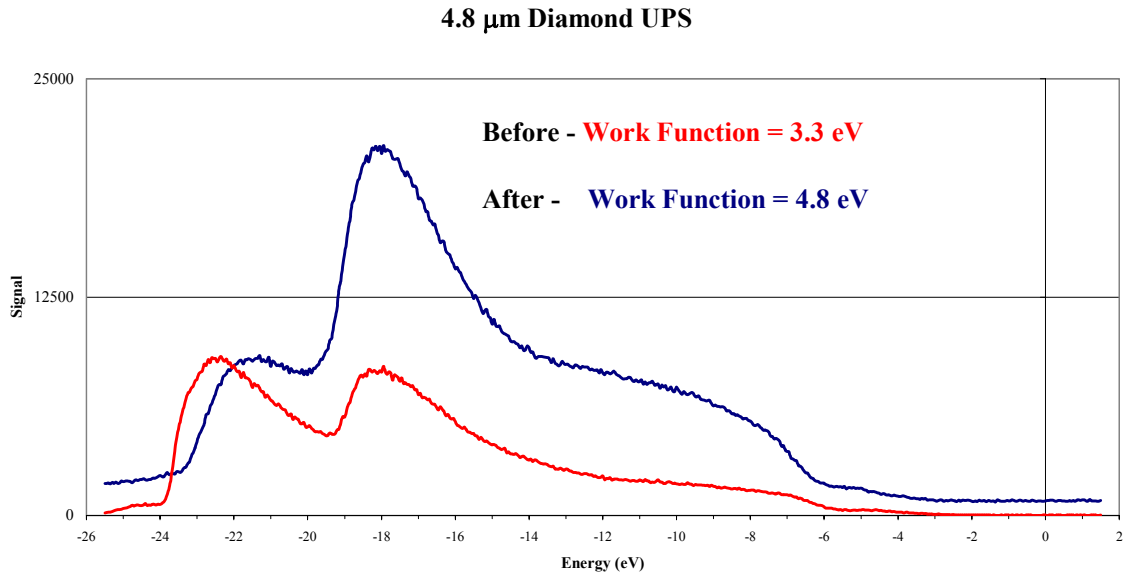

Fig. 3.30 UPS of 4.8 micron Annealed Diamond

The electron affinity before heating was -4.5 eV and afterward increased to -1.5 eV raising the work function from 3.3 eV to 4.8 eV. The 10.4 average grain size sample was also annealed with the UPS spectra before and after shown in Fig. 3.31.

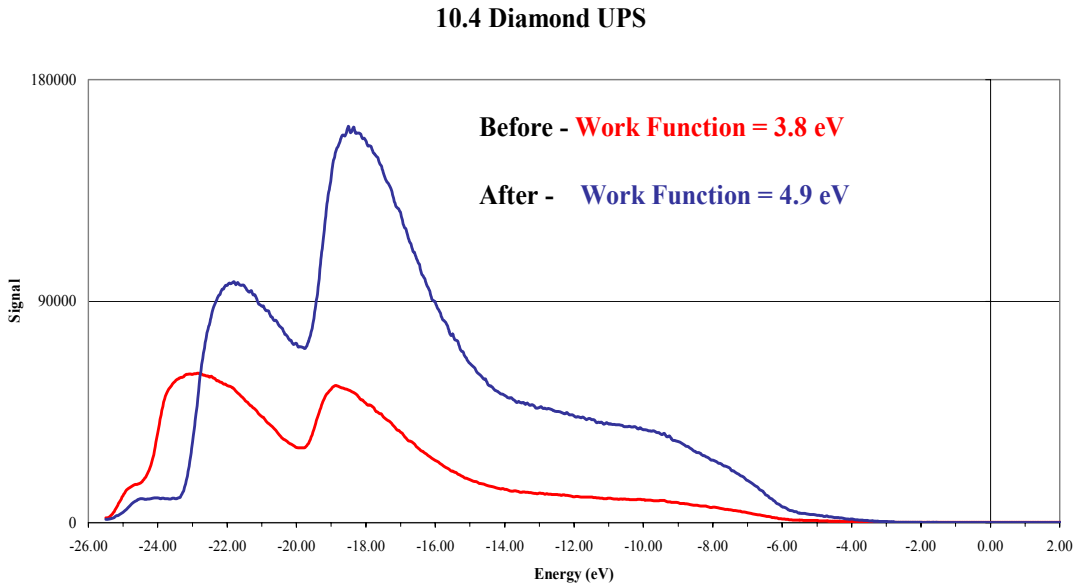

Fig. 3.31 UPS of 10.4 micron Annealed Diamond

Prior to annealing, the 10.4 micron sample had an electron affinity of -4.3 eV and after heating, this value changed to -1.1 eV. This change in electron affinity resulted in a work function which went from 3.8 eV before heating to 4.9 eV after heating.

Te most dramatic change occurred using the 1.1 micron grain size. While the work function was already 4.5 eV before annealing (only ½ eV below the work function of graphite), raising the sample temperature to 750°C for 45 minutes completely removed the NEA peak raising the work function to 5.0 eV as shown in Fig. 3.32.

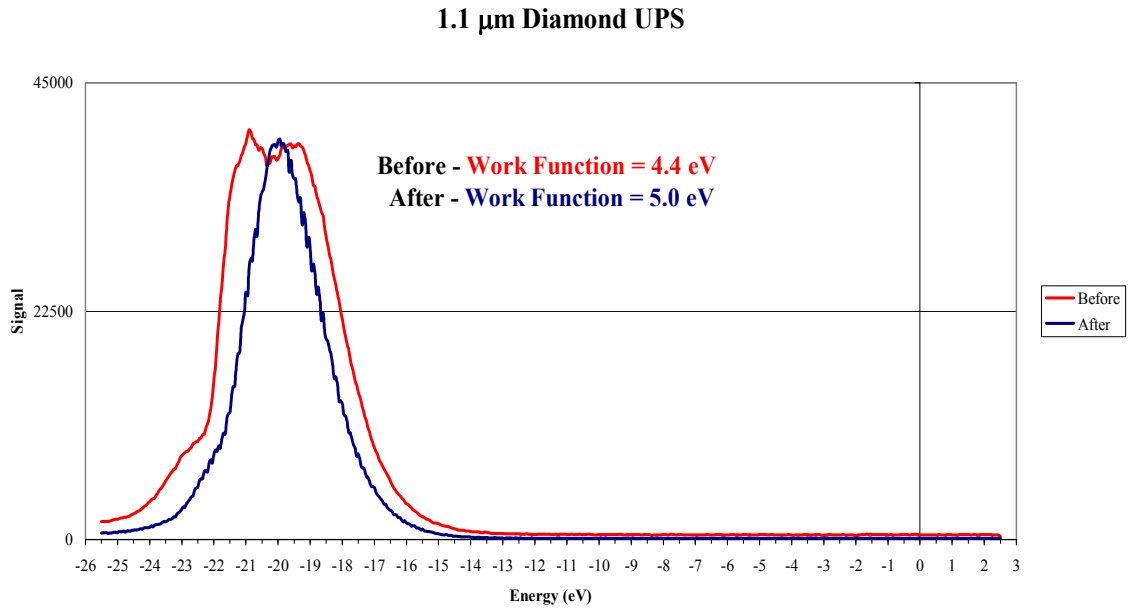

Fig. 3.32 UPS of 1.1 micron Annealed Diamond

Removing the hydrogen from the small area of defect sites allowed the work function to be dominated by the graphitic/amorphous carbon giving the work function of graphite. Characteristic in all of the spectra is the NEA peak shifting to lower binding energies which narrows the emission width of the valence band. As a result, this gives a greater (less negative) electron affinity which raises the work function in each case.

3.3 X-RAY PHOTOELECTRON SPECTROSCOPY

3.3.1 Elemental Composition

Survey scans were performed on a range of different grain sizes to determine the elemental composition of the surface. A “survey scan” involves a scan of the entire photon energy range up to 1486.6 eV in the case of an Al anode, and up to 1253.6 eV for a Mg anode. The XPS spectrum for the 15.3 micron grain size is shown in Fig. 3.33.

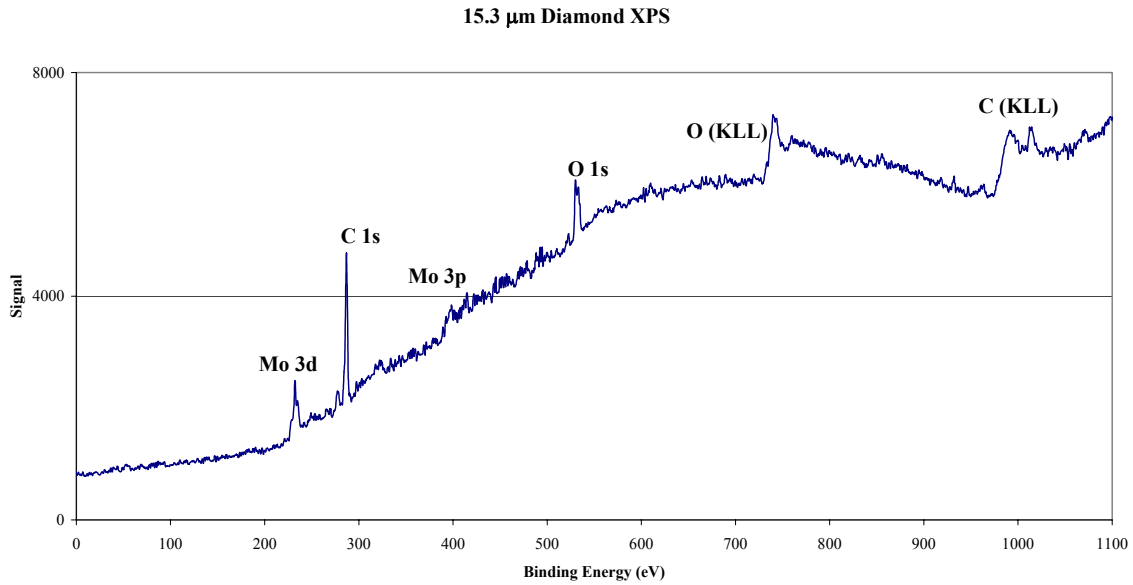

Fig. 3.33 XPS Survey Scan of 15.3 micron Diamond

The scan (using the Mg source of hν = 1253.6 eV) shows a large structure for the carbon 1s peak at 287 eV. There are four peaks shown for molybdenum: at 228 ($3d_{5/2}$), 231 ($3d_{3/2}$), 394 ($3p_{3/2}$), and 411 ($3p^{1}/_{2}$) eV. Because diamond does not readily oxidize, the oxygen 1s peak at 531 eV may be attributed to molybdenum oxides in the substrate. The spectrum also reflects Auger structures for both carbon and oxygen at higher binding energies.

The survey spectra for all average grain sizes reflect the molybdenum substrate, carbon and some oxidation states. For example, the survey scans for the 4.8 and 26.3 micron samples shown in Figures 3.34 and 3.35.

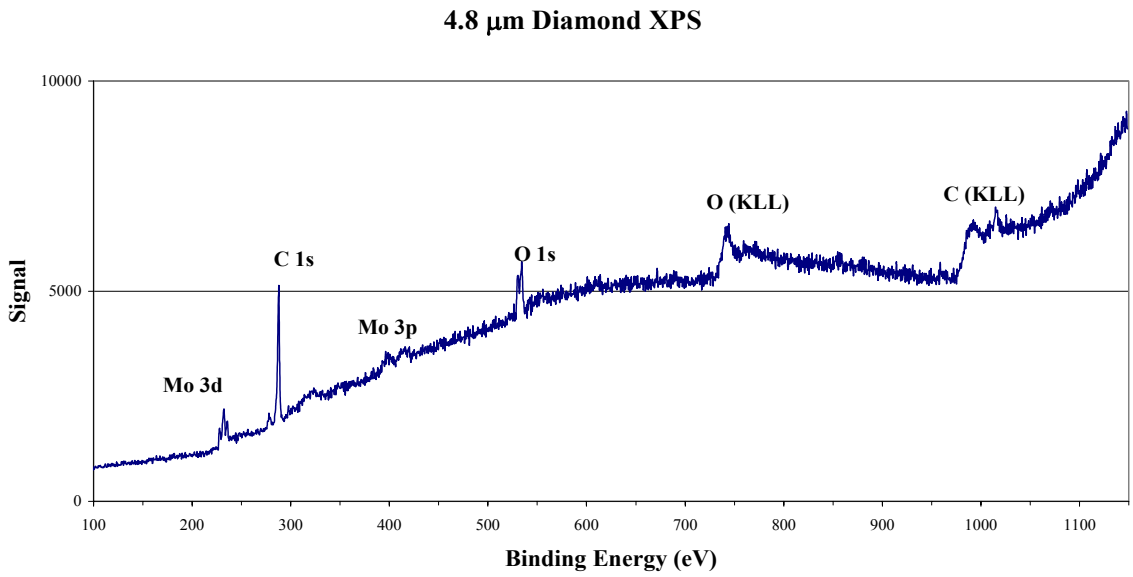

Fig. 3.34 XPS Survey Scan of 4.8 micron Diamond

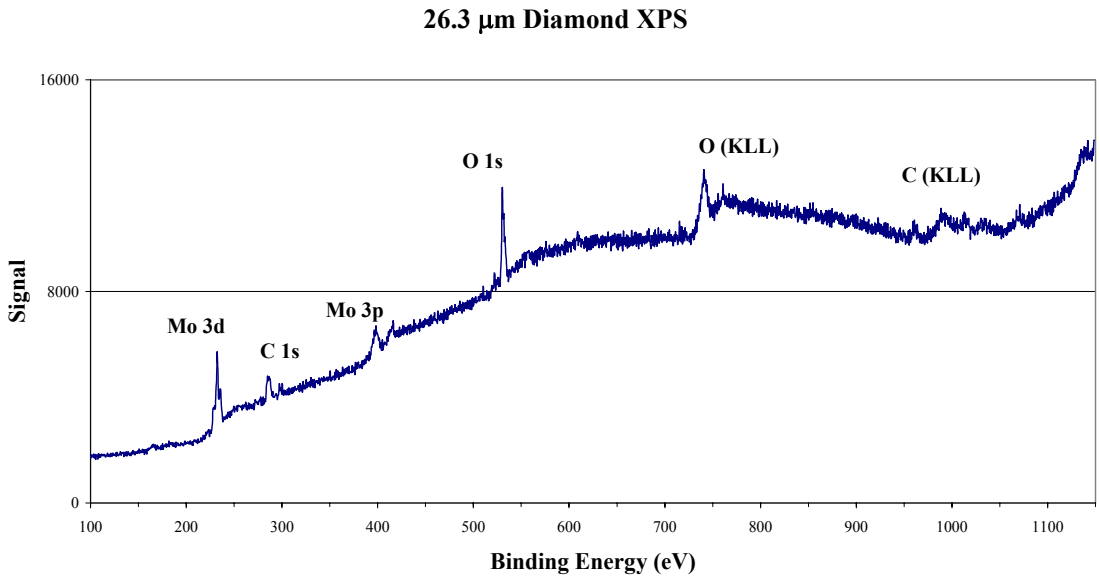

Fig. 3.35 XPS Survey Scan of 26.3 micron Diamond

3.3.2 Amorphous and Graphitic Carbon Fraction

While all of the samples reflect a double structure for the carbon 1s peak, the 0.3 and 1.1 micron average grain sizes showed significantly more graphite/amorphous carbon than the larger grain sizes. Amorphous carbon has a 1s binding energy of 284.6 eV, while the 1s binding energy for diamond peak has shown to be between 287-288 eV. The average grain sizes above 3 microns typically showed the carbon 1s peak at 287.6 eV, however this value was shifted to higher binding energies for the smallest grain sizes. The presence of graphite and/or amorphous carbon in the films may be attributed to the process used in making the diamond powders used for deposition. The C1s peak for the 0.3 micron sample is shown in Fig. 3.35.

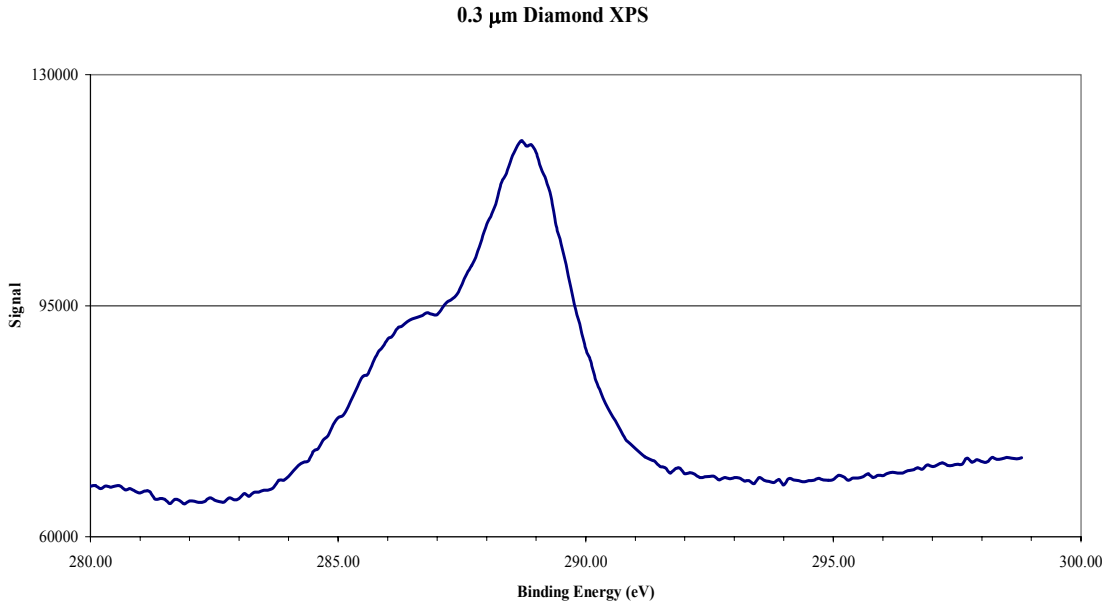

Fig. 3.36 XPS C1s peak of 0.3 micron Diamond

After fitting the two peaks, the sample shows to contain 29% amorphous carbon and 71% diamond. The diamond peak is at 288.8 eV while the graphitic peak is at 286.4 eV. The peak for the amorphous/graphitic carbon is at a slightly higher binding energy than the accepted value of 284.6 eV. This may suggest that the carbon species are not all graphitic carbon and are participating in bonding which raises the binding energy. Oxides may also play a role in raising the binding energy.

Shown in Fig. 3.37 are the fitted [13] 1s peaks. The upper curve shows the raw data in blue with the fitted curve. The lower curve shows the fitted peaks with the red diamond peak and blue graphite peak.

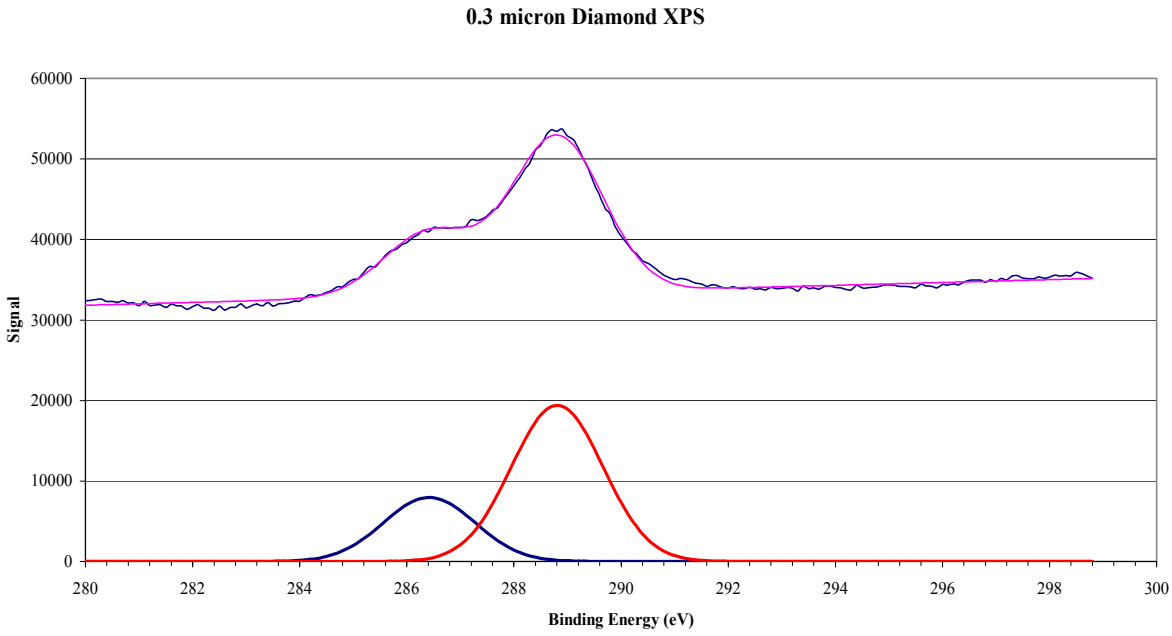

Fig. 3.37 Fitted XPS Spectra of 0.3 micron Diamond

Shown in Fig. 3.38 is the 1s spectrum for the 1.1 micron average grain size also exhibiting an increased sp^2 content as compared to all of the larger average grain sizes.

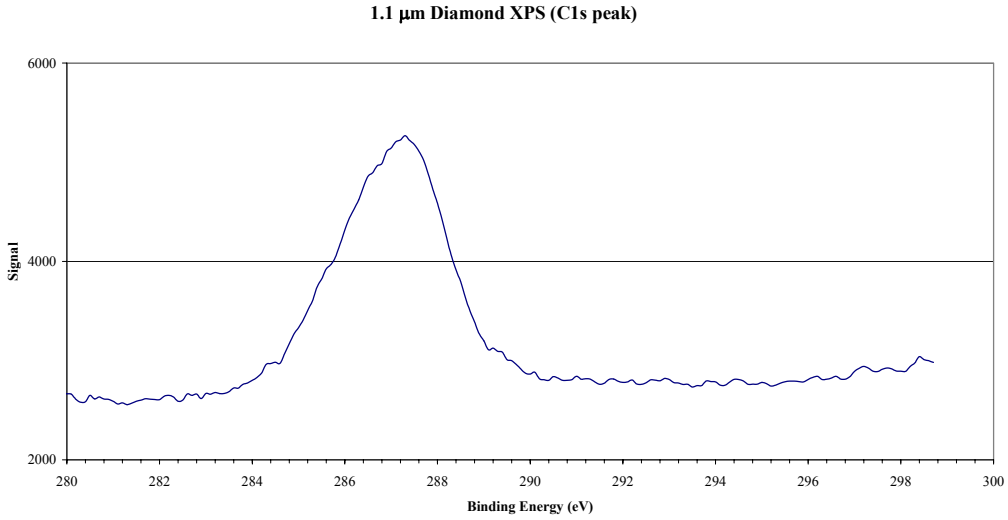

Fig 3.38 XPS C1s Peak of 1.1 micron Diamond

The 1.1 micron sample shows 28% amorphous carbon which is slightly less than the 0.3 micron sample. The fitted peaks for the 1.1 micron size are shown in Fig. 3.39.

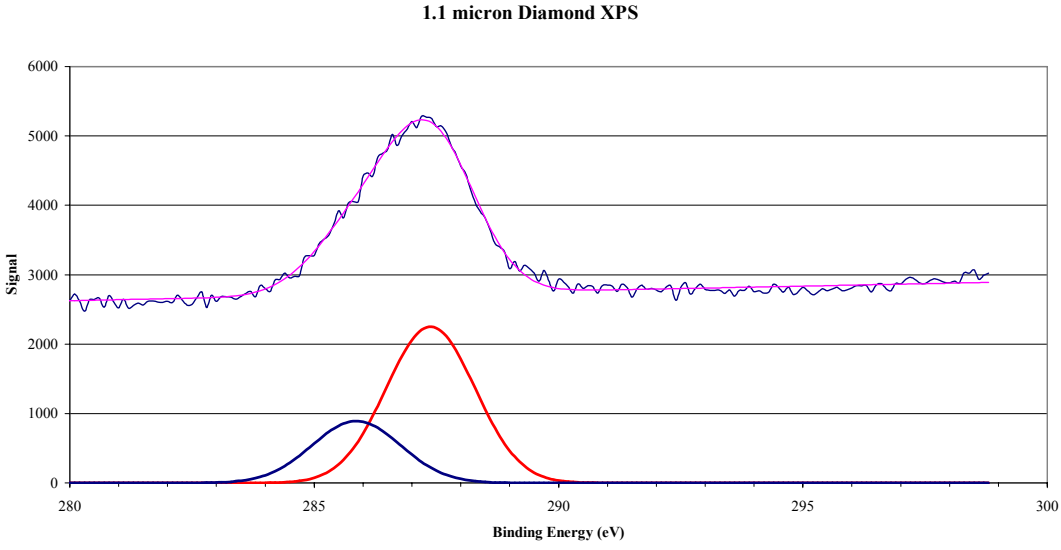

Fig. 3.39 Fitted XPS Spectra of 1.1 micron Diamond

The graphitic peak is shown in blue, the diamond peak in red with the raw data and fitted curve above. For this grain size the graphitic/amorphous peak is also shifted slightly to 285.8 eV. This again is attributed to numerous carbon species present and/or bonding which shifts the binding energy to higher values. The diamond peak is located at 287.3 eV, which is at approximately the same binding energy as in all other average grain sizes in this study.

Three larger sizes, the 4.8, 10.4 and 15.3 micron average grain sizes were fitted for the carbon 1s XPS peak. These also show the presence of sp^2 carbon but in smaller amounts. The sp^2 carbon content for the 4.8, 10.4, and 15.3 micron sizes are 16%, 15% and 20% respectively. Shown in Figures 3.40-3.42 are the fitted XPS C1s peaks for each of these three average grain sizes.

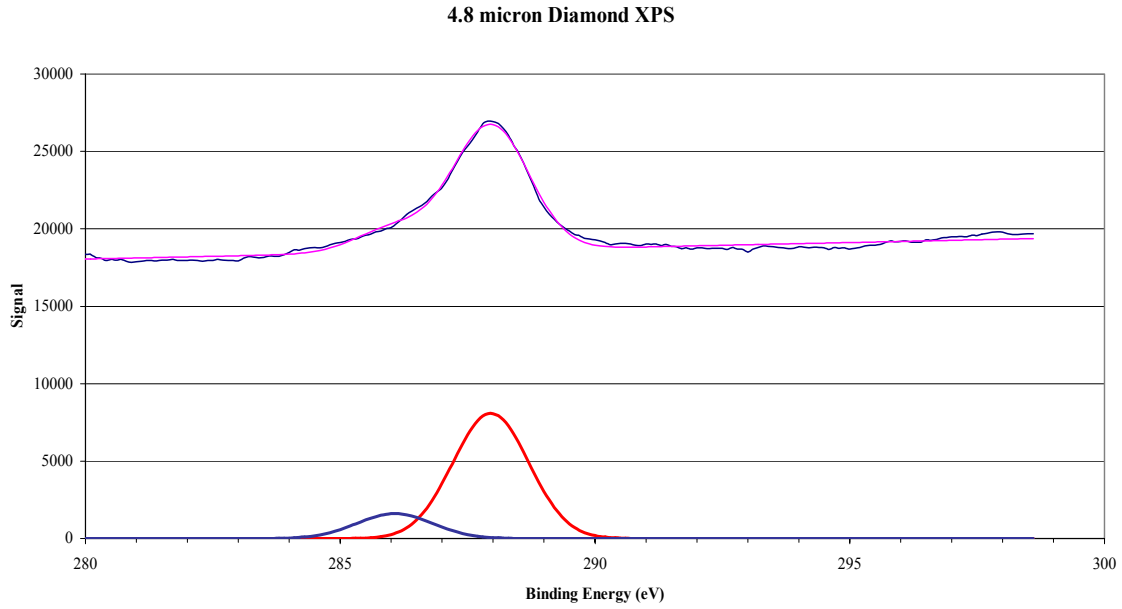

Fig. 3.40 XPS C1s peak of 4.8 micron Diamond

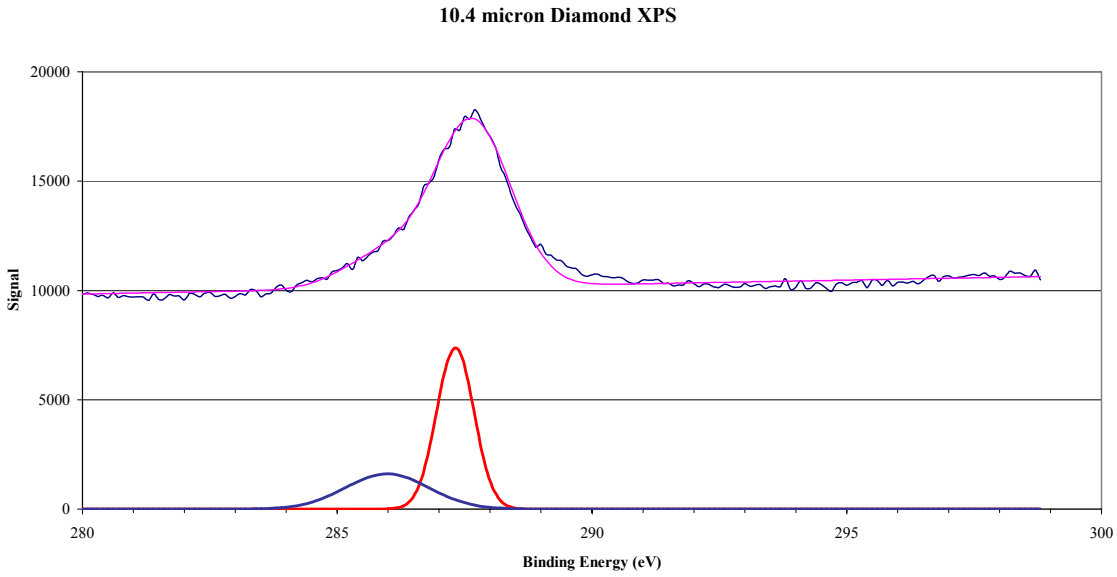

Fig. 3.41 XPS C 1s peak of 10.4 micron Diamond

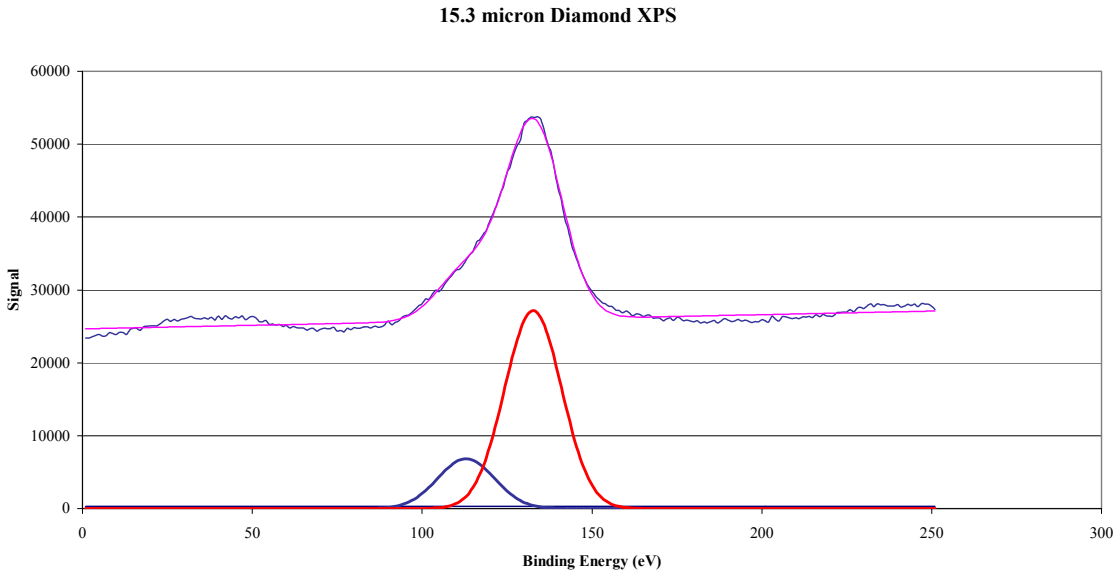

Fig. 3.42 XPS C1s peak of 15.3 micron Diamond

For comparison, carbon 1s peak for the largest grain size was shown to have a sp^2 fraction of only 13 percent as shown in Fig. 3.43.

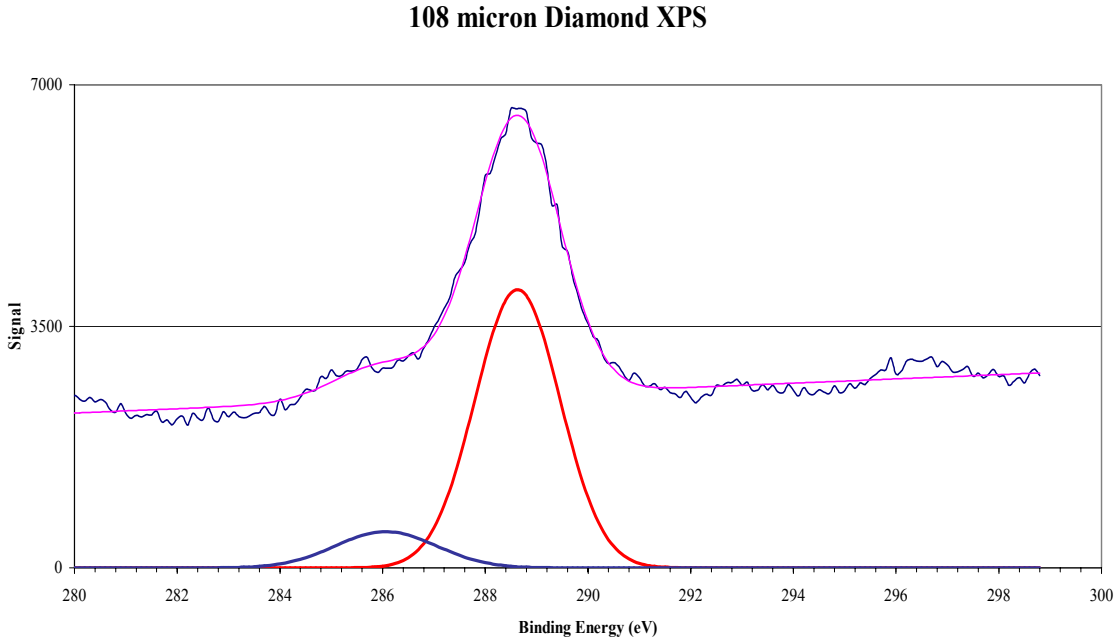

Fig. 3.43 XPS C1s peak of 108 micron Diamond

3.4 X-RAY DIFFRACTION MEASUREMENTS

The XRD measurements were all performed on films deposited onto molybdenum substrates as detailed in the section on sample preparation. A Siemens F-Series x-ray diffractometer was used for all measurements. The diffractometer utilizes only the Cu K_α x-ray by use of a monochromator. This results in radiation with a photon energy of 8.045 keV and a wavelength of 1.54 nm. The samples were secured in the apparatus by a small amount of clay keeping the samples fixed in a specialized holder for the diffractometer. The samples were then analyzed in steps of $2\theta = 0.05°$ from angles of

20-100° where θ is measured between the incident beam and the sample surface. Shown in Fig. 3.44 is the XRD spectrum for the 0.3 micron average grain size.

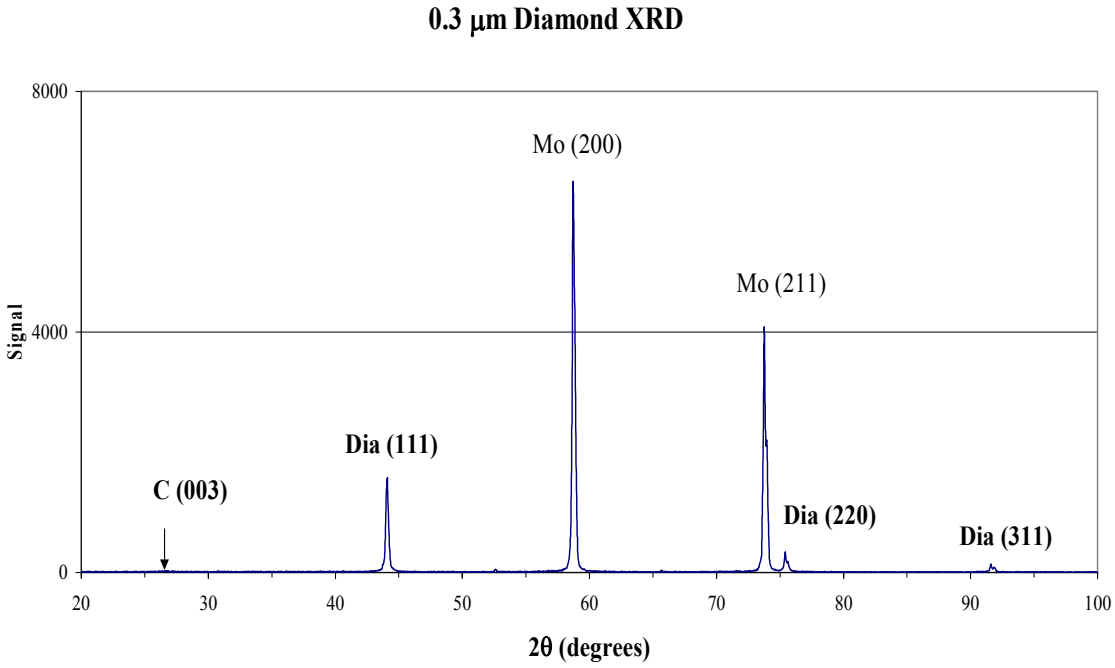

Figure 3.44 XRD Spectrum of 0.3 micron Diamond

The 0.3 micron average grain size shows a small amount of amorphous carbon which is also corroborated in the XPS data. The amorphous carbon peak shown in Fig. 3.43 is considerably smaller than the diamond peaks due to the difference in scattering cross sections of the two materials. The scattering cross section for graphite / amorphous carbon (sp^2) is approximately 38:1. Therefore the instrumentation is less sensitive to detecting amorphous carbon and graphite than diamond. Shown in Fig. 3.45 is an enlarged view of the amorphous carbon peak.

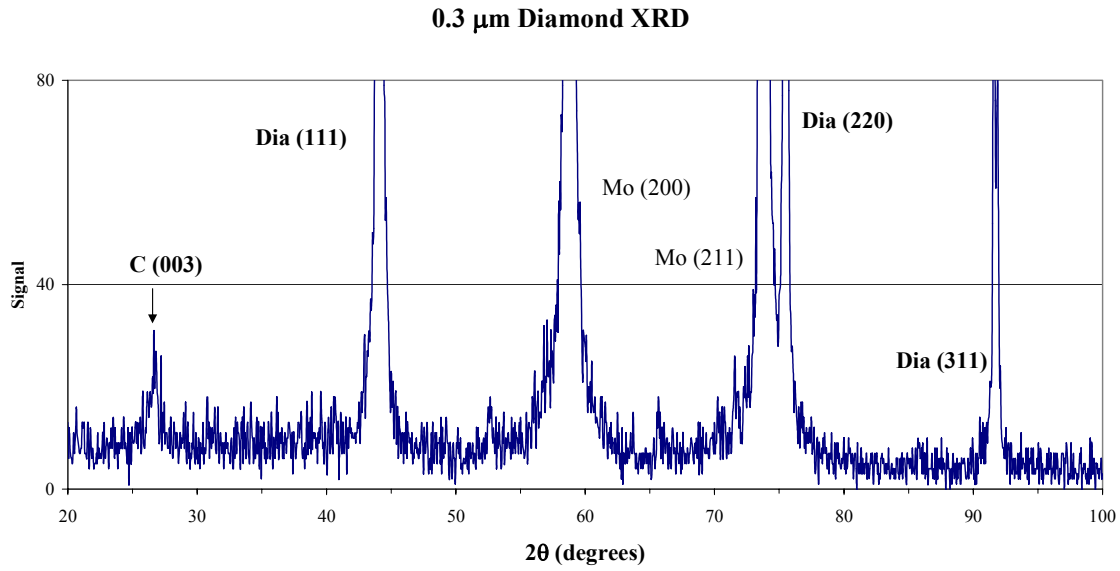

Fig. 3.45 XRD Carbon peak of 0.3 micron Diamond

Because of carbon's low atomic number, sp^2 carbon is very difficult to detect, and only extremely thick films can be effectively measured. Otherwise the diffraction takes place primarily from the substrate and passes directly through the carbon film. Diamond however (sp^3 carbon), because of its dense atomic structure is more effective at diffracting the high-energy x-rays. Depending on individual sample coverage, the molybdenum peaks are typically larger than carbon of either form.

The 1.1 micron average grain size also showed the presence of amorphous carbon which was more easily verified using XPS. The two smallest grain sizes (0.3 and 1.1 micron) were the only two samples which exhibit amorphous carbon in the XRD spectra. However XPS (which is more sensitive to carbon) shows amorphous carbon species in all of the grain sizes as detailed in Sec. 3.3). The abundance of amorphous carbon in the

smallest sizes may be attributed to the process used to manufacture the diamond powders. The XRD spectra for the remaining grain sizes are shown in Figures 3.46-3.58.

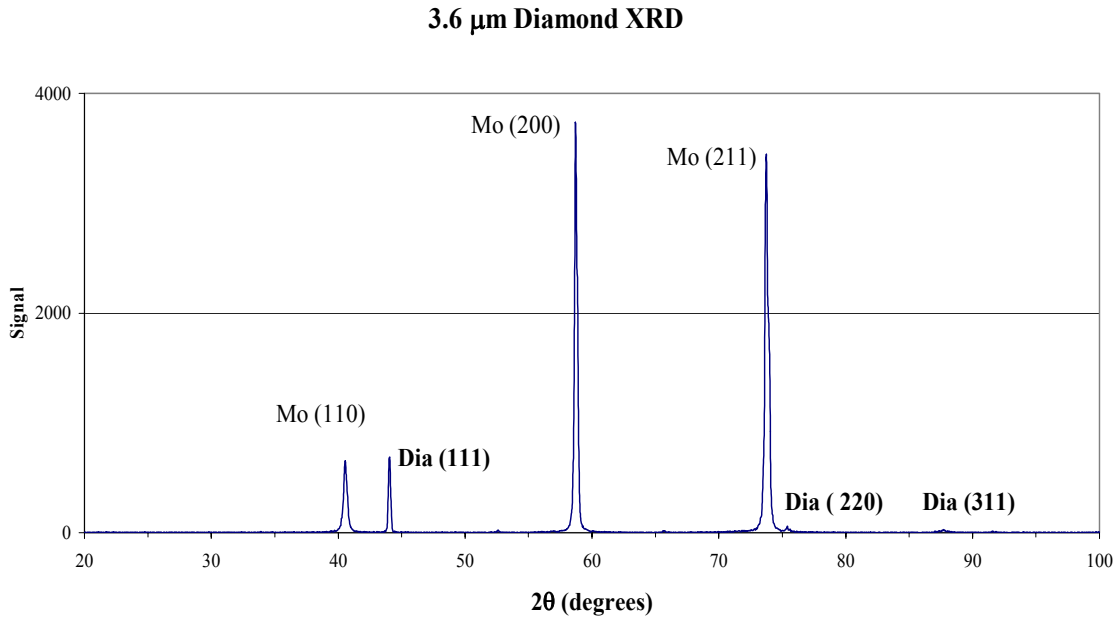

Fig. 3.46 XRD Spectrum for 3.6 micron Diamond

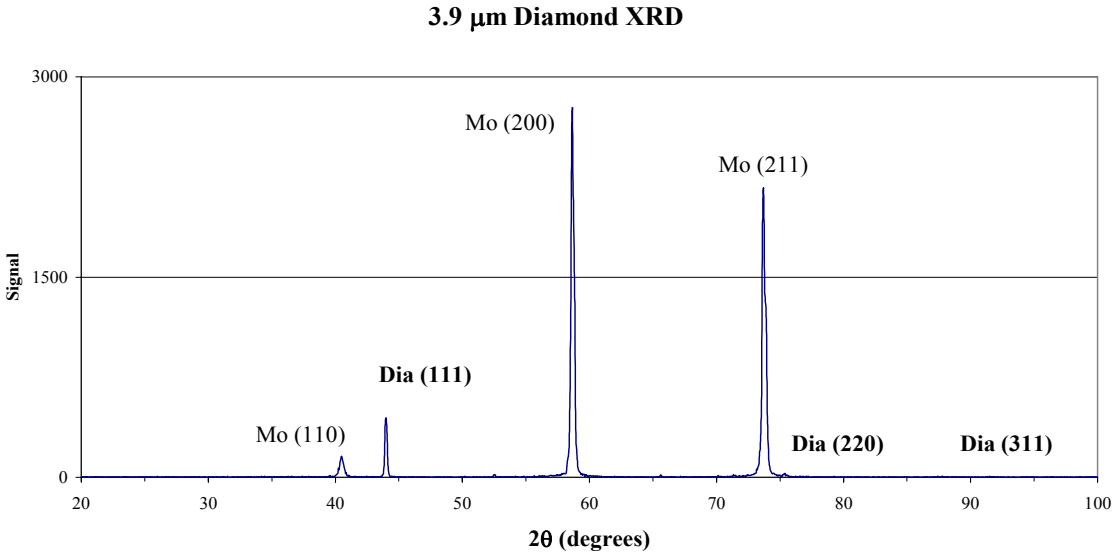

Fig. 3.47 XRD Spectrum for 3.9 micron Diamond

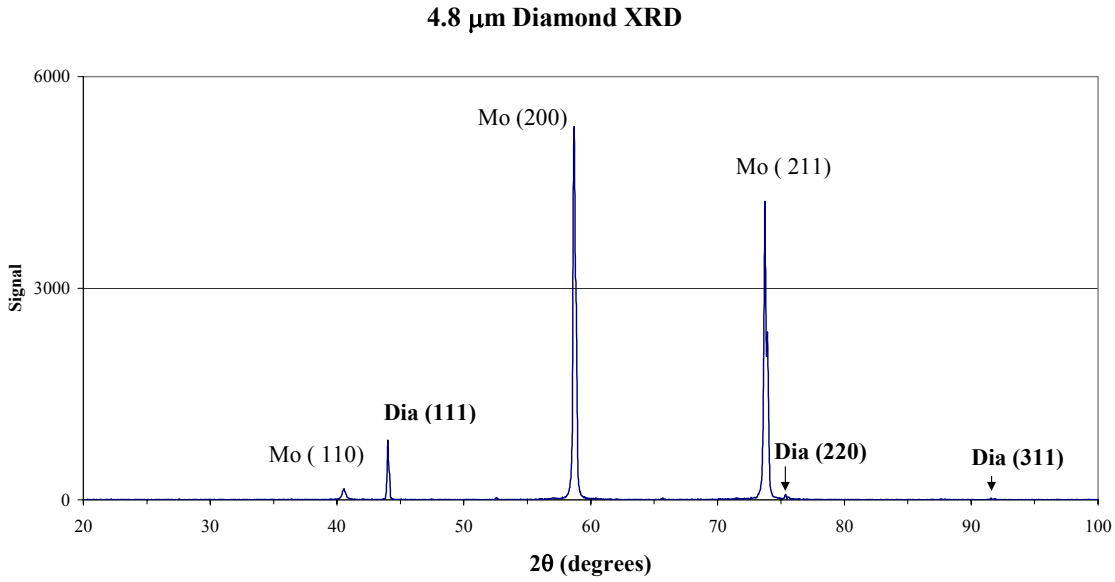

Fig 3.48 XRD Spectrum of 4.8 micron Diamond

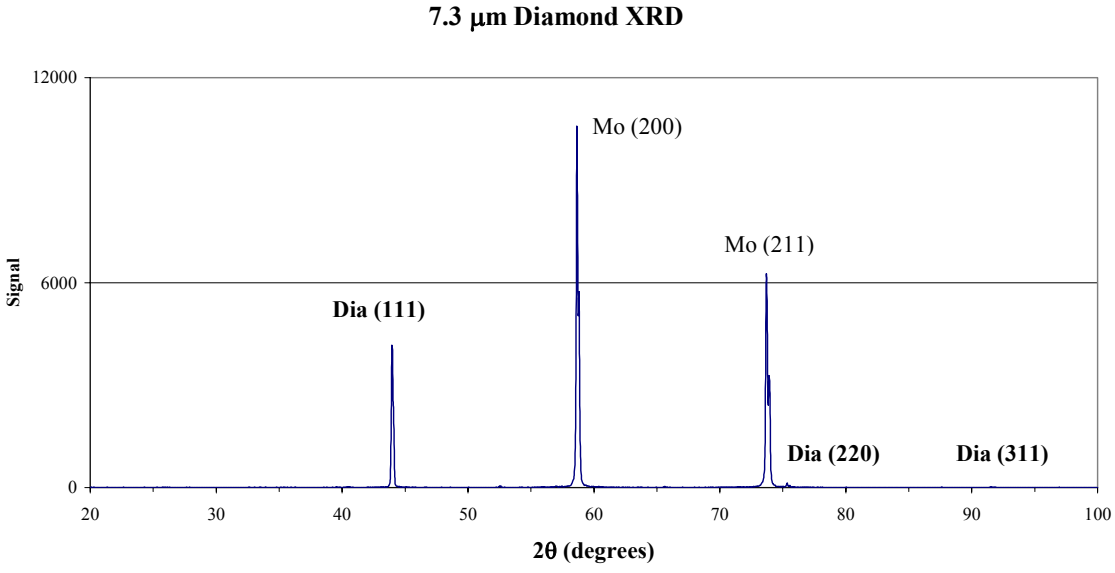

Fig 3.49 XRD Spectrum of 7.3 micron Diamond

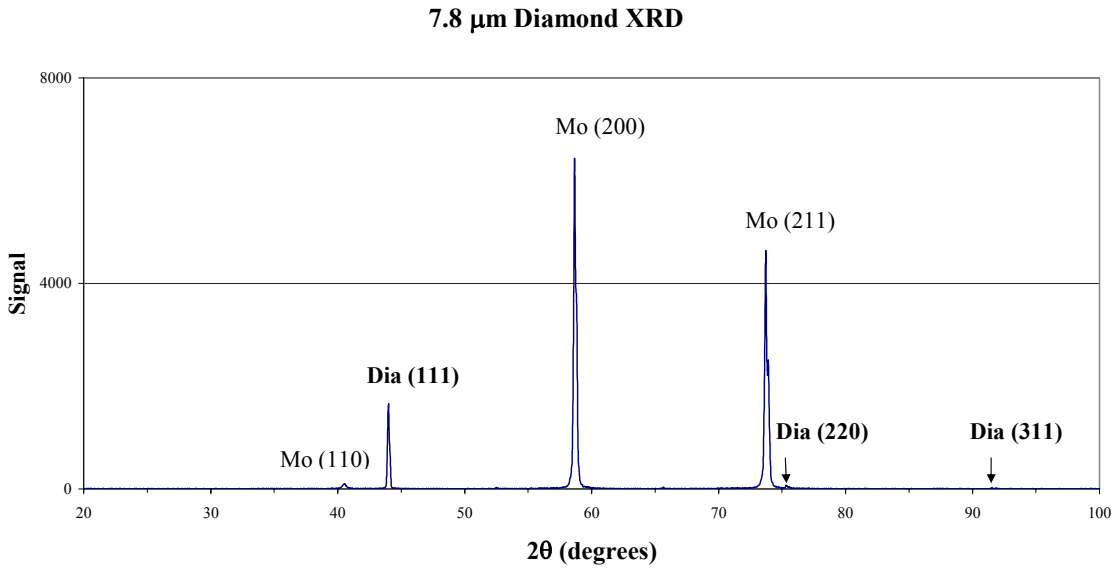

Fig 3.50 XRD Spectrum of 7.8 micron Diamond

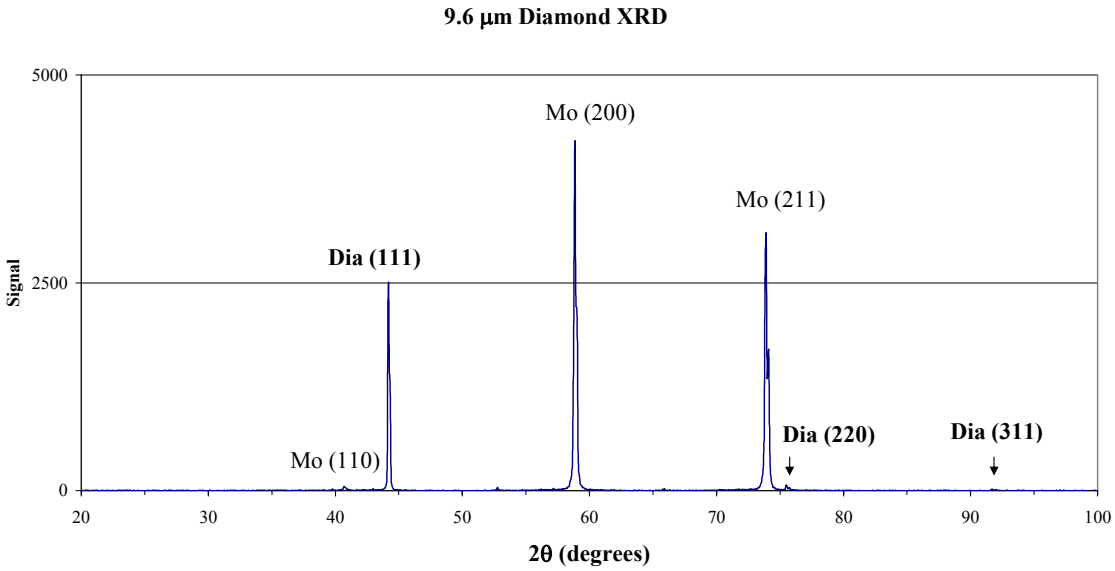

Fig 3.51 XRD Spectrum of 9.6 micron Diamond

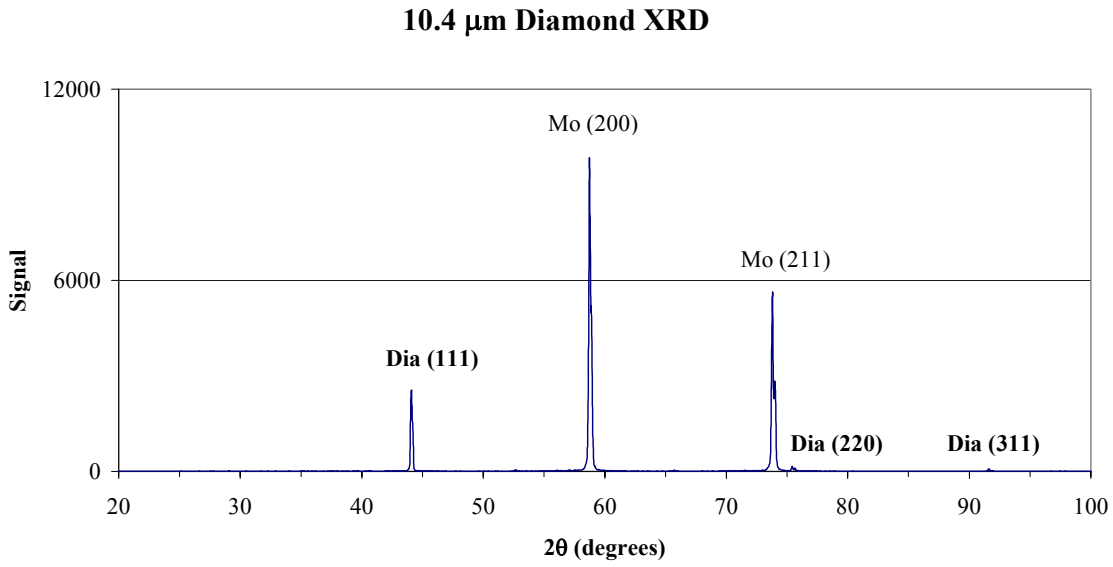

Fig 3.52 XRD Spectrum of 10.4 micron Diamond

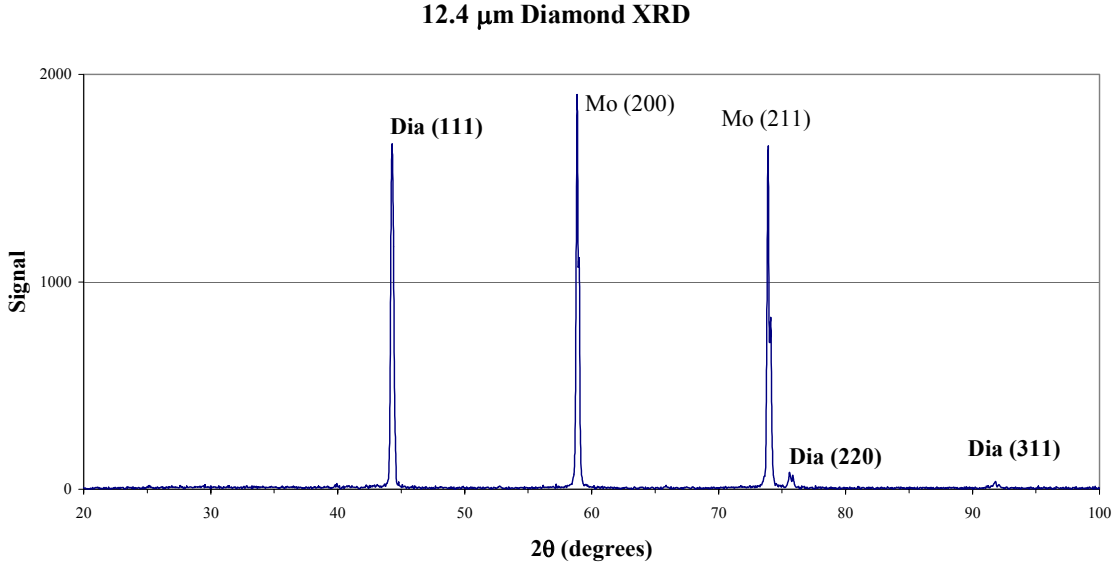

Fig 3.53 XRD Spectrum of 12.4 micron Diamond

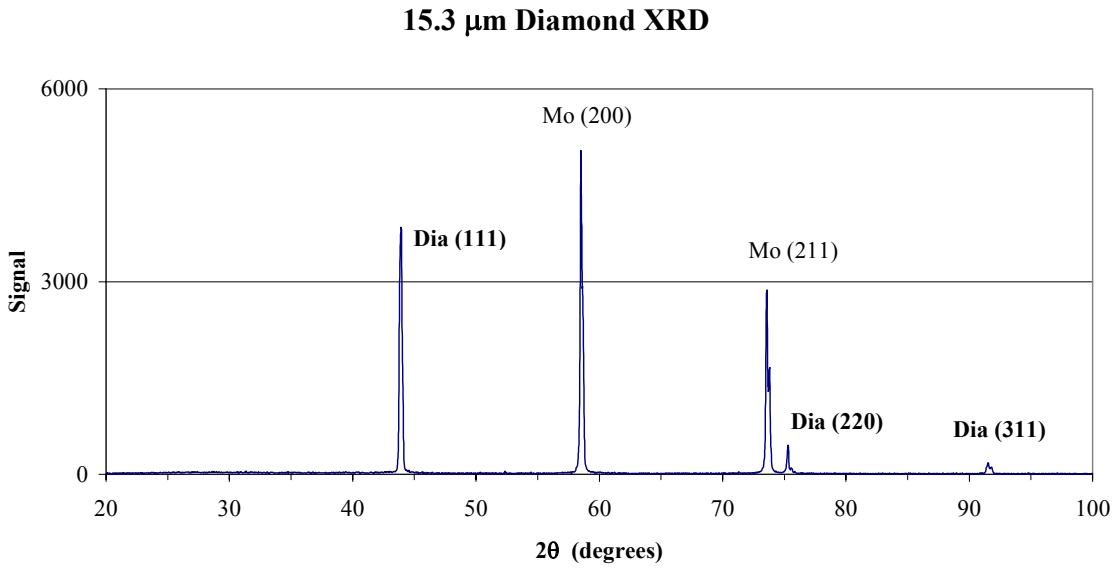

Fig. 3.54 XRD Spectrum of 15.3 micron Diamond

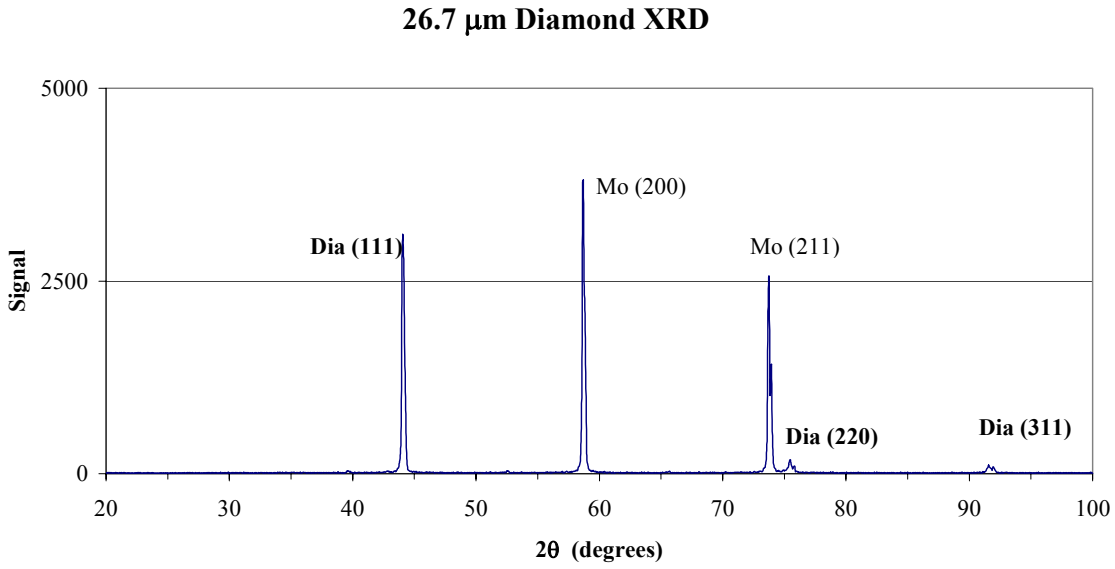

Fig. 3.55 XRD Spectrum of 26.7 micron Diamond

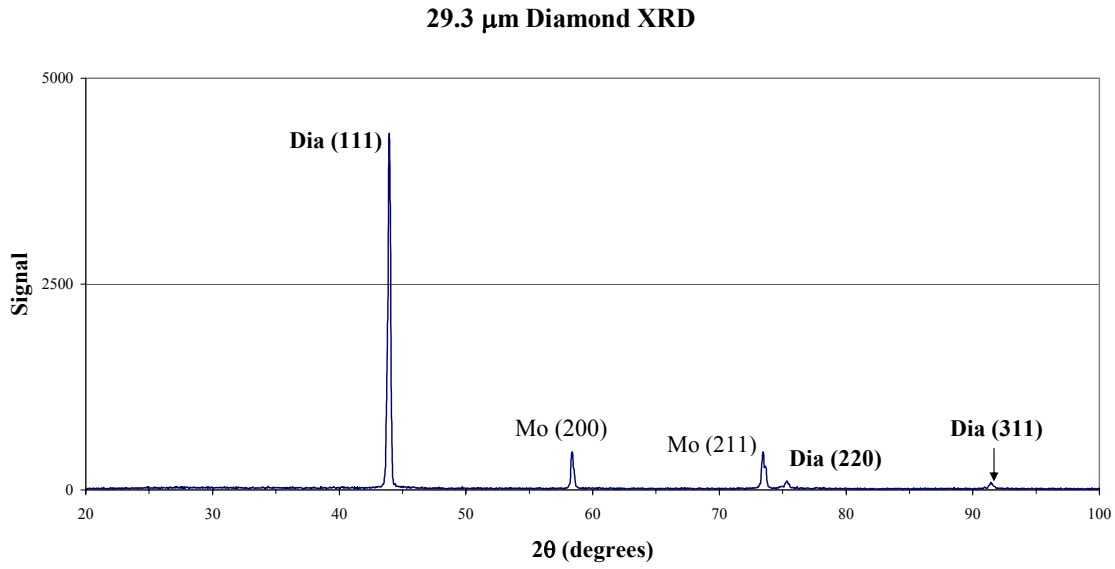

Fig. 3.56 XRD Spectrum of 29.3 micron Diamond

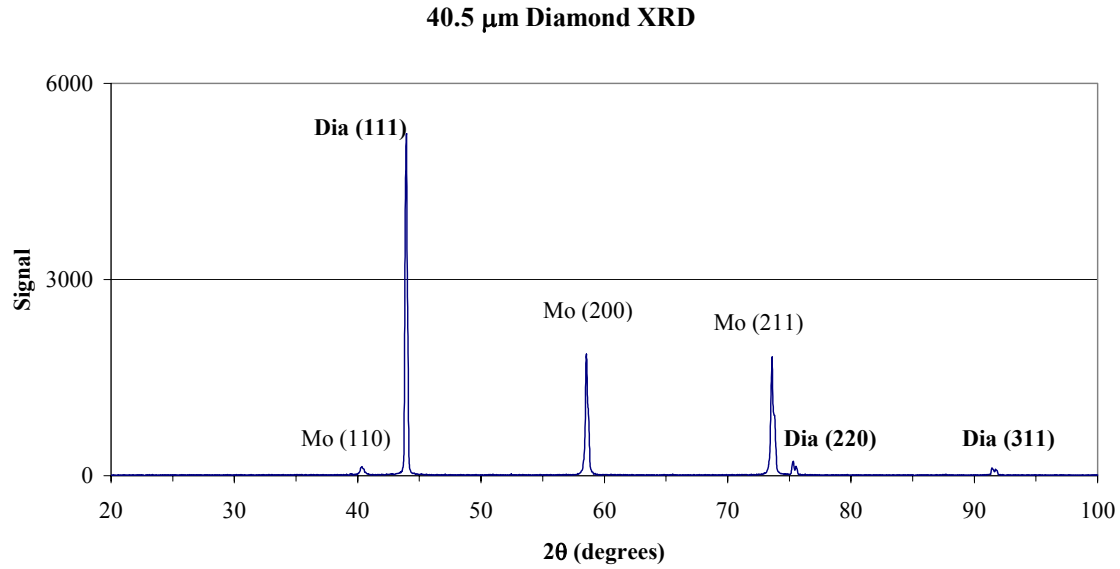

Fig. 3.57 XRD Spectrum of 40.5 micron Diamond

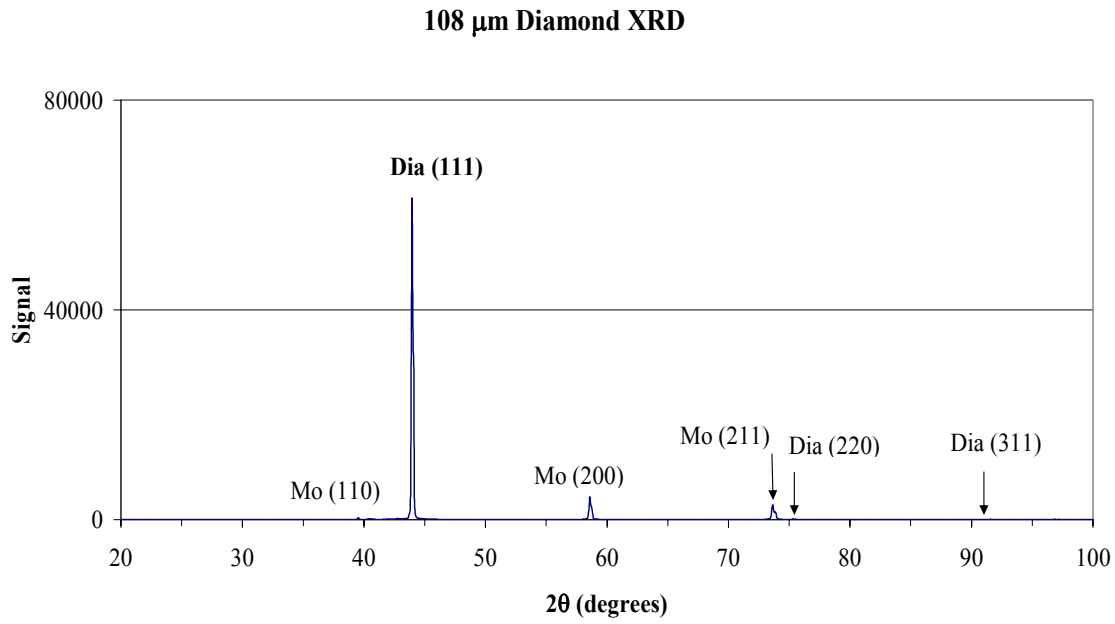

Fig. 3.58 XRD Spectrum of 108 micron Diamond

In all of the samples, the predominant surface of diamond is the (111) plane. Also present are the (220) and (311) planes. The (110), (200) and (211) planes of the molybdenum substrate are also present in varying intensities depending on film thickness. From the areas under the peaks, the abundance of each crystal facing on the surface can be calculated. Because of the NEA associated with the (111) plane of diamond, it was of interest to determine what fraction of the diamond film was comprised of (111) diamond. The film thickness varies among the samples with the smaller grain sizes generally having a thicker coating. However the percentage of (111) for each powder remains independent of the amount of coverage. In the smaller grain sizes containing 75-90% (111) diamond, there is a larger presence of grain boundaries, defects, and graphitic carbon on the surface. Figure 3.59 shows a plot of the (111) fraction to the (200) and (311) planes (and in some cases amorphous carbon peaks).

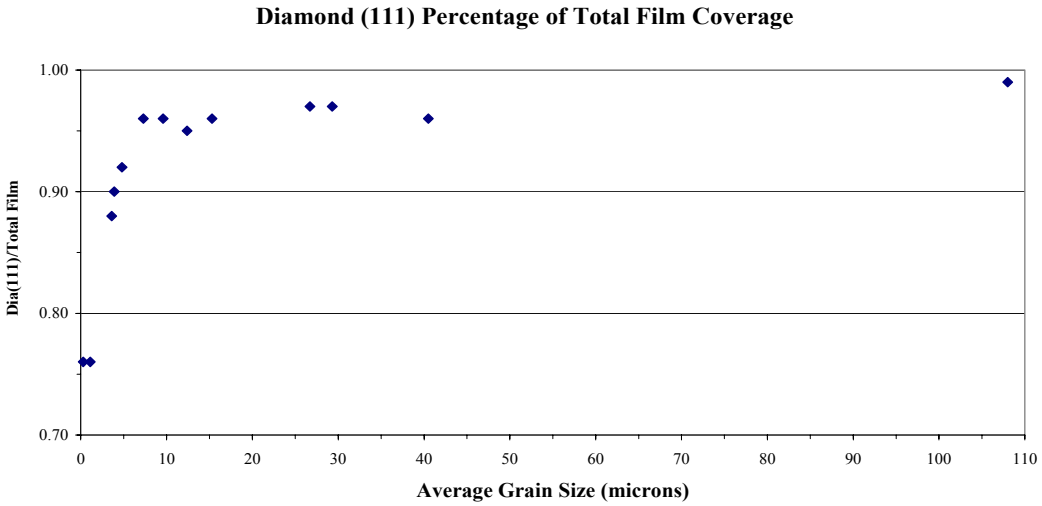

Fig 3.59 Diamond (111) Fraction vs. Average Grain Size

Shown in table 3.4 are the (111) percentages with respect to average grain size.

Average Grain Size (microns)	Diamond (111) Fraction
0.3	0.76
1.1	0.76
3.6	0.88
3.9	0.90
4.8	0.92
7.3	0.96
7.8	0.94
9.6	0.96
10.4	0.95
12.4	0.95
15.3	0.96
26.7	0.97
29.3	0.97
40.5	0.96
108	0.99

Table 3.4 Diamond (111) Fraction

The percentage of the film surface containing the (111) crystal face increases sharply below 10μm. Between 10μm and 108μm the (111) fraction has an asymptotic behavior as it approaches complete (111) coverage. At the largest grain size of 108μm the films contain 99% (111) diamond simulating that of a natural single crystal diamond.

The reason for diamond containing more (111) is attributed to its bonding properties. In the FCC diamond structure, when the s- and p-levels combine to form sp^2 and sp^3 hybrids, it results in bonding and anti-bonding states which split up to form the valence and conduction bands respectively. If the crystal is cleaved along a particular plane, the number of dangling bonds will be dependent upon the plane. The (111) plane contains one dangling bond per unit cell; whereas (100) and (110) planes of diamond each contain two dangling bonds per unit cell [11]. The surface tension is lowest along the (111) direction, so this is natural cleavage plane for diamond (as well as Si and Ge). Pictured in Fig. 3.60 is an example of diamond's natural (111) cleavage. This SEM micrograph of the 108 micron sample shows the triangular structure characteristic of the (111) plane.

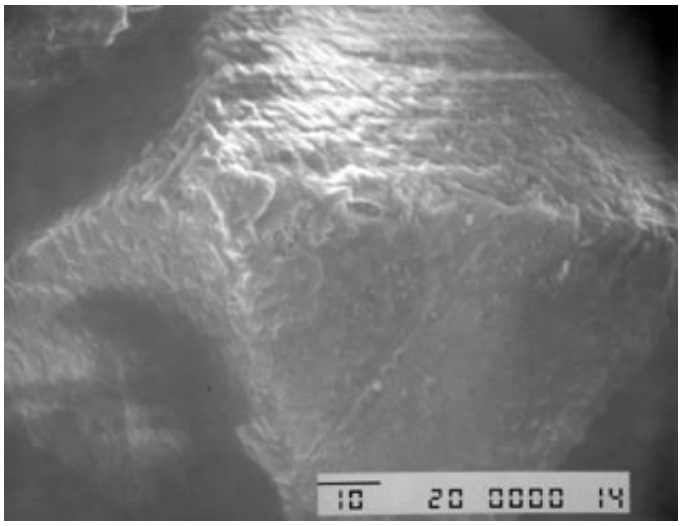

Fig. 3.60 SEM of (111) surface

3.5 THERMAL DESORPTION

3.5.1 Experimental Apparatus

All of the thermal desorption studies were performed in the ESCA system processing chamber under UHV. The samples were annealed using the VG P8 specimen temperature control unit which is standard equipment with the ESCA system and designed to accommodate the Ni sample pegs. This temperature control unit allows for sample heating using a variable low voltage (up to 12V) and high current (up to 16A) supply. The sample is annealed by resistive heating via the heating element which is isolated by a high-temperature ceramic just inside the sample holder. The heating element is a helical section of Ni-chrome heater wire composed of 80% nickel and 20% chromium. Because high temperatures are required to desorb hydrogen from the (111) diamond surface, it was necessary to replace the heating element occasionally when it failed due to excessive currents. The heating element used was a 22 gauge (0.64mm diameter) NiCr wire with a resistivity of 1.015 Ω/ft at room temperature. Approximately 8 inches of wire was tightly wound in a coil 1 inch long to produce a load of ≅0.75Ω. This resistance allows for a current of 16A when the full 12 volts of the supply is applied. However the maximum current rating for the 22 gauge wire is approximately 10A producing a temperature of 850-875°C. As the wire's temperature increases, its resistance also increases; however below 800°C this factor is ≤6% and does not affect the voltage significantly. The applied voltages are well within the range of the power supply. Another factor which contributed to wire's failure was oxidation which made it brittle (the heating element is not inside the vacuum).

The temperature measurements were made using a chromel/alumel (NiCr/NiAl) thermocouple in contact with the sample holder. The thermocouple was calibrated using a 250°C Hg thermometer taking measurements up to 200°C, both of which were in good agreement. Because the thermocouple has a lag in its time to respond to temperature changes, the temperatures were ramped at no more than 20°C/min.

3.5.2 Annealing Procedure

All of the samples were allowed an initial warm-up period at ≈150°C for 20-30 minutes to desorb water from the sample. Afterward, the temperature was ramped up at approximately 20°C/min until a temperature of 750-850°C at which time the sample had a bright orange glow to it. The sample was then held at this temperature for 30-45 minutes. During the anneal, the desorbed gases were monitored using a residual gas analyzer (RGA). Although the adsorbate of interest was hydrogen, several gases were monitored. Atomic hydrogen (H) was not observed in any of the spectra, however there was an abundance of molecular hydrogen (H_2) observed above 725°C. This may indicate that atomic hydrogen from the C-H bond diffuses along the diamond surface to form H_2 before desorbing from the surface. Hydrogen (H and H_2), nitrogen (N_2), water (H_2O), and oxygen (O_2) were monitored during the anneal process. Temperatures were recorded every 25°C during the sample heating and then plotted with the TPD spectrum.

Before the diamond films were annealed, background spectra were taken of the bare molybdenum substrate to observe which species were originating from the substrate, sample peg, wire, etc. A strong onset of H_2 at 550-600°C was observed and is believed to be desorbing from the molybdenum substrate. There is also a strong onset of H_2 from

diamond at 725°C which is well pronounced and is distinguishable from the H_2 signal from the molybdenum which begins at 550°C. Shown in Fig. 3.61 is a background spectrum of the sample holder and Mo substrate.

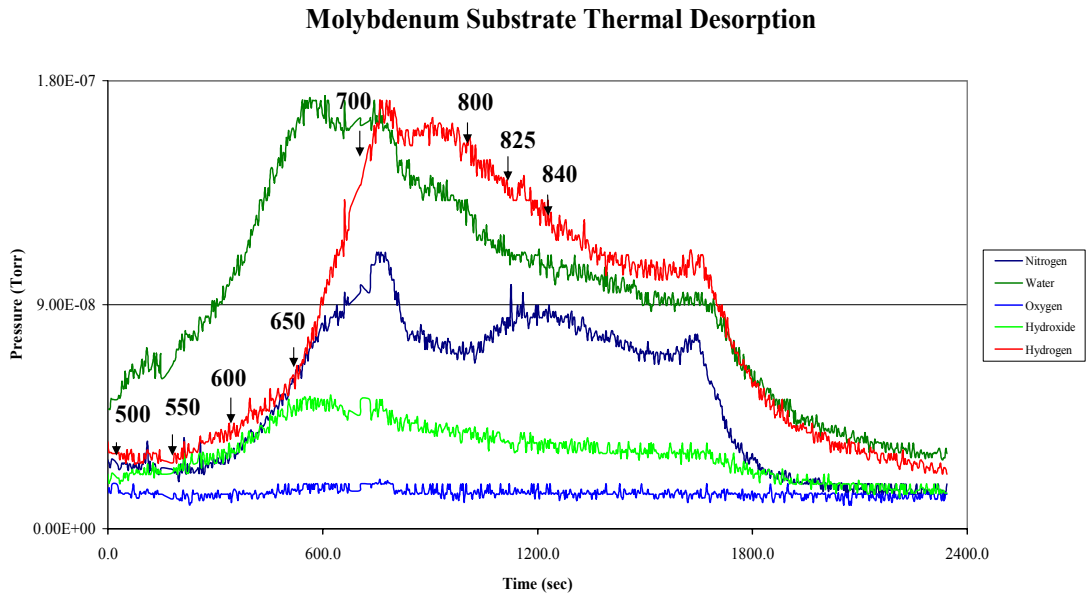

Fig. 3.61 Thermal Desorption Spectra for Mo Substrate

Shown here as the red curve, molecular hydrogen has a strong onset at 550°C and continues to desorb as the temperature is ramped. Just above 700°C, the H_2 has been desorbed from the surface and the H_2 pressure decreases as it is pumped out of the system. There is a sharp decrease at approximately 1600 seconds when the main chamber gate valve was opened to allow for the ion pump to aid in removing the residual gases. The temperature remained at 840°C from 1200 seconds until 2400 seconds when the total pressure had returned to approximately the pressure at the beginning of the anneal.

An anneal of the 3.9 average grain size diamond shows the H_2 partial pressure to increase by an order of magnitude when the sample is brought to 750°C. After an initial

warm up period of 30 minutes at 150°C, the sample temperature was ramped at approximately 20°C/min to a final temperature of 750°C. Once the sample reached 750°C, the temperature was held at this value for 3.5 hours. The spectrum in Fig. 3.62 shows an onset of molecular hydrogen just below 600°C from the molybdenum substrate. The slope then increases at approximately 725°C as a result of hydrogen desorbing from the diamond film.

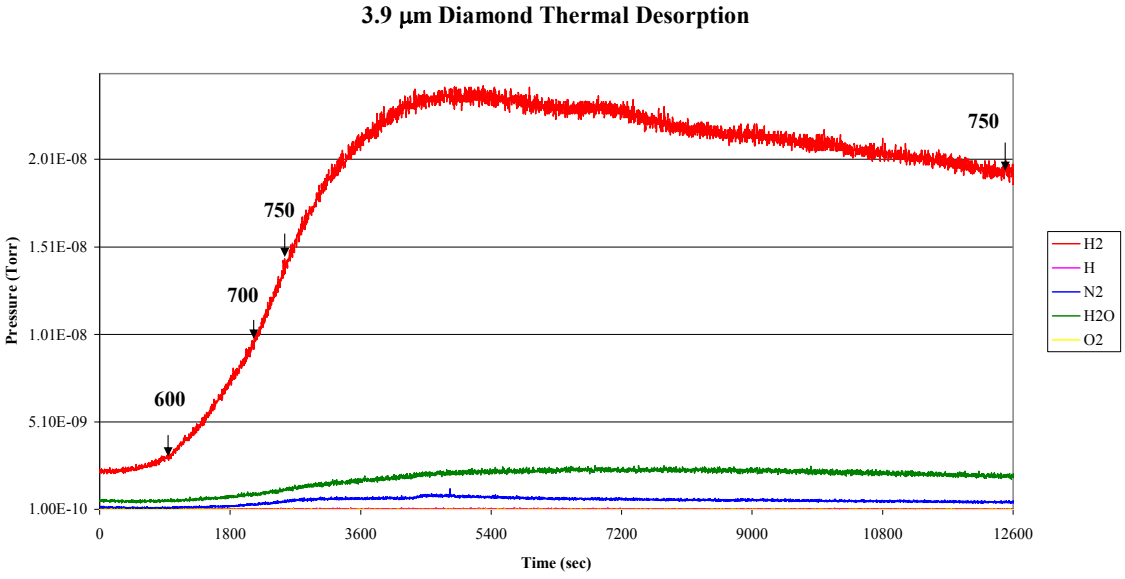

Fig. 3.62 Thermal Desorption Spectra for 3.9 micron Diamond

Atomic hydrogen was monitored, however its partial pressure was in the 10^{-12} Torr range which is comparable to hydrogen levels normally present in the system. The absence of atomic hydrogen is likely due to diffusing along the surface to form molecular hydrogen before desorbing. Because of hydrogen's small size, it is difficult to pump out, and the pressure decreases slowly over the annealing period.

The samples are being annealed to demonstrate that removal of chemisorbed hydrogen raises the work function by changing the electron affinity. These effects are measured by UPS and detailed in Section 3.2.

The 10.4 micron grain size was annealed to near 850°C, which is the upper limit of the apparatus. Ramping the temperature over a period of 1.5 hours, the temperature reached approximately 840°C before the heating element failed. Shown in Fig. 3.63 is the desorption spectra.

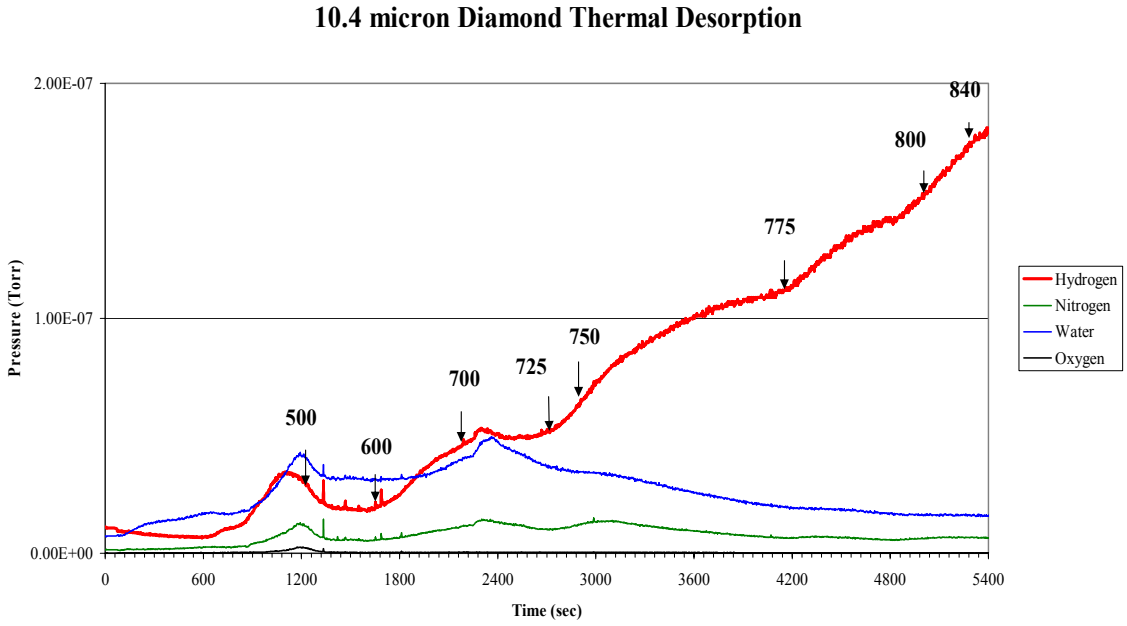

Fig. 3.63 Thermal Desorption Spectra for 10.4 micron Diamond

At the point where the heating element fails, the H_2 pressure is continuing to increase. This indicates hydrogen is still being desorbed from the surface. Once the chemisorbed hydrogen has been removed from the surface, there is a decrease in H_2 pressure as the desorbed hydrogen is being pumped out by the turbo-molecular and ion pumps.

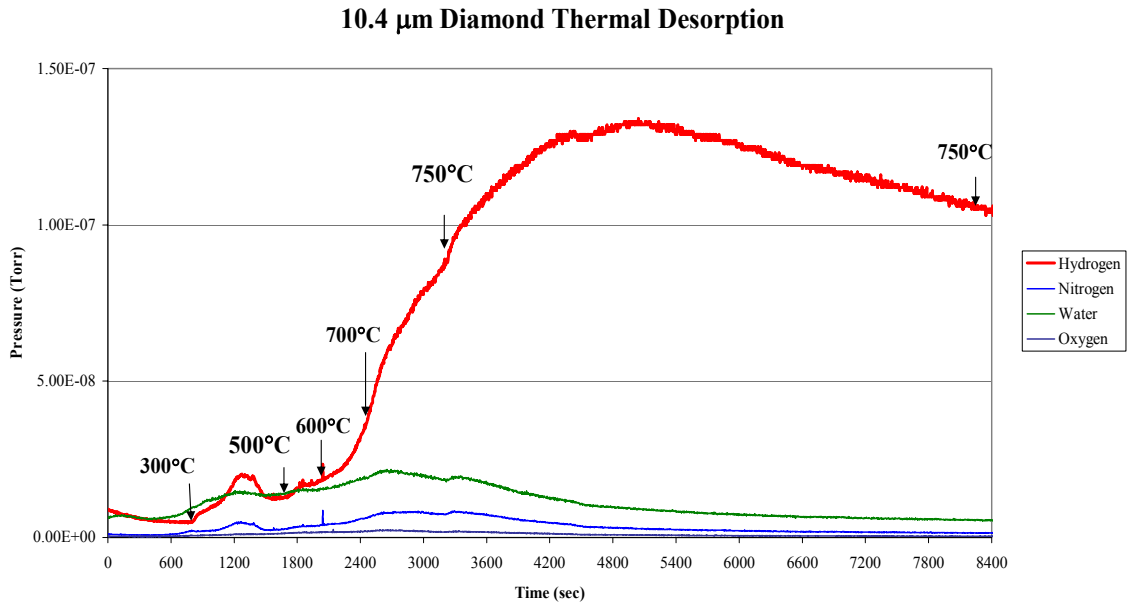

Fig. 3.64 Thermal Desorption Spectra of 10.4 µm Diamond (2nd Anneal)

Shown in Fig. 3.64 is a second annealing of this sample where the temperature was held at 750°C for approximately 1.5 hours. This was sufficient to desorb the surface hydrogen as evidenced by the decrease in H_2 partial pressure. In this figure, the H_2 pressure begins to decrease at approximately 1hr 20min (5200 sec). The sample temperature was then held fixed at 750°C to allow the hydrogen to be removed via the ion and turbo pumps. As discussed in Sec. 3.2, a sufficient amount of hydrogen was desorbed from the surface to change the work function significantly. The sample before heating had a work function on 3.9 eV and afterward had been raised to 4.6 eV.

The 4.8 micron grain size was annealed over a period of 25 minutes to a final temperature of 700°C. This spectrum shows a strong onset of H_2 desorbing from the

substrate at 550°C, then another sharp increase at approximately 650°C from the diamond film as shown in Fig. 3.65.

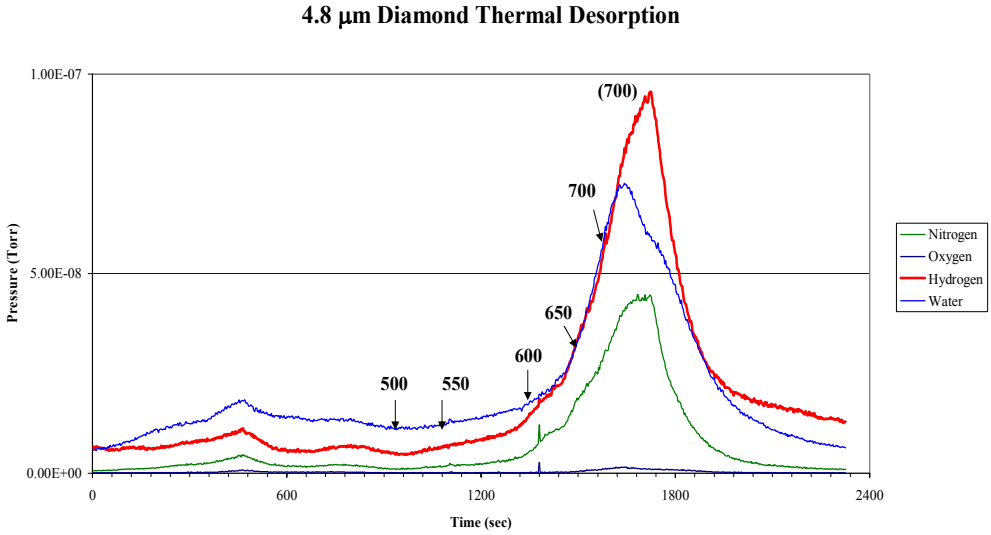

Fig. 3.65 Thermal Desorption Spectra of 4.8 Diamond

Because the heating element failed, the sample was kept in UHV until a second annealing was performed. This is shown in Fig. 3.66.

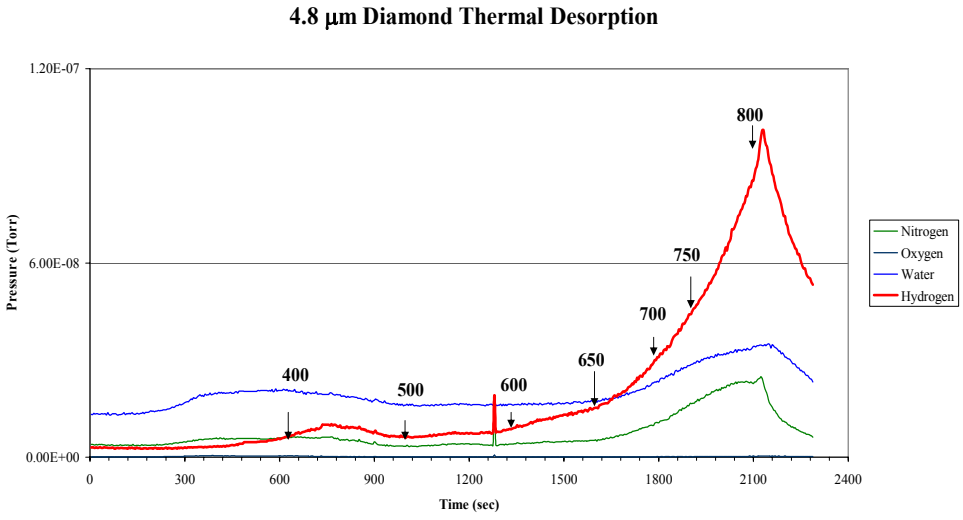

Fig. 3.66 Thermal Desorption Spectra of 4.8 micron Diamond (2nd Anneal)

Because a significant amount of hydrogen was desorbed from the molybdenum substrate on the first heating, the H_2 onset at 550°C is not as prominent. Just below 700°C the molecular hydrogen pressure increases and continues until a maximum temperature of 800°C is reached. Again the surface work function increased dramatically. Before heating, the work function was 3.3 eV and afterward had increased to 4.8 eV.

The average grain size of 3.6 microns was also annealed as shown in Fig. 3.67.

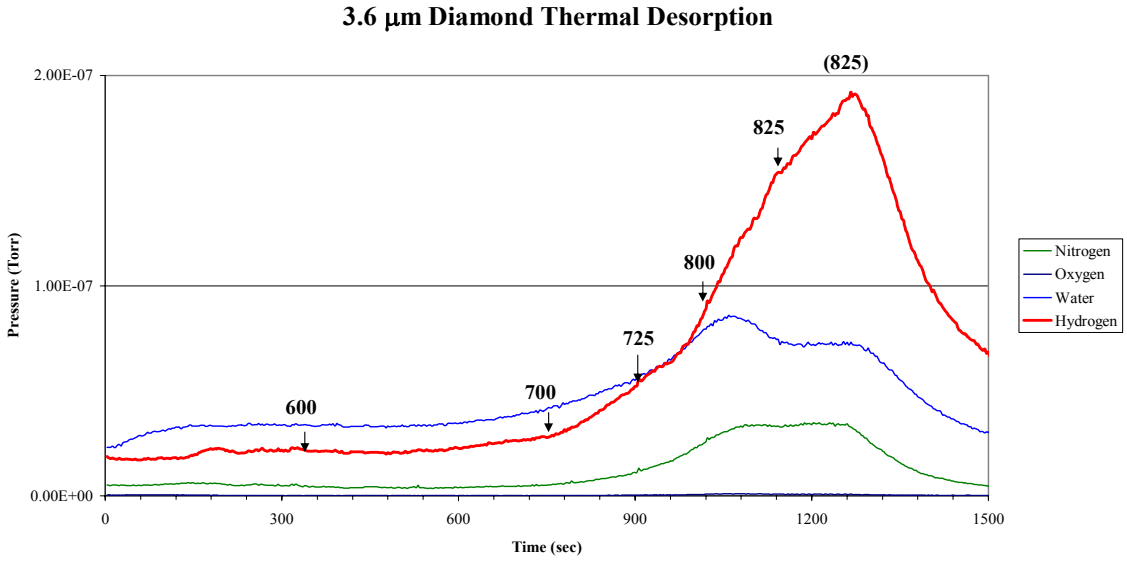

Fig 3.67 Thermal Desorption Spectra for 3.6 micron Diamond

This spectrum shows again the strong onset of molecular hydrogen desorbing from the diamond surface at approximately 700°C and increasing as the temperature reaches a final value of 825°C. Consequently, the work function increased from 3.3 eV to 4.4 eV.

3.6 SURFACE STATES

Shown in Fig. 3.68 is the spectrum for electrons excited with 3.51 eV photons from the 3.9 micron diamond surface.

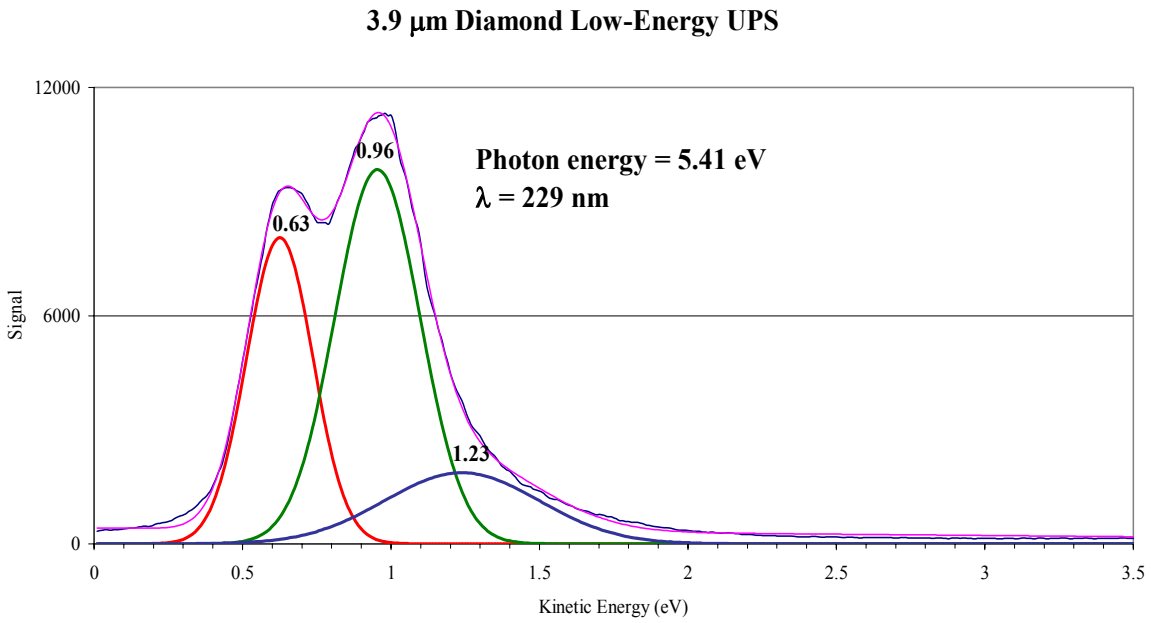

Fig. 3.68 Low Energy UPS of 3.9 micron Diamond (229nm)

The source used was a Coherent argon ion laser operating in second harmonic generation (SHG) mode producing a 229nm line from the 458nm fundamental line by a frequency-doubling crystal. The power of this beam was typically 8-10 mW, with a special resolution of approximately $2mm^2$. Because the diamond surface fluoresces when irradiatied with ultraviolet photons, the laser produced a bright spot which was a pale green in color. The fluorescence also made it possible to easily align the laser to the center of the spectrometer. Maximizing the count rate of signal was also used to verify alignment of the laser spot.

The 229 nm line produces a photon energy of 5.41 eV, and the beam is directed into the UHV chamber via a quartz window in the ESCA system. Shown in Fig. 3.69 is the low-energy UPS spectrum for the same sample using a photon energy of 3.51 eV.

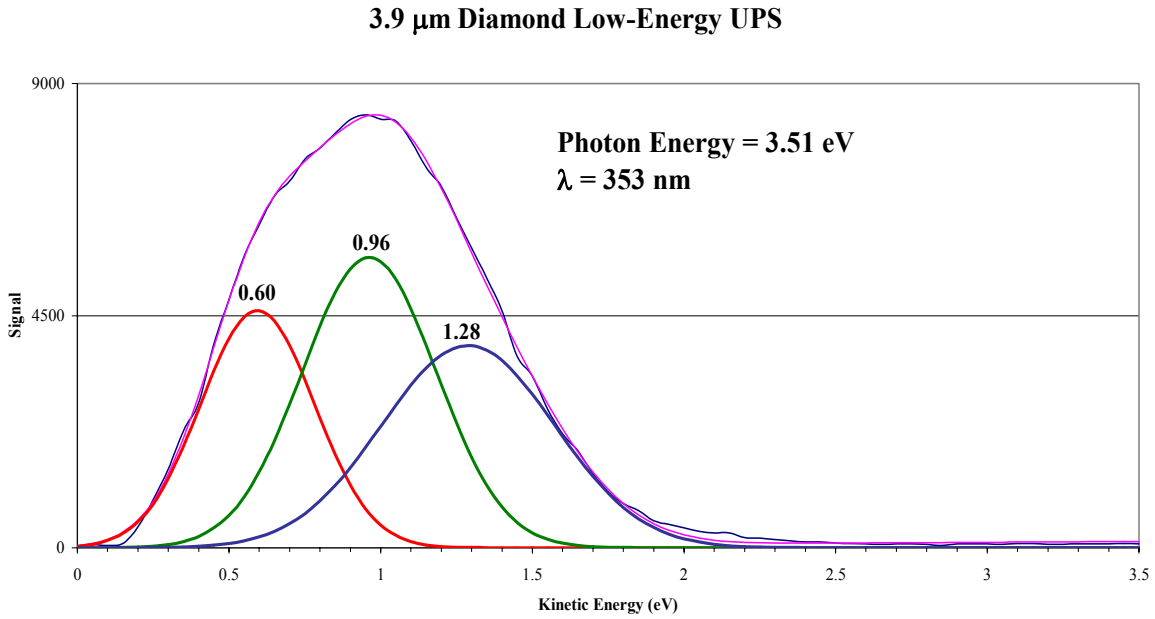

Fig. 3.69 Low Energy UPS of 3.9 micron Diamond (353 nm)

The fitted peaks for both spectra show structures in the same positions (within the resolution of the spectrometer). The incident radiation used her has a wavelength of 353 nm (hν=3.51 eV) and is shifted in energy by 1.9 eV. The laser operates in high tension mode for this particular line, and the use of a frequency-doubling crystal is unnecessary. This is the highest frequency possible in the "single line mode" which operates without the use of a crystal to double the frequency of a fundamental line.

For comparison, average grain sizes from both ends of the size spectrum are shown in Figures 3.70 and 3.71.

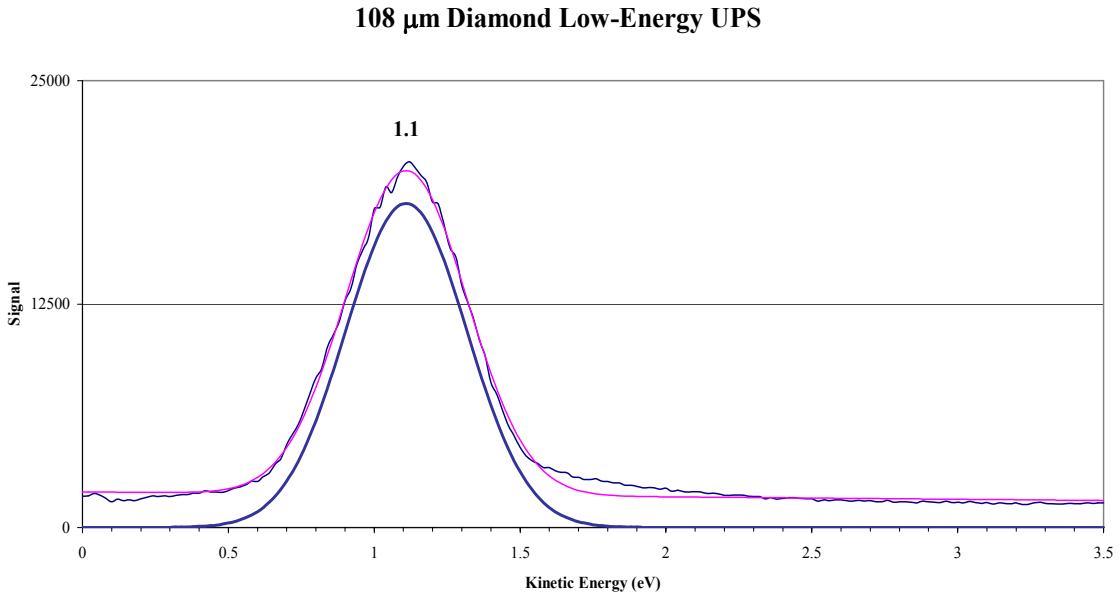

Fig. 3.70 Low Energy UPS of 108 micron Diamond (229nm)

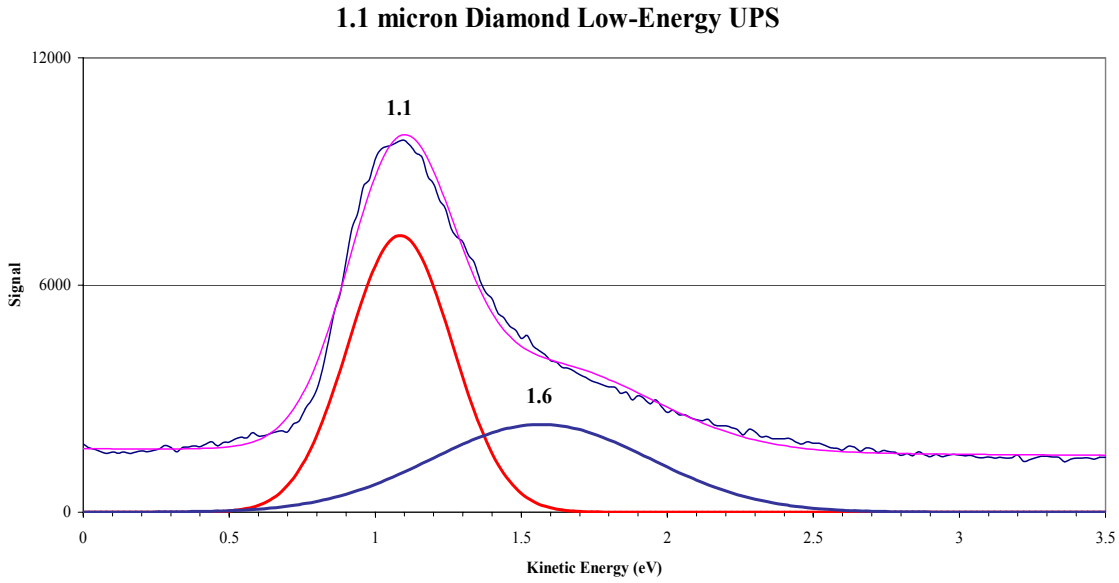

Fig. 3.71 Low Energy UPS of 1.1 micron Diamond (229nm)

The 108 micron grain size has a single surface state at 1.1 eV which has been documented in work on single-crystal (111) diamond [14]. The fact that it exhibits only one may be attributed to the large surface areas of the crystallites. Because the surface of the film is comprised of large, smooth planes, there may be less defects contributing to surface states. The 1.1 micron sample also shows this structure at 1.1 eV however there is a second peak at 1.6 eV. These are both as-prepared samples. Pictured in Fig. 3.72 is the spectrum for the same 1.1 micron sample after annealing.

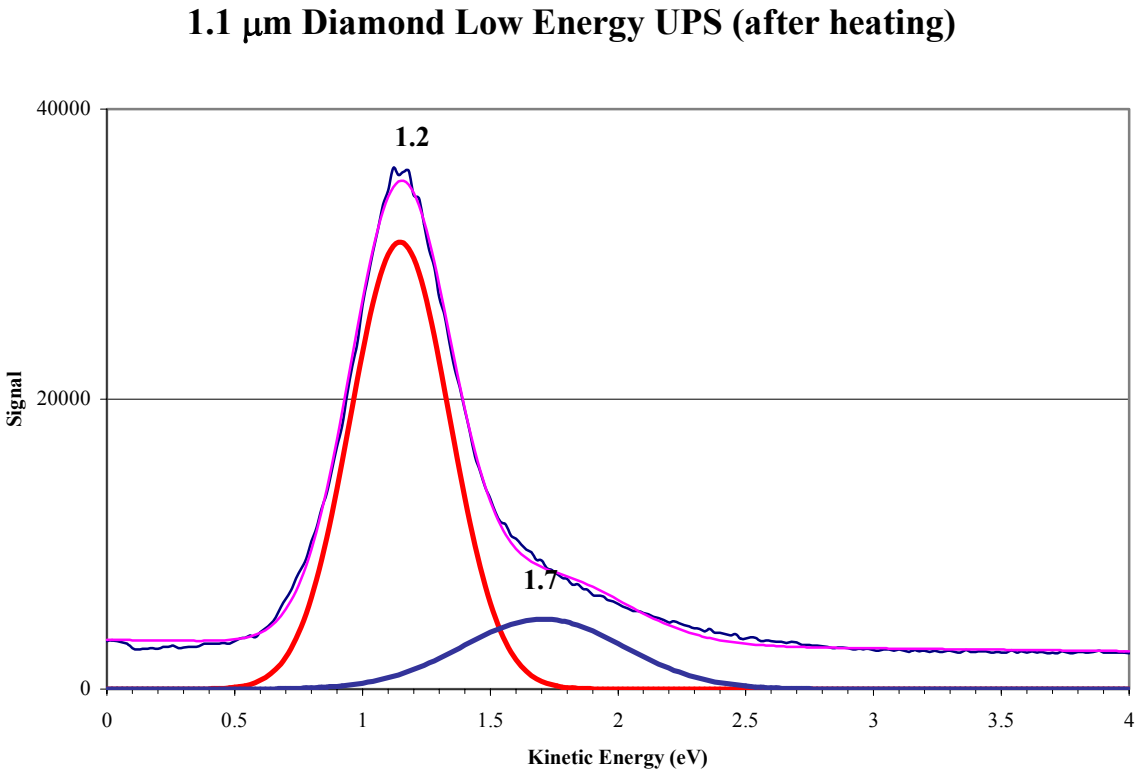

Fig. 3.72 Low Energy UPS of 1.1 micron Diamond (after annealing)

After annealing the sample at 750°C for one hour, both states have shifted in energy by 0.1 eV. The resolution used in all of the low-energy UPS measurements is 20 meV, which allows accurate measurement of the 0.1 eV shift in energy.

REFERENCES

[1] David R. Lide ed., *CRC Handbook of Chemistry and Physics, 73rd ed.*, CRC Press Inc., Boca Raton, 1992, p.12-108
[2] G. S. Painter, D. E. Ellis, and A. R. Lubinsky, Phys. Rev. **B4**, 3610 (1971).
[3] F. J. Himpsel, J. F. van der Veen, and D. E. Eastman, Phys. Rev. **B22**, 1967 (1980).
[4] F. R. McFeely, S. P. Koalczyk, L. Ley, R. G. Cavell, R. A. Pollak and D. A. Shirley, Phys. Rev. **B9**, 5268 (1974).
[5] M. W. Geis *et al*., Appl. Phys. Lett. **68**, 2294 (1996)
[6] G. R. Brandes and A. P. Mills Jr., Phys. Rev. B **58**, 4952 (1998)
[7] D.D. Koleske *et. al*., J. Chem. Phys. **102** (2), 992 (1995)
[8] R.E. Thomas, R.A. Rudder, and R.J. Markunas, J. Vac. Technol. A, **10**, 2451 (1992)
[9] B.B. Pate *et. al*., J. Vac. Technol., **19** (3), 349 (1981)
[10] M.T. Schulberg, *et. al*., J. Appl. Phys., **77**, 3484 (1995)
[11] I.L. Krainsky and V.M. Asnin, Phys. Rev. B **56**, 13529 (1997)
[12] Andrew Zangill, *Physics at Surfaces*, Cambridge University Press, New York 1988
[13] See e.g. Peakfit 4, SPSS Science, 233 S. Wacker Drive, 11th floor, Chicago, IL 60606-6307
[14] F. J. Himpsel, D. E. Eastman, P. Heimann, and J. F. van der Veen, Phys. Rev. B **24**, 7270 (1981)

CHAPTER 4 – CONCLUSIONS

The variation of the work function of polycrystalline diamond was studied for a range of grain sizes from 0.3 to 108 microns [1]. Grain sizes were measured by scanning electron microscopy and size distributions determined. The percentage of diamond (111) was found to increase from 76% to 99% as the grain size increased from 0.3 to 108 microns. The work function has a maximum of about 5.1 eV at 0.3 microns, then decreases with increasing grain size to a minimum of 3.2 eV at an average grain size of about 4 microns, and then increases to a value of 4.8 eV at a grain size of 108 microns. The results are consistent with a model in which the crystallites are comprised of three components as illustrated in Fig. 4.1: (1) diamond (111) crystallites, (2) negative electron affinity regions near the outside edges due to defects and (3) graphitic/amorphous carbon grain boundaries beyond the crystallite edges.

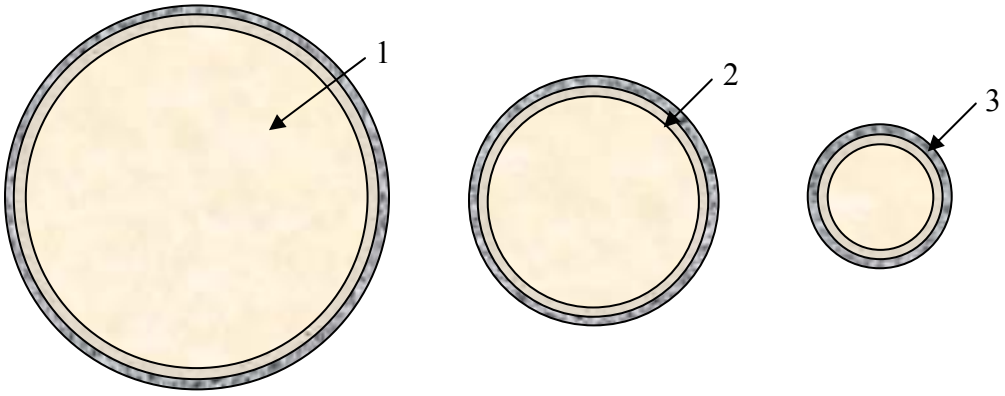

Fig. 4.1 Diamond Crystallite Regions

At the largest grain sizes (Fig. 4.1a), the work function reflects that of (111) crystalline diamond, while the outer regions are negligible. As the grain size decreases (Fig. 4.1b), the work function decreases as the fractional area of defects (negative electron affinity regions) becomes significant with less contribution from the other two regions. At the smallest grain sizes (Fig. 4.1c) the grain boundary becomes significant and the measured work function is representative of graphite/amorphous carbon. This model is supported by scanning tunneling field emission results that found emission sites for diamond (111) to be localized near the crystallite boundaries [2], and photoemission studies that characterized the grain boundaries of both single-crystal diamond and polycrystalline diamond as sp^2 [3]. In addition, the model for the larger grain sizes is supported by studies on large-area mosaic diamond films approaching single-crystal quality [4].

Surface states of polycrystalline diamond films were measured by low-energy ultraviolet photoelectron spectroscopy using photon energies of 5.41 eV and 3.51 eV. Surface states were found to exist within the band gap at kinetic energies of 0.6 eV, 0.9 eV, 1.2 eV, and 1.7 eV. In this work, the negative electron affinity of diamond is attributed to hydrogen termination of the (111) plane and thermal desorption studies were performed to desorb the attached hydrogen. After annealing above 750°C, samples exhibited an average increase in work function of 1.2 eV as a result of diminishing negative electron affinity.

The large change in work function (almost a factor of two) could be useful to make conductors with different work functions for microelectronic gate structures.

REFERENCES

[1] Patrick Abbott, Edward D. Sosa, and David E. Golden, Appl. Phys. Lett. **79**, 2835 (2001)

[2] A. T. Rakhimov, N. V. Seutin, E. S. Soldatov, M. A. Timofeyev, A. S. Trifonov, V. V. Khanin, and A. Silzars, J. Vac. Sci Technol. B **18**, 75 (2000)

[3] J. B. Cui, J. Ristein, and L. Ley, Phys. Rev. B **60**, 16135 (1999)

[4] M. W. Geis, Henry I. Smith, A. Argoitia, J. Angus, G. H. M. Ma, J. T. Glass, J. Butler, C. J. Robinson, and R. Pryor, Appl. Phys. Lett. **58**, 2485 (1991)

REFERENCES

Abbott, Patrick, Edward D. Sosa, and David E. Golden, Appl. Phys. Lett. **79**, 2835 (2001)

Albin, S., W. Fu, A. Varghese, and A.C. Lavarias, J. Vac. Sci. Technol. A **17**, 2104 (1999)

Andrews, Anthony T., *Electrophoresis – Theory, Techniques, and Biochemical and Clinical Applications*, Clarendon Press, Oxford 1986

Baker, A.D., *Photoelectron Spectrsocopy*, Pergamon Press, Oxford 1972

Bandis, C. and B. B. Pate, Phys. Rev. B **52**, 12056 (1995)

Bell, R. L., *Negative Electron Affinity Devices*, Clarendon, Oxford, 1973

Benjamin, M. C., C. Wang, R. F. Davis, and R. J. Nemanich, Appl. Phys. Lett. **64**, 3288 (1994)

Berglund, C. N., and W. E. Spicer, Phys. Rev. **136**, A1030 (1964)

Bier, Milan, *Electrophoresis – Theory, Methods and Applications Vol. 1*, Academic Press Inc., New York, 1959

Bier, Milan, *Electrophoresis – Theory, Methods, and Applications Vol. 2*, Academic Press Inc, New York 1967

Brandes, G. R. and A. P. Mills Jr., Phys. Rev. B **58**, 4952 (1998)

Briggs, D. and M.P.Seah, *Practical Surface Analysis*, John Wiley & Sons Inc., Chichester, 1995

Carlson, Thomas A., *Photoelectron and Auger Spectroscopy*, Plenum Press, Reading, Massachusetts 1978.

Choi, W. B., *et al*., J. Vac. Sci. Technol. B, **16** (1998)

Choi, W. B., *et. al.*, Appl. Phys. Lett. **68**, 720 (1996)

Cui, J. B., J. Ristein, and L. Ley, Phys. Rev. Lett. **81**, 429 (1998)

Cui, J. B., et al., J. Appl. Phys. **88**, 3667 (2000)

Cui, J. B., J. Ristein, and L.Ley, Phys. Rev. B **59**, 5847 (1999)

Cui, J. B., J. Ristein, and L. Ley, Phys. Rev. B, **60**, 16 135 (1999)

Cullity, B.D., *Elements of X-Ray Diffraction*, Addison-Wesley, New York, 1975

Debye, P. and E. Huckel, Ann. D. Physik. Z., **24**, 305 (1924)

Deyl, Z. ed., *Electrophoresis – A Survey of Techniques and Applications, Part A: Techniques*, Elsevier Scientific Publishing Co., Amsterdam, 1979

Einstein, A., Annalen der Physik, **17**, 132-148 (1905)

Feuerbacher, B., B. Fitton, and R. F. Willis ed., *Photoemission and the Electronic Properties of Surfaces*, Wiley & Sons, Ltd., Chichester, 1978

Geis, M. W. and M.A. Tamer, *Encyclopedia of Applied Physics*, VCH, Weinheim, 1993, Vol. 5, P. 2.

Geis, M. W., Henry I. Smith, A. Argoitia, J. Angus, G. H. M. Ma, J. T. Glass, J. Butler, C. J. Robinson, and R. Pryor, Appl. Phys. Lett. **58**, 2485 (1991)

Geis, M. W. *et al*., Appl. Phys. Lett. **68**, 2294 (1996)

Geis, M. W., *et. al*., J.Vac. Sci. Technol. A **6**, 1953 (1988)

Griem, H. R., *Plasma Spectroscopy*, McGraw-Hill, New York, 1964

Hamza, A.V., G. D. Kubiak, and R. H. Stulen, Surface Sci. Lett. **206**, L833 (1988)

Heald, Mark A. and Jerry B. Marion, *Classical Electromagnetic Radiation 3rd ed*., Saunders College Publishing, Fort Worth 1995

Himpsel, F. J. et al., Phys. Rev. B **20**, 624 (1979)

Himpsel, F. J., J. F. van der Veen, and D. E. Eastman, Phys. Rev. **B22**, 1967 (1980)

Himpsel, F. J., D. E. Eastman, P. Heimann, and J. F. van der Veen, Phys. Rev. B **24**, 7270 (1981)

Hsu, W. L., et al., Appl. Phys. Lett. **55**, 2739 (1989)

Ibach, H., *Electron Spectroscopy for Surface Analysis*, Springer-Verlag: New York, 1977

Jackson, J. D., *Classical Electrodynamics 3rd ed*., John Wiley & Sons, Inc., New York 1998

JADE software e.g., Materials Data Inc., 1224 Concannon Blvd., Livermore, California 94550

Jenkins, Ron, *Introduction to X-ray Powder Diffractometry*, John Wiley & Sons, New York, 1996

Jorgenson, James W. ed. And Marshall Phillips ed., *New Directions in Electrophoretic Methods*, American Chemical Society, Washington D.C. 1987

Kane, Evan O., Phys. Rev. **127**, 131 (1962)

Kasap, S. O., *Principles of Electrical Engineering Materials and Devices*, McGraw-Hill, 1996

Kittel, C., *Introduction to Solid State Physics*, Wiley & Sons Inc., Brisbane, 1996

Koleske, D. D., *et. al*., J. Chem. Phys. **102** (2), 992 (1995)

Krainsky, I. L. and V.M. Asnin, Phys. Rev. B **56**, 13529 (1997)

Kubiak, Glenn D., and Kurt W. Kolanski, J. Vac. Sci. Technol. A **6**, 814 (1988)

Kuyatt, C. E., and J. A. Simpson, Rev. Sci . Instr. **38**, 103 (1967)

Lee, S. T. and G. Apai, Phys. Rev. B **48**, 2684 (1993-II)

Lide, David R. ed., *CRC Handbook of Chemistry and Physics, 73rd ed*., CRC Press Inc., Boca Raton, 1992

McClure, M. T. R. Schlesser, B. L. McCarson, and Z. Sitar, J. Vac. Sci. Technol. B **15**, 2067 (1997)

McFeely, F. R., S. P. Koalczyk, L. Ley, R. G. Cavell, R. A. Pollak and D. A. Shirley, Phys. Rev. B9, 5268 (1974)

Miskovsky, N. M., P. H. Cutler, and Z. H. Huang, J. Vac. Sci. Technol. B **14**, 2037 (1996)

Modinos, A., *Field, Thermionic, and Secondary Electron Emission Spectroscopy*, Plenum Press, New York 1984

Morrison, S. Roy, *The Chemical Physics of Surfaces 2nd ed*., Plenum Press, New York, 1990

Painter, G. S., D. E. Ellis, and A. R. Lubinsky, Phys. Rev. **B4**, 3610 (1971)

Pate, B. B., et. al., J. Vac. Sci. Technol. **21**, 364 (1982)

Pate, B. B., *et. al*., J. Vac. Technol., **19** (3), 349 (1981)

Pate, B.B., et. al., J. Vac. Sci. Technol. A **2**, 957 (1984)

Peakfit 4 e.g., SPSS Science, 233 S. Wacker Drive, 11th floor, Chicago, IL 60606-6307

Rabalais, J. W., *Principles of Ultraviolet Photoelectron Spectroscopy*, John Wiley & Sons, New York, 1977

Rakhimov, A. T., N. V. Seutin, E. S. Soldatov, M. A. Timofeyev, A. S. Trifonov, V. V. Khanin, and A. Silzars, J. Vac. Sci Technol. B **18**, 75 (2000)

Read, A. J., *et al*., Phys. Rev. Lett. **69**, 1232 (1992)

Rouse, A. A., J. B. Bernhard, E. D. Sosa, and D. E. Golden, Appl. Phys. Lett. **75**, 3417 (1999)

Samson, J. A. R., Rev. Sci. Instr. **40**, 1174 (1969)

Schaich, W.L. and N. W. Ashcroft, Phys. Rev. B **3**, 2452 (1971)

Schulberg, M. T., *et. al*., J. Appl. Phys., **77**, 3484 (1995)

Siegban, Kai *et. al*., *ESCA – Atomic, Molecular and Solid State Structure Studied by Means of Electron Spectroscopy*, Uppsala 1967

Somorjai, Gabor. A., *Introduction to Surface Chemistry and Catalysis*, John Wiley & Sons, Inc., New York, 1994

Spear and Dismukes, *Synthetic Diamond - Emerging CVD Science and Technology,* Wiley, NY, 1994

Spicer, W. E., Phys. Rev. **112**, 114 (1958)

Suryanarayana, C. and M. Grant Norton, *X-Ray Diffraction – A Practical Approach,* Plenum Press New York, 1998

Thomas, R.E., R. A. Rudder, and R. J. Markunas, J. Vac. Technol. A, **10**, 2451 (1992)

Van der Weide, J. and R.J. Nemanich, Phys. Rev. B **49**, 13629 (1994)

Varshini, V. G., Physica **34**, 149 (1967)

Vickerman, J.C., *Surface Analysis – The Principal Techniques,*. John Wiley & Sons: Chichester, 1993

Vidali, G. *et. al.,* Phys. Rev. Lett. **51**, 118 (1983)

Waclawski, B. J., *et. al*., J. Vac. Sci. Technol. **21**, 368 (1982)

Wagner, C.D. et al., *Handbook of X-ray Photoelectron Spectroscopy*, Perkin-Elmer Corporation, 1979

Watanabe, I., T. Yamashita, and M. Sugimoto, Jpn. J. Appl. Phys. **31**, 1187 (1992)

Wyckoff, Ralph W. G., *Crystal Structures 2nd ed*., Interscience Publisher, New York, 26 (1963)

Zangwill, Andrew, *Physics at Surfaces*, Cambridge University Press, Cambridge 1988

Zaremba, E. and W. Kohn, Phys. Rev. B **13**, 2270 (1976)

Zaremba, E. and W. Kohn, Phys. Rev. B **15**, 1769 (1977)

Zhu, W., G. P. Kochanski, S Jin, and L. Seibles, J. Appl. Phys. **78**, 2707 (1995)